Summer 8-15-2020

X-rays from Warped Black Hole Accretion Disks

Quincy Abarr
Washington University in St. Louis

WASHINGTON UNIVERSITY IN ST. LOUIS

DEPARTMENT OF PHYSICS

Dissertation Examination Committee:

Henric Krawczynski, Chair

James Buckley

Francesc Ferrer

Jon M. Miller

Johanna Nagy

X-rays from Warped Black Hole Accretion Disks

by

Quincy Abarr

A dissertation presented to

The Graduate School

of Washington University in

partial fulfillment of the

requirements for the degree

of Doctor of Philosophy

St. Louis, Missouri

August, 2020

Contents

List of Figures

List of Tables

Acknowledgements

There are, of course, many people who have contributed to my success. Here I will attempt to credit and thank them all, in (mostly) order of appearance.

My family, and in particular my parents Russ and Sally Abarr, for supporting me from the very beginning.

My high school Science Olympiad coaches, who fostered my interest in astronomy as it began: Mr. Modlin, Mr. Brubaker, Mrs. Leonard, and especially Mr. Morgan.

The physics department at DePauw University–Howard Brooks, Vic DeCarlo, John Caraher, Jacob Hale, Alex Komives, and Mary Kertzman–who showed me what physics education and instruction should look like; Mary, especially, who set me down the path of high energy astrophysics.

The incoming physics cohort of 2015, because of whom my time at Washington University in St. Louis started out on the right foot; special thanks to John Cavin, Jared Lalmansingh, and Xia Ji. Everyone I have shared office space with, whom I am fortunate to be able to call friends and mentors: Banafsheh Beheshtipour, Ben Groebe, Lindsey Lisalda, Augusto Medeiros da Rosa, Nathan Walsh, Andrew West, and Wolfgang Zober (though I would be remiss to ignore the fact that my productivity increased during the first month of covid quarantine). All of the other friends I have made in St. Louis, including Tyler Webb, Lauren Williams, and Katie Randolph.

Henric Krawczynski, my advisor and boss for the last five years, who has been the model of a collaborative researcher I hope to be able to emulate. Fabian Kislat, Takashi Okajima, and Brian Rauch, who have been additional mentors and sources of knowledge. The rest of the X-Calibur crew from WashU, who have all taught me something and made the X-Calibur campaign more enjoyable: Richard Bose, Garry Simburger, Dana Braun, and Paul Dowkontt. The WASP team, who made the campaign run smoothly: Jim Lanzi, Tom Gadson, Dave Stuchlik, Scott Heatwole, and Zach Peterson. Mószi Kiss, Mark Pearce, Hiromitsu Takahashi, and Yuusuke Uchida, whom it has been a pleasure to get to know and

learn from as the X-Calibur team has supersized.

The McDonnell Center for the Space Sciences and NASA, under grants NNX16AC42G and 80NSSC18K0264, for supporting my work financially. Every staff member in the Physics Department at WashU, including Jan Foster, Sarah Akin, Alison Verbeck, and Linda Trower, for being the true powers behind everything.

Saori Pastore, for trusting my abilities as an instructor and treating me like a collaborator. Matthew Baring and Terri Brandt, for offering me professional advice that has been enormously helpful.

My dissertation defense committee: Jon Miller, Johanna Nagy, Jim Buckley, and Francesc Ferrer, the latter two of whom helped to guide my work over the last few years.

And lastly, Jessica Maginity, who has been by my side and believed in me through all of this.

Quincy Abarr

Washington University in St. Louis

August, 2020

ABSTRACT OF THE DISSERTATION

X-rays from Warped Black Hole Accretion Disks

by

Quincy Abarr

Doctor of Philosophy in Physics

Washington University in St. Louis, 2020

Professor Henric Krawczynski (Chair)

In this thesis, I present the results from my research to better understand accretion onto black holes and neutron stars based on spectropolarimetric X-ray observations. I have developed a general relativistic ray-tracing code which simulates X-rays from warped accretion disks around black holes. I used this to predict the polarization of the thermal X-ray emission and the energy spectrum the reflected power law emission. Both of these can be used to measure properties of black hole systems, such as the spin parameter and the inclination of the observer to its spin axis. My results enable the measurement of these parameters with improved accuracies and with a different set of systematic errors. The methods discussed can be applied to the data of existing X-ray satellites, such as Chandra and XMM-Newton, and upcoming spaceborne missions, such as the Imaging X-ray Polarimetry Explorer (IXPE) and the X-ray Imaging and Spectroscopy Mission (XRISM).

My work also included optimization and deployment of the balloon-borne X-Calibur experiment for its 2018/2019 long duration balloon flight from McMurdo, Antarctica. Results from this flight allowed me to study the light curve and polarization of the hard X-ray emission from the accreting pulsar GX 301-2. I have also contributed to the research and development for its successor, called XL-Calibur, which will observe pulsars and black holes during a northern hemisphere flight in the next few years.

Chapter 1

Introduction

Invisible to telescopic eye
Infinity, the star that would not die
All who dare to cross her course
Are swallowed by a fearsome force

— Rush, *Cygnus X-1 Book I: The Voyage*

1.1 Motivation

X-ray astronomy was made possible by the development of the rocket. This allowed detectors to travel into space (originally for minutes at a time), above the atmosphere which attenuates all X-rays from astronomical sources. On June 13, 1962, the most sensitive detector that had yet been flown aboard a sounding rocket observed a single source dominating the sky: Scorpius X-1, a neutron star accreting matter from a stellar companion [61]. Ever since, physicists and astronomers have been developing more advanced and specialized instruments to study sources of X-rays. Simultaneously, theoreticians have been working to understand why we see what we see: what physical process are happening in these extreme sources; what underlying physical laws govern the behaviour of matter and energy close to strong sources of gravity; what do we still not know? These are mutually beneficial efforts, each motivating the other and offering guidance towards questions that we have the ability to answer and phenomena that we need to explain.

In this thesis, I describe my work predicting the X-ray signals from black holes whose accre-

tion disks are warped. I will discuss the prospects of studying such warped systems using the polarization of X-rays emitted from the hot accretion disk and the profile of the fluorescent iron line from power law emission reflecting off the warped disk. Then, I will discuss the experimental prospects of observing this polarization, focusing on my contributions to the balloon-borne mission X-Calibur.

1.2 Theory of Black Holes

Black holes are the simplest objects in the universe in that they can be described by a few quantities: their mass, their angular momentum, and their electric charge (though this is usually thought to be zero) [22]. The idea that black holes can be described by these few simple parameters is called the no-hair theorem – any additional parameters would make them more 'hairy'. Black holes come out of the General Theory of Relativity, presented by Einstein in 1915 and published in 1916 [44]. Einstein's theory, familiarly called GR, considers space and time as the unified fabric of the universe – spacetime – which matter and energy act to deform. Shortly after GR was introduced, Schwarzschild found the exact solution to Einstein's field equations describing the spacetime around an uncharged, spherically symmetric object with no angular momentum [139]; the Schwarzschild solution is valid for the spacetime around stars, including our Sun. For objects with non-negligible angular momentum, such as astrophysical black holes, we use the Kerr solution [83]. Black holes are such a strange phenomenon by the standards of classical physics that there was no consensus on their existence until the discovery that Cygnus X-1 was too massive to be a neutron star [157, 17].

The environments around black holes are so extreme that the accreting matter – whether from a star locked in companion orbit (in the case of binary black holes) or from the surrounding galactic matter (in the case of supermassive black holes at the center of galaxies) – emits energy as it falls into the black hole, its gravitational potential energy converted

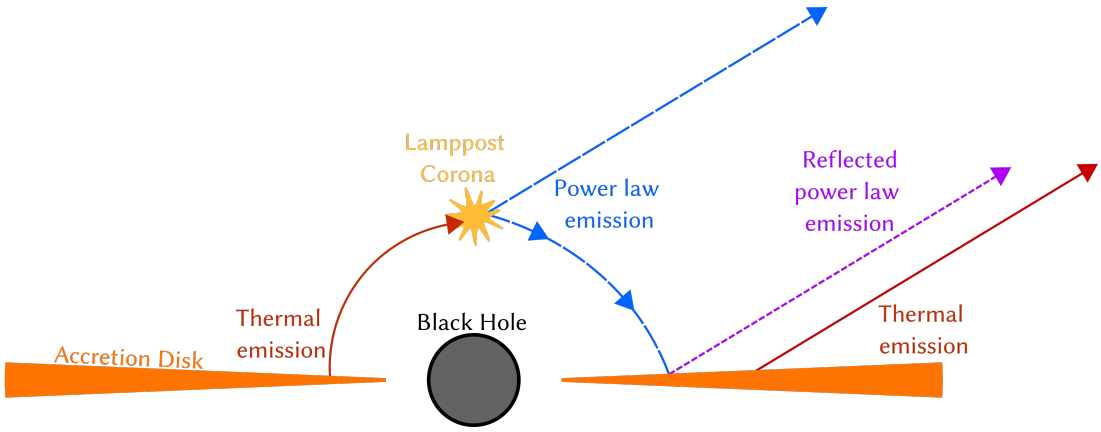

Fig. 1.1: Schematic of a black hole system, highlighting the different components and emission types discussed here.

into radiation in the ultraviolet and X-ray bands. Black holes are thought to have some additional concentration of matter outside of the disk, called the corona. The exact location and size of the corona is not yet known, but the radiation emitted from the accretion disk gains energy in the corona and is emitted back out towards infinity; one of the main goals of studying black holes is to better understand this corona.

A schematic diagram of a black hole is shown in Figure 1.1, including the accretion disk and lamppost corona, as well as the thermal emission and power law emission.

1.2.1 Accretion Disks around Black Holes

Shakura and Sunyaev [142] described a model for a geometrically thin accretion disk. As matter from the surrounding environment falls towards a black hole, it enters a circular orbit due to its significant angular momentum. Shakura and Sunyaev make the approximation that these orbits are Keplerian, with angular velocity $\omega = \sqrt{\frac{GM}{R^3}}$. They lie in the equatorial plane (perpendicular to the direction of the black hole's angular momentum), and their vertical extension is small – making the disk geometrically thin. Viscosity between matter in adjacent orbits causes it to lose angular momentum and spiral inward, its gravitational energy radiated away to infinity and angular momentum transported outward along the disk with efficiency α. Novikov and Thorne [122] extended the work of Shakura and Sunyaev into a steady-

state model including general relativity, and this was further extended into a time-averaged model by Page and Thorne [130]. Page and Thorne derived the radial brightness profile for a generic axially symmetric spacetime, such as the Kerr metric describing a spinning black hole. In these standard thin disk models, the accreting matter is radiatively efficient: the emitted energy is able to escape to infinity rather than scattering within the matter of the disk until it is reabsorbed. If the disk were not radiatively efficient, the increased radiation pressure could 'puff up' the disk, invalidating the thin disk approximation [16].

Thse models tend to treat the inner edge of the accretion disk simplistically: they assume no torque at the innermost stable circular orbit (ISCO) of the disk. Within this radius, matter cannot sustain a stable circular orbit, so it is assumed to fall freely inward to be swallowed by the black hole. This is not the case, as infalling matter may still experience some gas pressure and emit light; it is, however, a good approximation, as this matter is deep enough in the potential well of the black hole that little photon energy is able to reach infinity. The location of this ISCO depends on the spin rate of the black hole, with higher spins allowing for smaller radii. This, combined with the fact that the brightness profile of Page and Thorne [130] is inversely proportional to radius in the disk, yields a powerful tool for measuring black hole spin. A comparison of the thermal spectra for different spins is shown in Figure 1.3, based on simulations of a $10\,\mathrm{M}_\odot$ black hole accreting at half the Eddington accretion rate (the rate at which the inward pull of gravity is balanced by the thermal pressure of the accreting matter). The accretion disk extends from the ISCO out to $100\,\mathrm{r_g}$. $\mathrm{r_g}$ is the radius in gravitational units, where we divide by the black hole mass to get units independent of the size of the black hole: $\mathrm{r_g} = \frac{GM}{c^2}$. In these units, the event horizon and ISCO depend only on the spin of black hole, and decrease as spin increases as shown in Figure 1.2 [9].

While the thin disk model is often a good descriptor of observational data, it will likely need modification as observation techniques advance further. As mentioned earlier, disks may not be geometrically thin if they do not sufficiently radiate away energy; or, rather than being

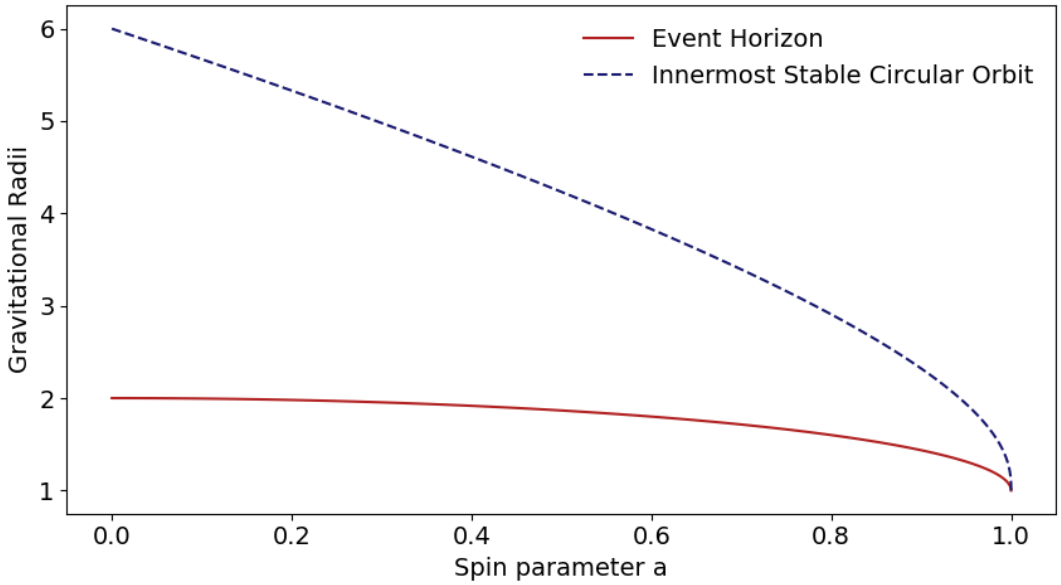

Fig. 1.2: A comparison of the location of the event horizon and innermost stable circular orbit around black holes with different spin. For a Schwarzschild black hole ($a = 0$), the event horizon is at $2\,r_g$ and the ISCO is at $6\,r_g$. These both approach $1\,r_g$ as the spin parameter approaches 1.

in the equatorial plane and perpendicular to the spin axis, the disk may be misaligned. In a binary black hole system, this could occur if the angular momentum axes of the binary orbit and the black hole are not parallel. Throughout this work, I use 'binary black hole' to refer to a black hole in a binary orbit with a stellar companion, not two black holes in binary orbit. In supermassive black holes, it could be the result of galaxy mergers [84].

Bardeen and Petterson [8] first theorized what would happen to the disk around a black hole with misaligned accretion. They predicted that the Lense-Thirring effect [94] would drag the inner region of the disk into alignment and it would remain connected by a smooth warp to the outer misaligned region.

Warped Accretion Disks around Black Holes

We can characterize a warped disk like the one described by Bardeen and Petterson [8] with two additional properties: the 'Bardeen-Petterson' radius r_{BP}, and the tilt β. r_{BP} is the radius at which the aligned inner disk transitions to the misalinged outer disk, which could

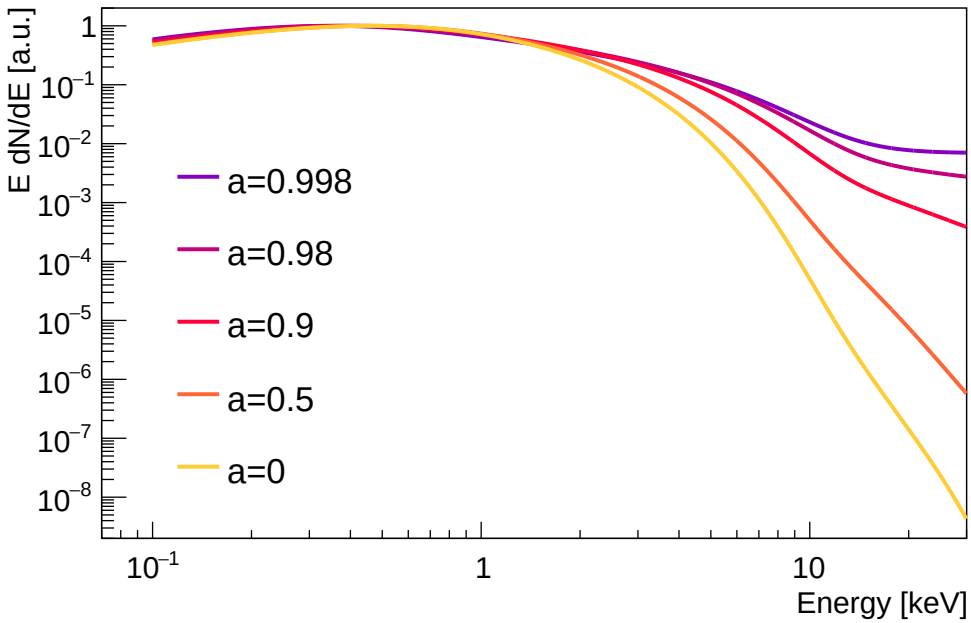

Fig. 1.3: The spectra of thermal emission from the accretion disks around black holes with spins between 0 and 0.998. The higher the spin of the black hole, the higher in energy the spectrum extends. This plot was produced by the code described in Chapter 2.

be a smooth warp or a clean break. The tilt β is the angle between the inner and outer disks, with $\beta = 0°$ being a completely aligned disk.

In nature, warped disks may not be so uncommon: Brandt and Podsiadlowski [18] used Monte Carlo simulations of supernova kick velocities to estimate that 60 % of x-ray binaries have a degree of misalignment between 5° and 45°, while the median misalignment is 20°. This has even been measured in some systems: assuming a radio jet is aligned with the black hole spin axis (thus the inner disk) and the binary orbit with the outer disk, the black hole binary GRO J1655-40 has a misalignment of about 15° [70, 64].

Papaloizou and Pringle [131] analytically described the dynamics of a warped accretion disk by linearizing the hydrodynamical equations of a misaligned disk with a small tilt, conserving angular momentum where previous attempts failed to do so. Their method is valid when the viscosity is greater than the disk thickness at a given radius, $\alpha > H/R$. In this regime, disk instabilities can diffuse through the disk; when $\alpha < H/R$, they propogate in a wave-like manner, allowing for oscillation modes. These two regimes are referred to as the 'diffusive'

and 'bending wave' regimes, respectively.

Kumar and Pringle [93] utilized the equations of Papaloizou and Pringle [131] to calculate values of tilt β and warp radius r_{BP} for different disks. They found that the disk can align with the black hole spin at small radii, agreeing with the predictions made by Bardeen and Petterson. Both Kumar and Pringle and Papaloizou and Pringle, though, note that their linearization is not valid for large tilts.

Pringle [133] derived equations for the time evolution of a disk warp by considering two viscosities between adjacent annuli of disk material: one for the shear in the disk and one for the shear perpendicular to it. The second viscosity can be thought of at the 'twist' of the misaligned part of the disk. This method works for larger values of β and predicts that over time more of the disk will align. Scheuer and Feiler [137] used Pringle's equations to find a steady state, but were forced to use a small tilt due to computational limits of the time. They predicted that for a Shakura and Sunyaev disk the steady state radius would be very large, past the radii from which X-rays originate, and that it would take millions of years to reach this. Lodato and Pringle [98] innovated on the work of Pringle [133] by allowing the axis of the black hole spin to move; in a physical system, both the disk and the black hole can torque each other, which may be why some astrophysical jets are observed to precess. They note, though, that the timescale of the Bardeen-Petterson effect is much longer than the precession timescale observed by Lister et al. [97] in the quasar PKS 1345+125.

A caveat to Pringle [133] is that it completely ignores the internal fluid dynamics of the disk, though further numerical work shows that this does not entirely invalidate it [100]. Ogilvie [125] set out to include these, assuming that the fluid obeys the compressible Navier-Stokes equations (i.e. is isotropic). For a thin disk in the diffusive regime, Ogilvie generalized Papaloizou and Pringle [131] into non-linear equations. This resulted in three coefficients, agreeing with Pringle [133] when the dispersion goes to zero. Ogilvie extended this work later to investigate the bending wave regime, including a proper treatment of radiative transport and viscous dissipation [126, 101].

With these advancements in the one dimensional analytical understanding of disk warping, three dimensional numerical models were developed to study the effect of disk warping based on first principles. Nelson and Papaloizou used smoothed particle hydrodynamics to simulate a disk in the bending wave regime [116, 117]. Smoothed particle hydrodynamics is a computational method in which the medium is treated as collection of particles and the fluid properties such as viscosity and pressure are represented as interactions between pairs of particles. To find a value at any point, an integral is done over a kernal function with some smoothing radius; a common choice for this is the Gaussian function [112].

The first three dimensional simulation of a disk in the diffusive regime was done by Fragile and Anninos [51], where they found that an initally misaligned disk will warp, at which point the warped disk will precess as a nearly solid body. This simulation, though, was done for a thick disk, not a thin disk like the Shakura and Sunyaev model. Later work which included a magnetic field actually found no disk alignment [53].

Lodato and Pringle [100], followed by Lodato and Price [99] (improving upon several issues with the prior work), used numerical SPH to simulate a disk in the diffusive regime; their results agreed with the analytical results of Ogilvie [125]. A fascinating result of this was that the the accretion disk could, for large enough misalignments, break – rather than the two regions being connected by a smooth warp, there is a clean separation with little to no matter between them. This was corroborated by Nixon and King [120], who included internal fluid dynamics in their simulation. They showed that the viscosity must be small to allow the disk to break, and that this could lead to rapid accretion onto the black hole [119].

Recently, Liska et al. [95] used the highly advanced General Relativistic Magnetohydrodynamic (GRMHD) code H-AMR [96] to simulate a very thin disk with $H/R = 0.03$. Applying a warp of 10° to a disk around a black hole with spin 0.9375, they found that the inner disk entered a persistent Bardeen-Petterson configuration with a transition radius of $\mathrm{r_{BP}} \approx 5\,\mathrm{r_g}$ between the inner aligned disk and the outer misaligned disk. The outer disk aquired an

intermediate orientation, possibly due to the cancellation of misaligned angular momentum because of different precession angles of adjacent annuli of the disk [144]. A very important advancement that allowed H-AMR to achieve these results was the inclusion of jets, wich act to torque the inner disk into alignment [109].

1.2.2 Coronae

The corona is the term for the source of the power law continuum observed at high energies in black hole X-ray spectra. It is some hot plasma in which thermal disk photons Compton scatter multiple times and gain energy, a process referred to as Comptonization [65]. From the observed power law we can infer properties of the corona such as its temperature and optical depth; the three dimensional geometry, though, remains unknown. There are several models, including a layer above and below the disk, a sphere surrounding the black hole, or a pseudo-point source above the black hole. This last model (perhaps related to the base of the jet launched by the black hole) is called a lamppost corona. It is often used in simulations due to its simplicy and ability to reproduce observational data [104, 43]. In reality, the corona must have some extension in order to Comptonize thermal disk photons.

1.3 X-ray Spectral and Timing Observation of Compact Stellar Remnants

1.3.1 Black Holes

The X-ray energy spectra of black holes can be decomposed into several components: below a few kiloelectronvolts the thermal emission dominates, but at higher energies a power law continuum dominates. The thermal emission is the blackbody radiation coming off the accretion disk, and its energy is inversely proportional to the size of the black hole: for AGN it peaks in the ultraviolet part of the electromagnetic spectrum, while for binary black holes

it peaks in the X-ray around 1 keV. As mentioned above, the power law continuum is the result of thermal photons Comptonizing in the corona.

Black holes tend to emit in three states, which are combinations and variants of these two types of emission [135]. When the thermal emission dominates, with little to no presence of the power law, the black hole is said to be in the 'thermal state'. The 'hard state' is when instead the power law dominates over small contributions from the thermal emission. This state is associated with the presence of a jet detected in the radio band, reinforcing the association of the lamppost corona with the base of the jet. The third state is the 'steep power law', in which the power law still dominates, but a larger photon index Γ means the emission does not extend out to as high energies as in the hard state.

While some of the power law photons travel directly from the corona to the observer, a portion illuminate the accretion disk. In binary black holes, where the temperature of the disk is higher, these photons tend to reflect off the disk, changing direction but not energy. In AGN, though, more often these reflected photons are of high enough energy to cause ions in the disk to fluoresce: one of the electrons in the ion will transition to a higher state as it absorbs the incident photon, then as the electron fall back to its original state it will emit another photon with energy matching the transition. In accretion disks, the most prominent ionization line is the Iron Kα line at about 6.4 keV [60]. The line is comprised of contributions from several transitions in different ions; the two most prominent are the Kα_1 and Kα_2 transitions in the FeI ion at 6.404 keV and 6.391 keV, respectively.

The iron line is interesting for the astrophysical study of accreting systems because it is relativistically blurred by two effects: redshift from escaping the gravitational well of the black hole and Doppler shift due to the orbit of the fluorescing disk matter. Since, as previously mentioned, the inner edge of the accretion disk depends on black hole spin, the degree of redshift of the reflection from the ISCO will be correlated with spin. The degree of Doppler shift depends on how quickly the disk material is movings towards or away from us, so the more highly inclined (i.e. edge-on) the disk is the more parallel the motion of the

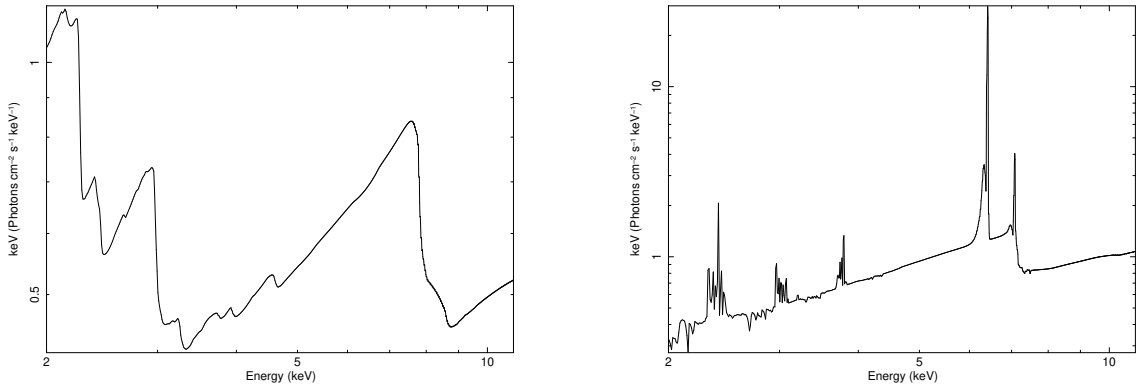

Fig. 1.4: Left: An example iron line profile produced by `relxill` for a binary black hole with spin $a = 0.998$ and inclination of 60°. Right: An example of the line emission in the local reference frame of the disk material.

material will be to to the line-of-sight and the stronger the shift will be. We define inclination as the angle between the line of sight and disk angular momentum, which is usually parallel to the black hole spin axis; the disk will be fully edge-on at an inclination of 90°.

These effects smear the iron line out over several kiloelectronvolts on either side of the rest-frame energy. This can be modelled based on radiative transfer calculations of the reflection combined with photon propagation through the Kerr spacetime around the black hole. One such model is `relxill`, to which data can be fit to find the most likely spin and inclination of black hole systems [46]; an example of a profile produced by `relxill` is shown in Figure 1.4. Since warped disks have two characteristic inclinations (of the inner and outer disks), the iron line can carry information about the degree of warping [52].

The iron line also allows us to do reverberation mapping of the black hole environment. Any temporal fluctuations in the power law source will be present in both the power law emission travelling directly to us as well as the component reflection off the disk. The time difference between the direct and reflected components will be based on the distance between the power law source and the disk from which it reflects, so by isolating the reflected component through the iron line, we can constrain the position and size of the corona [153, 82].

1.3.2 Neutron Stars

The accretion picture looks different around neutron stars than it does around black holes. Though an accretion disk may form far out from the neutron star in much the same way it does around a binary black hole, near the neutron star its strong magnetic field forces the matter towards its poles. Within the Alfvén radius (the radius as which magnetic energy density of matter of is equal to its kinetic energy density) the accreting plasma couples to the magnetic field lines and forms an accretion column. For typical neutron star parameters, this radius is 1800 km [20].

There are two accepted models for the pulsed X-ray emission from neutron stars. In brighter neutron stars, where the optical depth of the accretion column is large, the matter falling towards the magnetic pole is shocked at some height above the surface and slowly sinks, emitting radiation out of the column perpendicular to the magnetic field lines; this is the fan beam model. If instead the optical depth is low, the matter is able to fall all the way to a hot spot on the surface of the star, which emits radiation parallel to the field lines; this is the pencil beam model [111].

The X-ray spectrum of neutron stars is well-described by a power law with an exponential cutoff; typically, the power law peaks at 5 to 20 keV, and the cutoff energy is 20 to 30 keV. Becker and Wolff [10] model the spectrum from a fan beam accretion column as a combination of bremsstrahlung, cyclotron, and thermal emission Comptonizing; they use this to fit the spectrum of Hercules X-1. The power law spectrum can be modified by an iron line like we see in the reflection spectra of black holes, as well as cyclotron resonant scattering features (CRSFs), also called cyclotron lines. In the strong magnetic fields near neutron stars, the energy of electrons are quantized into Landau levels, and thus photons scattering off these electrons have specific energies given by

$$E_{CRSF} = n\frac{11.6\,\mathrm{keV}}{1+z}\frac{B}{10^{12}\,\mathrm{G}}. \tag{1.1}$$

z is the redshift from the emission site (which can be as high as $\sim$0.3 if coming from the neutron star surface), B is the magentic field at the emission site in Gauss, and n is an integer to indicate the presence of harmonics. Cyclotron lines are of extreme interest because they offer the best way to measure the magnetic field of neutron stars. They also allow us to observe the changing height of the emission region in these sources: with an increase in luminosity, the fan beam shock front moves higher in the accretion column where the magnetic field is weaker, thus lowering the energy of the cyclotron line [152, e.g.]

1.3.3 X-ray Timing and Spectroscopic Instruments

In the early days of X-ray astronomy, the most reliable way to get above the atmosphere was with sounding rockets [61]. Once inserting satellites into orbit around Earth became feasible, instruments could observe for much longer periods of time. The first such satellite was Uhuru, launched from an Italian platform off the coast of Kenya in 1970. Over they next few years it discovered 339 X-ray sources [49]. Uhuru consisted of a pair of proportional counters each with an effective area of 840 cm^2, and fields of view of 0.52° and 5.2°. It operated in the 1.7 to 18 keV bandpass, with eight energy bins for spectra [143].

The Rossi X-ray Timing Explorer (RXTE), in operation from 1995 to 2012, was designed to study the time variablity of X-ray sources; though its energy resolution was relatively poor (3.2 keV at 10 keV), its timing resolution was on the order of 1 µs [76, 143, 4].

One of the greatest achievements of X-ray astronomy is the Chandra X-ray Observatory, launched in 1999 with a nominal lifetime of five years – but still in operation at time of writing. Chandra uses a Wolter Type 1 grazing incidence mirror to focus X-rays onto four different detectors. It has an angular resolution more than a thousand times smaller that Uhuru – the point spread function (PSF) of the mirror is 0.5″. The Advanced CCD Imaging Spectrometer (ACIS) instrument on Chandra has two arrays, ACIS-I and ACIS-S, which have energy resolutions at 1.5 keV of 140 eV and 100 eV, respectively, and effective areas of 580 cm^2 and 670 cm^2. There are also gratings on Chandra, which can do spectroscopy with

energy resolutions on the order of 1 keV; this sacrifices the imaging capabilities of the ACIS, though, and has roughly one-tenth the effective area [160, 143].

The European equivalent to Chandra, XMM-Newton, is also still in operation. It trades off angular resolution for collecting area, consisting of three Wolter I mirrors with 14″ PSFs. The primary instrument on each of the XMM telescopes is the EPIC-MOS, an X-ray CCD with an effective area of 1000 cm^2 and energy resolution of 94 eV at 1.8 keV [78, 143].

In 2004, the Neil Gehrels Swift Observatory was launched, containing three different instruments designed help localize gamma-ray bursts (GRBs). The Burst Alert Telescope, sensitive in the 15-150 keV range, scans the sky constantly; when a GRB is discovered, it quickly slews the co-aligned X-ray Telescope (XRT) and Ultraviolet/Optical Telescope to observe the GRB [58].

More recent observatories include NuSTAR (the Nuclear Spectroscopic Telescope Array) and NICER (Neutron Star Interior Composition Explorer). NuSTAR which was launched in 2012 and observes high energy X-rays (3-79 keV) using four Cadmium Zinc Telluride detectors [66]. NICER was launched in 2017; it is attached to the International Space Station rather than in free orbit around the Earth. It observes X-rays in the 0.2-12 keV range with an absolute timing better than 300 ns. This unmatched timing resolution allows NICER to do phase-resolved spectroscopy of pulsars, constraining their radii and interior structure [59].

With both Chandra and XMM-Newton approaching their anticipated end-of-life in the coming years, there are three next-generation X-ray missions currently in the planning and construction phases. The European Space Agency is planning to launch Athena (Advanced Telescope for High-Energy Astrophysics) in the early 2030s. Athena is the successor to XMM-Newton and observers in a similar energy range, 0.2-12 keV, but is significantly more advanced: the specifications are not finalized, but the goal is for the X-IFU, Athena's primary X-ray detector, to have an effective area of 2 m^2 at 1 keV, and a spectral resolution of 2.5 eV, made possible by the use of highly efficient Transition Edge Sensors [115]. NASA and JAXA (the Japanese space agency) are jointly launching XRISM (X-ray Imaging Spec-

troscopy Mission) in 2022 to recover some of the capabilities of the JAXA satellite Hitomi, which was lost shortly after launch in 2016. Specifically, the *Resolve* soft X-ray spectrometer on XRISM will have a spectral resolution of 7 eV [164]. Lastly, the Lynx mission [57] is one of the contenders for the Great Observatory likely to be recommended by 2020 Decadal Survey of the National Academy of Sciences, and if selected will launch in the mid 2030s. It is the successor to Chandra, achieving a similar angular resolution while also having a large effective area comparable to Athena.

1.4 X-ray Polarimetry

Polarization of a light source refers to its tendency to emit photons with their electric fields aligned with one another. In the most general case, a light source will be unpolarized; that is, it will emit photons with random electric field directions. Some processes, however, will tend towards a specific direction, giving rise to polarization. Polarization gives two observables of light: polarization angle is the direction of electric field oscillation that the light tends towards, and polarization fraction is the percent of photons that will have that direction.

It is often useful to use Stokes parameters to describe the polarization of individual photons. There are three Stokes parameters of linear polarization: Q, U, and I (a fourth, V, describes circular polarization, but is not relevent to this work as the discussed X-ray polarimeters do not constraint V). Q and U are a measure of the polarization, while I is the intensity of the light; Figure 1.5 shows Q and U. These are related to polarization fraction Π and direction χ by

$$\Pi = \sqrt{\left(\frac{Q}{I}\right)^2 + \left(\frac{U}{I}\right)^2} \qquad \chi = \frac{1}{2}\arctan\left(\frac{U}{Q}\right) \tag{1.2}$$

A photon with $+Q = I$ is fully polarized in the $+Q$ direction. The Stokes parameters of combined beams of light are additive, which makes them particularly well suited to use in X-ray astronomy since we observe individual photons and can thus add their Stokes parameters to find the net polarization of a source.

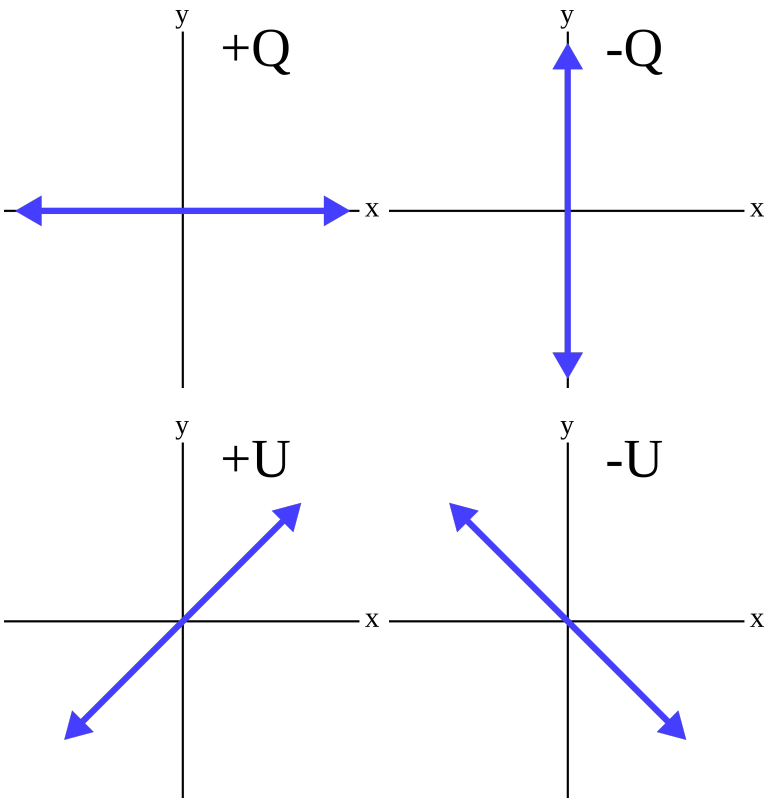

Fig. 1.5: Stokes parameters Q and U

Scattering is one of the most common source of polarization; Chandrasekhar [24] calculated the incoming and outgoing Stokes parameters of light in a variety of scattering conditions, such as diffuse and planar atmospheres. His work forms a backbone for studying polarization of astrophysical sources; in particular, this is the main resource we use to calculate the scattering of photons off the geometrically thin, optically thick accretion disk in our ray-tracing code discussed in Chapter 2 and used to predict polarization and flux spectra in Chapters 3 and 4.

Polarization has long been a tool of observational study in bands of the electromagnetic spectrum other than X-ray (optical and radio polarization have a pedigree going back decades [see 72, for more information]). Long studied theoretically [111, 24, e.g.], X-ray polarimetry has had, at the time of writing, a single dedicated satellite with OSO-8, launched in 1975. It consisted of a pair of Bragg-diffracting graphite crystals [158] with which it measured the polarization fraction of only the brightest X-rays sources at 2.6 and 5.2 keV, including a

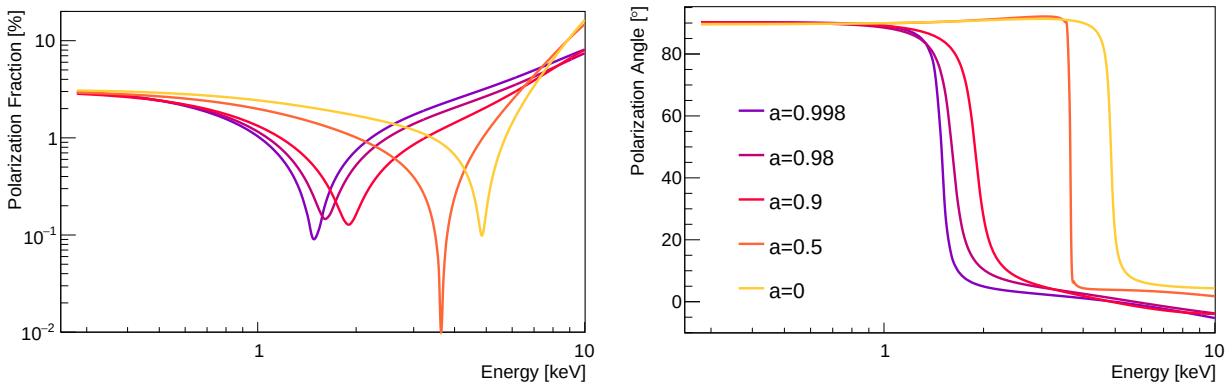

Fig. 1.6: The change in polarization over spin, for a $10\,M_{\odot}$ black hole accreting at half the Eddington rate. This plot was produced by the code described in Chapter 2.

19 % polarization of the Crab nebula [159]. Recent technical developments such as gas pixel detectors [113] and high efficiency Cadmium Zinc Telluride (CZT) detectors have made possible the ability to measure the polarization of weaker astrophysical sources with higher accuracy. In Chapter 5, I will discuss my contributions to one such mission, X-Calibur, which uses CZTs.

1.4.1 Polarization of X-rays from Mass Accreting Black Holes

The thermal emission from a black hole tends to be polarized parallel to the plane of the accretion disk from which its emitted, though it can become weakly polarized due to rotation of the plane of polarization along the geodesic of photons travelling close to the black hole. The main cause of polarization in these systems is reflection: according to Chandrasekhar, when light scatters perpendicular to its initial trajectory, the resulting beam is nearly 100 % polarized. This can occur when the strong gravitational curvature near black holes leads some thermal disk photons emitted near the ISCO to bend back towards the disk and scatter. Since the energy of thermal photons increases towards smaller radii, the spectrum of polarization angle swings by ∼90° when the reflected emission begins to dominate.

Polarization spectra (examples of which are shown in Figure 1.6) give us information about two properties of a black hole: its spin and inclination. The polarization fraction at low

energies, below the transition, depends on the inclination of the system. When the accretion disk is more highly inclined, the direct emission that reaches the observer comes out of the disk atmosphere more obliquely, which makes it more polarized [24]. This is a weak effect – even at high inclinations the polarization fraction is still just a few percent. The spin can be measured by the energy at which the polarization angle transitions from being dominated by direct emission to reflected. Assuming the accretion disk follows the Novikov and Thorne model, the transition energy changes by several kiloelectronvolts between a non-spinning and maximally spinning black hole.

This effect can be used to test the validity of general relativity in the strong gravity regime: since some alternative theories of gravity allow for different innermost stable circular orbits, spin measurements using polarization will disagree with measurement by other methods [see 91, 71].

1.4.2 Polarization of X-rays from Mass Accreting Neutron Stars

Meszaros et al. [111] calculated the expected polarization for the fan and pencil beam models. In the environment of a pulsar, the predictions from quantum electrodynamics (QED) of the birefringence of the magnetized vacuum become important, as does the mode dependence of scattering and absorption. Using the results of Meszaros and Nagel [110], Meszaros et al. [111] calculated the polarization of an accreting pulsar at various energies and relative inclinations of the observer and magnetic field. They found that polarimetry can robustly differentiate between the fan and pencil beams. In Figure 1.7, I have adapted plots of their results. Over all inclinations and energies, when phase resolved, the peak in pulse amplitude is *correlated* with the peak in polarization fraction in the fan beam model, while the pulse peak is *anticorrelated* with the fraction peak in the pencil beam.

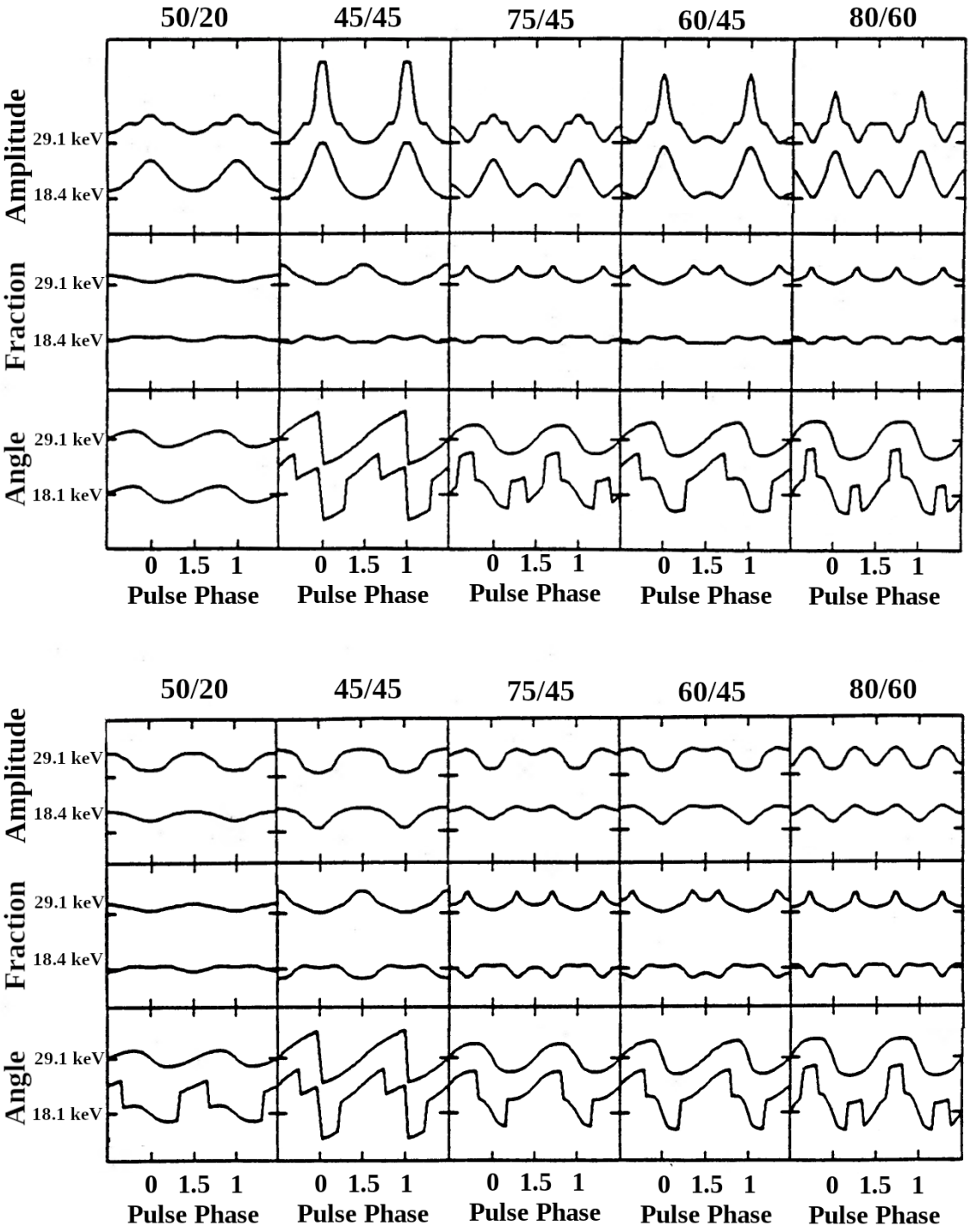

Fig. 1.7: Predicted polarization fraction and angle from the pencil beam (top) and fan beam (bottom) resolved over the pulse phase. Results are shown for 18.4 keV and 29.1 keV. The five division left-to-right are for different observer inclinations, labeled at the top in the form (inclination of the observer)/(inclination of the magnetic field), both of which are compared to the angular momentum of the pulsar. Adapted from Meszaros et al. [111] (Original figure © AAS, reproduced with permission).

1.4.3 X-ray Polarization Instruments

X-ray polarization is particularly difficult to observe, since statistics tend to work against it: X-ray observations often consist of a handful of photons, which does not allow for strong polarization measurements. The governing statistic for polarization is the minimum detectable polarization (MDP), shown in Equation 1.3 for a confidence of 99 % [13].

$$\mathrm{MDP} = \frac{4.29}{\mu R_S}\sqrt{\frac{R_S + R_B}{T}}. \tag{1.3}$$

μ is the modulation factor of the given polarimeter (typically around 0.5), representing the modulation in signal detected for a 100 % polarized source. If $\mu = 0.5$, there will be a 50 % increase in photons measured at $\pm 90°$ from the polarization angle. T is the observation length, and R_S and R_B are the signal and background rates, respectively. Polarized sources tend to have polarization fractions on the order of 10 %, so 90 % of X-rays from the source are unpolarized and contribute to the background. Long observations are thus required to push the MDP down to a useful level: for example, detecting an MPD of 5 % with an instrument that has a modulation factor of 0.5 and sees no background requires 3×10^4 photons. To put this in perspective, the Crab nebula, the second brightest persistent X-ray source in the sky, would need to be observed by the Swift Burst Alert Telescope for almost two days in order to see this many counts. The Crab is a useful source for such comparisons, as its rate of activity is very consistent. It is often even used as a unit of measure: we might refer to the rate of another source active at half the level of the Crab as 500 mCrab, for example.

None of the plans for X-ray polarimeters in the intervening time since OSO-8 have come to fruition: a polarimeter was part of the original plan for Spectrum-X-Gamma [80] before that mission was abandonded during the fallout of the dissolution of the Soviet Union [33], to name one example. There have, however, been gamma-ray instruments with polarization capabilities. INTEGRAL (the International Gamma-ray Astrophysics Laboratory), launched in 2002 by the European Space Agency, is a hard X-ray/soft gamma-ray obser-

vatory. Above 100 keV, its spectrometer, called SPI, is sensitive to polarization due to its reliance on Compton scattering, a process inherently sensitive to polarization [25]. The SPI consists of 19 hexagonal Germanium crystals [154]. The polarization angle of a photon can be measured when it Compton scatters in one crystal and, rather than being absorbed in that same crystal, deposits energy in an adjacent one; these type of detections account for about 20 % of the flux above 100 keV. INTEGRAL has observed the Crab nebula multiple times over its mission, and has found that the polarization of emission is aligned with the pulsar spin axis [39, 50]. Recent analysis of the entire set of Crab observations found a polarization fraction of (24 ± 4) % [79].

Within the last decade, X-ray polarimetry has become a viable observational program. During a balloon flight from Sweden in 2016, *PoGO+* constrained the polarization of the Crab nebula [27, 29] and the accreting black hole Cygnus X-1 [28, 30]. PoGO+ is a Compton scattering hard X-ray (>20 keV) polarimeter in which incident photons scatter within an array of 61 plastic scintillating rods, each read out by a photomultiplier tube (PMT). This setup allows PoGO+ to measure the angle of photon scattering when two scintillations occur within a small enough time window of each other.

X-Calibur, a balloon-borne Compton polarimeter, flew from McMurdo, Antarctica in the 2018-2019 Austral summer and constrained the polarization of the accreting pulsar GX 301-2 [1]. In X-Calibur, X-rays are focused by a grazing incidence mirror onto a beryllium rod, which is aligned with the optical axis of the mirror. The X-rays Compton scatter in the beryllium rod and are detected by CZT detectors on all four sides, from which their scattering angle is deduced.

1.5 Outline of Thesis

The rest of my thesis is organized as follows: In Chapter 2, I describe the ray-tracing code we use and the warped disk model I implemented. In Chapter 3, I present my results

from simulating the polarization of the thermal emission from a warped disk. I discuss the prospects for measuring disk warping X-ray polarization, specifically using IXPE. In Chapter 4, I use the warped disk model to simulate the reflected emission originating in a lamppost corona. I compare the results to `relxill`, and discuss the implications on extracting black hole spin and disk inclination from measured iron line profiles. In Chapter 5, I summarize my work on X-Calibur that contributed to the polarimetric observations of the pulsar GX 301-2. In Chapter 6, I discuss several future projects, including upcoming polarimetry missions and advancements in simulation; finally, I summarize the main results of this thesis.

Chapter 2

General Relativistic Ray-Tracing of X-rays from Accreting Black Holes

Black holes collect problems faster than they collect matter.

—Carl Sagan, *Contact*

2.1 Introduction

In the last few years, GRMHD simulations have achieved a high degree of maturity which enables the study of black hole dynamics and accretion from first principles, accounting for general relativistic effects, plasma hydrodynamics, and global as well as dynamically generated magnetic fields. GRMHD techniques have advanced from being able to simulate thick, radiatively inefficient disks [e.g. 67] to geometrically thin disks as in the Shakura and Sunyaev model [121]. Recent codes such as H-AMR [96] have sufficient resolution to capture the magnetic turbulence which is the source of viscosity in the disk plasma that allows angular momentum to transport outward, and thus matter inward. Currently, efforts are focused on including the energy transport and radiation pressure, but we are still far from capturing the full angle and frequency dependent radiative flux in GRMHD codes.

It is useful, then, to use ray-tracing codes like Geokerr [40] to interpret the results of GRMHD simulations to predict the signals from black hole sources. Many codes, Geokerr included,

tend to calculate geodesics from the observer to the emitter, which precludes the inclusion of polarization-dependent photons scattering dynamics, as well as possibility for photons to scatter off the disk multiple times. Agol and Krolik [5] studied the impact of multiple scatterings by placing an observer on the accretion disk and calculating geodesics originating in other parts of the disk, and Schnittman and Krolik [138] developed a ray-tracing code which forward evolves photons along geodesics, allowing both the inclusion of scattering dynamics and multiple scatterings. They showed that such photons have a significant effect on the polarization of X-rays from the disk. Krawczynski [91] developed a similar code in order to investigate the usefulness of polarimetry to test general relativity; this is the basis for the code which I discuss in this chapter.

In Section 2.2 I present an overview of the ray-tracing code we use, including the Cash-Karp method I implemented to integrate the photon geodesic and parallel transported the polarization vector through the Kerr spacetime around the black hole. Then, in Section 2.3 I describe the orthonormal reference frame used to transform photon beams into the inertial local frame of the orbitting disk material. In Section 2.4 I develop an approximate description of misaligned accretion disks in the Kerr metric; this allows us to study the observational appearance of disks with warps in the very inner portion of the accretion flow where the background metric cannot be approximated by the Schwarzschild metric.

2.2 Overview of the General Relativistic Ray-Tracing Code

Our ray-tracing code [91, 71, 11, 89], written in C/C++, generates photon packages (or beams) either in an accretion disk located in the equatorial plane or a point or spatially extended corona. After emission, we use the Cash-Karp method [23, 132] to integrate the geodesic equation:

$$\frac{d^2x^\mu}{d\lambda^2} = -\Gamma^\mu_{\sigma\nu}\frac{dx^\sigma}{d\lambda}\frac{dx^\nu}{d\lambda}, \tag{2.1}$$

and to parallel transport the polarization vector f^μ:

$$\frac{dx^\mu}{d\lambda} = -\Gamma^\mu_{\sigma\nu} f^\sigma \frac{dx^\nu}{d\lambda}. \tag{2.2}$$

Here, λ is the affine parameter and $\Gamma^\mu_{\sigma\nu}$ are the Christoffel symbols, defined in terms of the metric coefficients by

$$\Gamma^\mu_{\sigma\nu} = \frac{1}{2} g^{\mu\rho} \left(\partial_\sigma g_{\nu\rho} + \partial_\nu g_{\sigma\rho} - \partial_\rho g_{\sigma\nu} \right). \tag{2.3}$$

The integration gives us the geodesics $x^\mu(t)$, as well as the wave vector k^μ and polarization vector f^μ of each photon along the geodesic.

We use the Kerr metric in Boyer-Lindquist coordinates for the spacetime around an uncharged black hole:

$$\begin{aligned} ds^2 = &- \frac{r^2 - 2Mr + a^2}{r^2 + a^2 \cos^2\theta} \left(dt - a \sin^2\theta d\phi \right)^2 + \frac{\sin^2\theta}{r^2 + a^2 \cos^2\theta} \left(\left(r^2 + a^2 \right) d\phi - a dt \right)^2 \\ &+ \frac{r^2 + a^2 \cos^2\theta}{r^2 - 2Mr + a^2} dr^2 + (r^2 + a^2 \cos^2\theta) d\theta^2, \end{aligned} \tag{2.4}$$

where the black hole has mass M and angular momentum J, and $a = J/M$ is the dimensionless spin parameter. Boyer-Lindquist coordinates are useful because the metric is maximally diagonal outside of the black hole.

Photons are tracked until they get within 2 % of the black hole event horizon or until they reach $10\,000\,\mathrm{r_g}$. In the former case, photon beams are assumed to be lost within the event horizon; we stop tracking here due to the Boyer-Lindquist coordinate singularity at the event horizon. When the latter occurs, the wave vector is transformed into the reference frame of a coordinate stationary observer for post-processing.

2.2.1 Thermal Photons

Emisson

Emission of thermal photons is based on the model of Page and Thorne [130]. They describe a geometrically thin, optically thick accretion disk with temperature

$$T_{eff} = \left(\frac{F(r)}{\sigma_{SB}} \right)^{1/4}. \tag{2.5}$$

σ_{SB} is the Stefan-Boltzmann constant, and $F(r)$ is the time averaged flux from the disk

$$F(r) = \frac{\dot{M}_0}{4\pi} e^{-(\nu+\psi+\mu)} \frac{-p^t_{,r}}{p_\phi} \int_{r_{ISCO}}^{r} \frac{p_{\phi,r}}{p^t} dr. \tag{2.6}$$

"$,r$" indicates partial differentiation with respect to r, p^μ is the four-momentum of the disk material, $\dot{M}_0$ is the time averaged rate at which rest mass flows inward through the disk, and ν, ψ, and μ are determined by the metric.

Thermal photons are emitted from 10 000 radial bins spaced equally logarithmically between $\mathrm{r_{ISCO}}$ and $100\,\mathrm{r_g}$. They are given a random initial trajectory into the upper hemisphere with equal probability per solid angle in the frame of the disk plasma (hereafter called the plasma frame). For the statistical weight and initial polarization fraction of each photon we use Table XXIV from Chandrasekhar [24], which gives the limb brightening function of an indefinitely deep electon-scattering atmosphere. The polarization vector of the photon is initially perpendicular to its wave vector and the θ direction in Boyer-Lindquist coordinates; this makes it parallel to the surface of the disk. Finally, we transform into the global Boyer-Lindquist coordinates for tracking.

Scattering off the Disk

When a thermal photon impinges on the accretion disk, it is scattered using the formalism of Chandrasekhar [24] for scatterings of polarized photons off an infinitely thick electron-

scattering atmosphere. The disk is assumed to be highly ionized, reflecting nearly 100 % of incident photons; this is often the case around stellar mass black holes. The properties of the photon, includings its position, wave vector, and polarization vector, are recorded at each scattering event, and so during analysis we can apply a different weighting if we wish to simulate a disk which reflects fewer photons.

The scattering is implemented in several steps: First, the wave vector and polarization vector of the incoming beam are transformed from the global Boyer-Lindquist coordinates into the Lorentz frame of the reflecting material; this procedure is described in more detail in Section 2.3. Given the polarization vector in this frame, the incoming Stokes parameters are calculated. A random scattered direction is drawn with equal probability per solid angle, and Equation (164) and Table XXV from Chapter X of Chandrasekhar [24] are used to determine the Stokes parameters of the outgoing beam. The Stokes parameters are subsequently used to calculate the polarization fraction and polarization angle of the outgoing beam and to calculate the statistical weight for the particular scattering direction. In the final step, the polarization angle is converted into the local polarization vector, and the wave vector and polarization vector are transformed back into the global Boyer-Lindquist coordinates.

2.2.2 Power Law Photons

Emission

Each geodesic from the lamppost corona represents a beam of photons with energies distributed accorting to the power law $N(> E) \propto E^{-(\Gamma-1)}$. To emit power law photon beams, I use the lamppost corona model [106, 43] which I described in Section 1.2.2. The lamppost has a programmable height and is located 1° off the $\phi = 0°$ axis due to the Boyer-Lindquist coordinate singularity there. Photons initially have a random trajectory down towards the disk, but with the θ component of their four velocity equal to zero. Lamppost photons are initially unpolarized, and since fluorescence is not a polarizing process I do not consider the polarization of these photons in my work. Our code is also capable of simulating the

Comptonization and emission of photons from several extended corona models, including the wedge and spherical corona [11], but I do not use these in this work.

Scattering off the Disk

When a beam hits the accretion disk, we record the frequency shift undergone between emission in the lamppost frame and reflection in the accretion disk plasma frame, and launch a new photon beam in a random direction in the plasma frame. Once a beam reaches the distant observer, we take its contribution to the total spectrum from the inclination dependent intensity from XILLVER. This is the line-producing part of `relxill` (it is responsible for the unblurred profile on the right in Figure 1.4), and thus by itself does not include the relativistic effects of the entire `relxill` package.

XILLVER simulates a forest of atomic absorption and emission lines, all of which depend on the properties of the black hole system: the lamppost height, black hole spin, inclination of the disk to the observer, abundance of iron, power law index, and ionization state of the disk are among the most important. Most of these properties are uniform for a given simulation; the exception is the apparent disk inclination due to general relativistic light bending and frame transformations as the fluoresced photon travels to the observer. Thus, for each photon beam, we take the XILLVER spectra for the emission angle in the plasma frame. During analysis, we add together the spectra of all photon beams that reach the observer, applying the frequency shift experienced by the beam as it travels from the point of emission to the observer, including the effect of transforming out of the plasma frame and into the coordinate stationary observer frame.

2.2.3 The Cash-Karp Method

The Cash-Karp method is a 5th order Runge-Kutta numerical integration method which allows for an adaptive step size. The Runge-Kutta methods are a family of ordinary differential equation solvers which take the known solution to the function $y(x)$ (in our case, the

geodesic equation) at a single point (when the photon is generated) and propagate it over steps of size h until we reach the desired endpoint (the distant observer). The general form for a solution of order m is to calculate each function k_n, for n from 1 to $m+1$, by

$$k_n = hf\left(x_{initial} + a_n h, y_{initial} + \sum_{j=1}^{n} b_{nj} k_j\right), \tag{2.7}$$

where each subsequent function depends on the previous. From the functions k_n, the next step is calculated using

$$y_{final} = y_{initial} + \sum_{j=1}^{n} c_j k_j. \tag{2.8}$$

The coefficients a_n, b_{nj}, and c_j are particular to the Runge-Kutta method being used; for the Cash-Karp method, they are collected in Table 2.1. The Cash-Karp is an embedded Runge-Kutta method; this means that it contains a fourth-order solution y^* calculated with the same k_n functions and different set of coefficients c_j^*:

$$y^*_{final} = y_{initial} + \sum_{j=1}^{n} c^*_j k_j. \tag{2.9}$$

This second solution allows us to estimate the error in the fifth-order solution as the difference between the two, $y_{final} - y^*_{final}$, and for subsequent steps we can increase or decrease h based on how precise we wish the calculation to be.

I implemented the Cash-Karp method into our ray-tracing code because of its inclusion of adaptive step size; previously, the code used the standard 4th order Runge-Kutta method. In addition to the Cash-Karp method, I tested the Fehlberg [48] and Dormand-Prince [41] adaptive step size methods, but found that the Cash-Karp method performed best for our purposes. Adaptive step size is especially important in general relativistic calculations since space is highly curved near the black hole (where a large step size introduces error) and asymptotically flat far from the black hole (where a small step size causes the photon to take an enormous amount of CPU time to reach the observer); the step size in our code varies

a_n	b_{nj}					
0						
1/5	1/5					
3/10	3/40	9/40				
3/5	3/10	-9/10	6/5			
1	-11/54	5/2	-70/27	35/27		
7/8	1631/55296	175/512	575/13824	44275/110592	253/4096	
c_i:	37/378	0	250/621	125/594	0	512/1771
c_i^*:	2825/27648	0	18575/48384	13525/55296	277/14336	1/4

Tab. 2.1: The Cash-Karp Butcher tableau

by several orders of magnitude along a geodesic. In addition to the embedded Cash-Karp error, our code keeps track of the integration error using k^2, which should be zero for a null geodesic, and f^2, which should remain constant along the geodesic. By implementing the Cash-Karp method, I improved the error as measured by k^2 by roughly an order of magnitude and halved the runtime per photon beam. In its current state, the ray-tracing code is able to simulate about 10^7 photons per hour on the WUSTL physics department's computing cluster.

2.3 Orthonormal Bases

In general relativity, we have the ability to transform our coordinate system in to a reference frame which is most useful for a given problem. While the Boyer-Lindquist coordinate system is best for tracking photon beams through the Kerr spacetime around the black hole, these coordinates obscure the physics of scattering when a photon impinges on the accretion disk. Chandrasekhar [24] calculated polarized scattering for an indefinitely thick electron scattering atmosphere in a reference frame for which the scattering atmosphere is at rest. To transform the wave and polarization vectors of a scattering photon beam into this locally

flat rest frame for the orbiting disk material, we use a tetrad – a system of orthonormal basis vectors describing a given local inertial frame. The tetrad $\mathbf{e}_{\hat{\mu}}$ for disk matter in the equatorial plane is defined in terms of the Boyer-Lindquist basis vectors ∂_μ. To make this represent the rest frame of the orbiting disk material, we set its first component $\mathbf{e}_{\hat{t}}$ equal to the four-velocity of the matter. Since circular orbits in the equatorial plane have constant r and θ coordinates, $\mathbf{e}_{\hat{r}}$ and $\mathbf{e}_{\hat{\theta}}$ are unchanged. Lastly, $\mathbf{e}_{\hat{\phi}}$ is chosen to ensure orthonormality. These four vectors are defined as

$$\mathbf{e}_{\hat{t}} = \partial_t + \Omega_{\rm k}\partial_\phi \tag{2.10}$$

$$\mathbf{e}_{\hat{r}} = \partial_r/\sqrt{g_{rr}} \tag{2.11}$$

$$\mathbf{e}_{\hat{\theta}} = \partial_\theta/\sqrt{g_{\theta\theta}} \tag{2.12}$$

$$\mathbf{e}_{\hat{\phi}} = \alpha\partial_t + \beta\partial_\phi. \tag{2.13}$$

The orthonormality conditions $\mathbf{e}_{\hat{\phi}} \cdot \mathbf{e}_{\hat{r}} = 0$ and $\mathbf{e}_{\hat{\phi}} \cdot \mathbf{e}_{\hat{\theta}} = 0$ are trivially satisfied, and the conditions $\mathbf{e}_{\hat{\phi}} \cdot \mathbf{e}_{\hat{\phi}} = 1$ and $\mathbf{e}_{\hat{\phi}} \cdot \mathbf{e}_{\hat{t}} = 0$ determine α and β to be

$$\alpha = \frac{-g_{t\phi} - g_{\phi\phi}\Omega_{\rm k}}{\sqrt{\left(g_{t\phi}^2 + g_{tt}g_{\phi\phi}\right)\left(g_{tt} + 2g_{t\phi}\Omega_{\rm k} + g_{\phi\phi}\Omega_{\rm k}^2\right)}} \tag{2.14}$$

$$\beta = \frac{g_{tt} + g_{t\phi}\Omega_{\rm k}}{\sqrt{\left(g_{t\phi}^2 + g_{tt}g_{\phi\phi}\right)\left(g_{tt} + 2g_{t\phi}\Omega_{\rm k} + g_{\phi\phi}\Omega_{\rm k}^2\right)}}. \tag{2.15}$$

Transformations of a four vector in Boyer-Lindquist coordinates can be effected by dotting with the four basis vectors (giving, up to a sign for the zero-component, the coordinates in the accretion disk frame), and by multiplying the accretion disk coordinates with the respective basis vectors in Boyer-Lindquist coordinates.

2.4 The Warped Accretion Disk

This section is adapted from Abarr and Krawczynski [3], where I originally presented my warped disk model. I represent a warped accretion disk as residing in two planes, with a clean break between the two regions. For radial coordinates $r \leq r_{\rm BP}$, I use a standard equatorial accretion disk at a polar angle $\theta = \frac{\pi}{2}$. In the Kerr metric, inclined test particle orbits precess and have cork-screw type shapes [e.g. 94, 163, 95]. I assume that viscous stresses force the disk material for $r > r_{\rm BP}$ into orbits of constant r inclined by an angle β relative to the equatorial plane.

The plane of the disk is defined by the solutions of

$$\cos(\theta)\cos(\beta) - \sin(\theta)\cos(\phi)\sin(\beta) = 0. \tag{2.16}$$

The disk thus extends from an inclination of $\theta = 90°-\beta$ at $\phi = 0°$ to $\theta = 90°+\beta$ at $\phi = 180°$ (Fig. 2.1). The left-hand side of Eq. 2.16 is positive above the disk and negative below, and so a photon scatters off the inclined disk when this value changes sign.

The Boyer-Lindquist coordinates of a disk segment are given by

$$x^\mu(t, r) \; = \; (t, r, \theta(t), \phi(t)). \tag{2.17}$$

To find the angles θ and ϕ, I first parameterize a circular orbit in the equatorial plane at radial coordinate r around a black hole with spin parameter $a \in [-1, +1]$. This orbit has the Keplerian angular velocity

$$\Omega_{\rm K} \; = \; (a + r^{3/2})^{-1}. \tag{2.18}$$

Tilting the orbit by the angle β gives

$$\theta = \arccos\left(\sin\beta\cos\left(\Omega_{\rm K} t\right)\right) \tag{2.19}$$

$$\phi = \arctan\left(\sec\beta\tan\left(\Omega_{\rm K} t\right)\right). \tag{2.20}$$

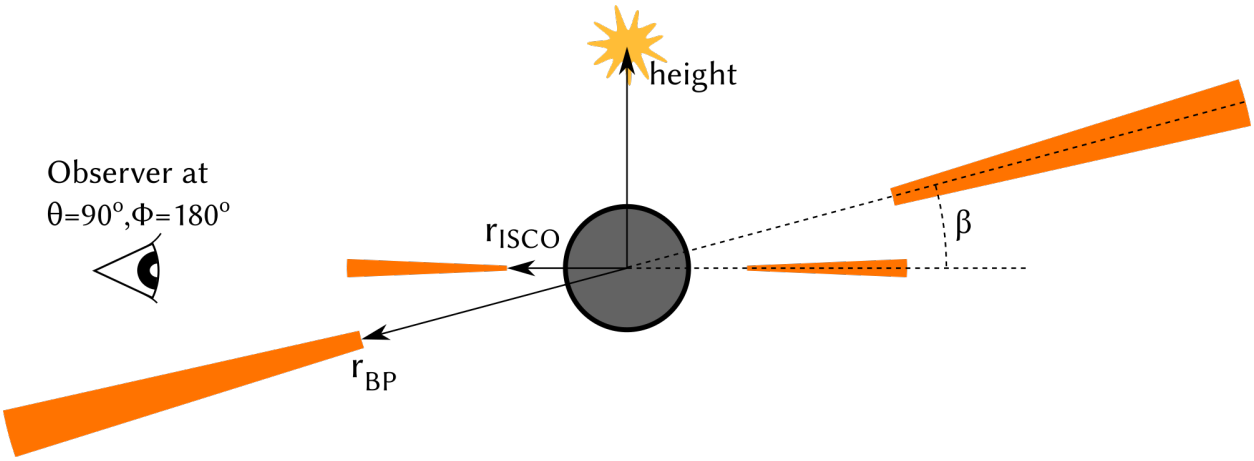

Fig. 2.1: The warped disk configuration, including the lamppost corona. The angular momentum of the inner accretion disk is aligned with the black hole spin axis. At r_{BP}, there is a tilt of β between the inner and outer disks. Shown is an example observer at an inclination of $\theta = 90°$, $\phi = 180°$. I use the spherical Boyer-Lindquist coordinates with $\theta = 0°$ pointing along the spin axis of the black hole. For $\theta = 90°$, $\phi = 0°$ points to the right, $\phi = 180°$ points to the left, and $\phi = 270°$ points to the reader.

Reflection off the inclined disk requires a different tetrad for the rest frame of these inclined orbits; I label this new tetrad $\mathbf{e}_{\hat{a}}$ with $a = 0, 1, 2, 3$. The four components of the tetrad are roughly analagous to t, r, θ, and ϕ, though inclined orbits require mixing of t, θ, and ϕ rather than just t and ϕ as in the equatorial case.

The first basis vector $\mathbf{e}_{\hat{0}}$ is simply the four velocity of the disk material $\mathbf{u} = dx^{\mu}/d\tau$. The four velocity is proportional to dx^{μ}/dt but is normalized to -1. I choose $\mathbf{e}_{\hat{1}}$ and $\mathbf{e}_{\hat{3}}$ to be tangent to the inclined disk: $\mathbf{e}_{\hat{1}} \propto \partial_r$, and $\mathbf{e}_{\hat{3}}$ is the component of the vector tangent to the particle orbit that is also perpendicular to $\mathbf{e}_{\hat{0}}$ and $\mathbf{e}_{\hat{1}}$. The last basis vector $\mathbf{e}_{\hat{2}}$ is the component of the gradient across the disk perpendicular to the first three basis vectors. For $\mathbf{e}_{\hat{2}}$ and $\mathbf{e}_{\hat{3}}$ I get the components perpendicular to the other basis vectors by using Gram-Schmidt orthonormalization to subtract out the parallel components with the help of the metric.

In terms of the Boyer-Lindquist basis vectors ∂_μ, the new basis vectors are given by:

$$\mathbf{e}_{\hat{0}} = \left(\partial_t + \Omega_{\rm K} \sin\beta \sin\phi \partial_\theta + \Omega_{\rm K} \cos\beta \csc^2\theta \partial_\phi\right)/\sqrt{\Sigma} \tag{2.21}$$

$$\mathbf{e}_{\hat{1}} = \partial_r/\sqrt{g_{rr}} \tag{2.22}$$

$$\mathbf{e}_{\hat{2}} = \frac{\sqrt{g_{\theta\theta}}\sin\beta\sin\phi}{\sqrt{\zeta\left(g_{t\phi}^2 - g_{tt}g_{\phi\phi}\right)}}\left(g_{t\phi}\partial_t - g_{tt}g_{\phi\phi}\partial_\phi\right) - \sqrt{\frac{g_{t\phi}^2 - g_{tt}g_{\phi\phi}}{\zeta g_{\theta\theta}}}\cos\beta\csc^2\theta\partial_\theta \tag{2.23}$$

$$\begin{aligned}\mathbf{e}_{\hat{3}} = \Big[&\left(-g_{t\phi}\cos\beta\csc^2\theta - g_{\phi\phi}\Omega_{\rm K}\cos^2\beta\csc^4\theta - g_{\theta\theta}\Omega_{\rm K}\sin^2\beta\sin^2\phi\right)\partial_t \\ &+ \left(g_{tt} + g_{t\phi}\Omega_{\rm K}\cos\beta\csc^2\theta\right)\left(\sin\beta\sin\phi\partial_\theta + \cos\beta\csc^2\theta\partial_\phi\right)\Big] \\ &\div\sqrt{\Sigma\cos^2\beta\csc^4\theta\left(g_{t\phi}^2 - g_{tt}g_{\phi\phi}\right) + g_{tt}g_{\theta\theta}\sin^2\beta\sin^2\phi}\end{aligned} \tag{2.24}$$

where

$$\Sigma = -g_{tt} - \Omega_{\rm K}\left(2g_{t\phi}\cos\beta\csc^2\theta + g_{\phi\phi}\Omega_{\rm K}\cos^2\beta\csc^4\theta + g_{\theta\theta}\Omega_{\rm K}\sin^2\beta\sin^2\phi\right) \tag{2.25}$$

$$\zeta = \left(g_{t\phi}^2 - g_{tt}g_{\phi\phi}\right)\cos^2\beta\csc^4\theta - g_{tt}g_{\theta\theta}\sin^2\beta\sin^2\phi. \tag{2.26}$$

Equations 2.21-2.24 are only valid in the upper hemisphere of the inclined disk, so I restrict photon emission to $k^\theta < 0$. It is possible that a photon emitted from the inner disk near $\phi = 0°$ scatters off the bottom of the outer disk, or a photon emitted from the outer disk near $\phi = 180°$ scatters off the bottom of the inner disk, in which case the reflected photon would be emitted back into the lower hemisphere. In these cases, I take advantage of the symmetry of the disk to 'mirror' the reflected photon into the upper hemisphere with

$$\theta \to \pi - \theta$$

$$\phi \to \phi + \pi$$

$$k^\theta \to -k^\theta$$

$$f^\theta \to -f^\theta.$$

This changes our tracked photon into the equivalent photon which was initially emitted into the *lower* hemisphere and scattered into the *upper* hemisphere. During analysis, I perform this same transformation to any photons arriving in the lower hemisphere to account for their mirrored twins initially emitted into the lower hemisphere.

Chapter 3

Polarization of Thermal Emission from Warped Accretion Disks

3.1 Introduction

The majority chapter is adapted from Abarr and Krawczynski [3]. I produced all of the simulated data, performed all of the analysis, and wrote the majority of the text.

As mentioned in Chapter 1, at least half of black holes in binaries may have angular momenta significantly misaligned with the angular momenta of the orbiting companion due to the kick from the supernova [18]. One of the strongest cases for misalignment is GRO J1655-40, whose binary and jet inclinations disagree by $\sim 15^\circ$ [70, 64]. If this misalignment causes a persistent warp in the accretion disk like what Bardeen and Petterson [8] predicted, a signature of this warp should be carried in the polarization signal due to the strong dependence of polarization on disk inclination.

In this chapter, I show the effect that a warped disk configuration similar to that of Liska et al. [95] has on the polarization of the thermal emission from the accretion disk. I limit the discussion to a single warp configuration viewed from different azimuthal viewing angles, and compare the observational signatures to those of the standard equatorial geometrically thin, optically thick disk. Cheng et al. [31] previously studied the polarization of warped disks around a non-spinning and a spinning black hole with a misalignment of 30° and r_{BP}

between 30 and 1000 r_g, and I improve on their work in several ways. As our code tracks photons forward in time, it allows us to model single and multiple reflections of photons off the inner and outer portions of the accretion disk. In contrast, Cheng et al. [31] included only single reflections of photons from the inner disk reflecting off the outer disk.

Section 3.2 compares the results for a warped disk to a standard disk aligned in the equatorial plane, showing the impact of the warp on the flux and polarization energy spectra. I examine the results and study the impact of the azimuthal viewing angle, and the reflections off different disk sections on the flux and polarization spectra. In Section 3.3, I investigate the possible polarization signal from two sources which may contain warped disks. In Section 3.4, I discuss the results and emphasize the opportunities to explore the dynamics of warped disks with upcoming and future X-ray polarization measurements.

3.2 Polarization of Thermal Emission

I focus on a single warped disk configuration around a stellar mass black hole. I choose a black hole with a spin of 0.9, r_{BP} of 8 r_g, and a misalignment of 15°. The black hole has a mass of 10 $M_\odot$ and an accretion rate of 8.98×10^{18} g/s, or 0.5 $\dot{M}_E$.

I generate 3.5×10^8 photon packages between r_{ISCO}=2.32 r_g and 100 r_g for the warped disk, and compare the results to those for 10^7 photons generated for a standard equatorial disk. The former case requires more photons due to the lack of azimuthal symmetry. For each observer, I collect all photons within 4° of the location of the observer.

I will discuss in the following the observers at a constant inclination of $i_{in} = 75°$ measured from the angular momentum vector of the black hole and the inner disk. In Table 3.1 I list the eight observers analyzed, each with a different azimuthal angles ϕ starting at $\phi = 90°$; for clarity, I label each observer with their azimuth ϕ in the form Obϕ. Given the inner disk inclination i_{in} (tied to the observer location θ), ϕ, and β, the inclination of the outer disk is

$$i_{out} = \arccos\left(\cos i_{in} \cos\beta - \sin i_{in} \cos\phi \sin\beta\right). \tag{3.1}$$

Thus, for Ob90, the outer disk is inclined at $i_{\rm out} = 75.52°$, almost the same as $i_{\rm in}$.

We can distinguish between three classes of events: total emission, direct emission, and reflected emission off the whole disk. Figure 3.1 shows black hole images for the three event classes, with their polarization plotted on top. The direct emission (bottom left panel) is polarized along the plane of disk from which it emits; this is more obvious for the outer disk, where the emission is less affected by light bending. The front of the inner disk is more horizontally polarized than the outer disk, and its back is more weakly polarized since the strong light bending causes this part of the disk to be viewed at a lower inclination angle. The reflected emission (bottom right panel) shows high degrees of polarization, and tends to come from the region close to the black hole. On the left side of the black hole, where the emission is beamed towards the observer, photons can reflect at radii of up to 15 or $20\,{\rm r_g}$; for a fully aligned disk, almost all scattering of returning radiation should occur within $10\,{\rm r_g}$.

Figure 3.2 shows the energy spectrum, polarization fraction, and polarization angle for the observer Ob90 and compares it to the total emission from two different unwarped disks: the completely aligned disk lies in the equatorial plane of the black hole, and the completely misaligned disk lies in the plane of the binary orbit (the same plane as the outer disk in the warped case). It is important to note that for both the completely aligned disk and the completely misaligned disk the angular momenta of the black hole and disk are aligned; these are only 'misaligned' in the sense that they represent unwarped disks in the same plane as the inner and outer disks, respectively. The flux and polarization fraction of the warped disk are very similar to those of the completely aligned disk. The polarization angle of the warped disk configuration, however, is shifted by $\sim 15°$ and roughly matches the angle of the completely misaligned disk. It matches particularly well at low energies, where direct emission from the outer disk dominates, and seems to settle back down at high energies where the reflected emission dominates.

In Figure 3.3, the reflected emission is split into two parts: emission reflected off the outer disk and emission reflected off the inner disk. There is a third component which reflects

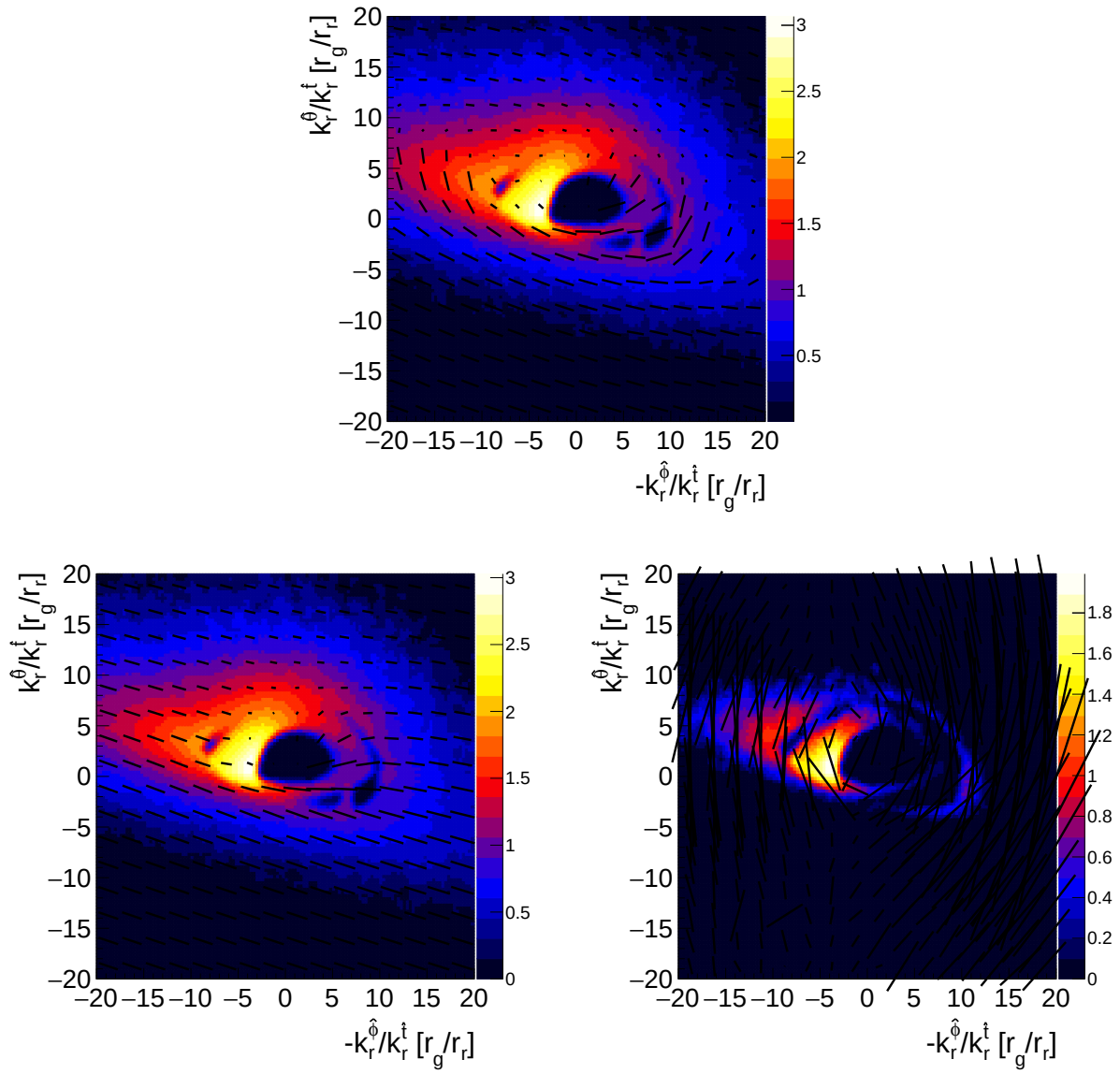

Fig. 3.1: The three emission types: Total emission (top), direct emission (bottom left), reflected emission (bottom right). The color bar gives the surface brightness in logarithmic units. Over the images is plotted the polarization, where the length of the black bars gives the polarization fraction and the orientation gives polarization angle.

Observer	ϕ-viewing angle	i_{out}	Figure
Ob90	90°	75.52°	3.1, 3.2
Ob135	135°	64.74°	3.4
Ob180	180°	60°	3.5
Ob225	225°	64.74°	3.6
Ob270	270°	75.52°	3.7
Ob315	315°	85.8°	3.8
Ob0	0°	90°	3.9
Ob45	45°	85.8°	3.10

Tab. 3.1: Summary of the eight observers in this work. For each, the inner disk inclination is fixed at 75°.

off both disks, but this is a comparatively small effect. The overall reflected polarization fraction and angle clearly falls between the two components, with the outer disk component being more highly polarized than the inner disk.

3.2.1 Azimuthal Dependence of the Polarization Signature

Ob135 (Figure 3.4) sees a slightly softer energy spectrum since more of the outer disk is visible and thus more direct emission is reaching the observer. The polarization fraction is slightly lower than in the completely aligned disk. At low energies, though, it matches the completely misaligned disk well. The polarization angle roughly matches the completely misaligned disk, which is offset from the completely aligned disk by ∼12°; this is the angle the observer sees between the angular momentum axes of the inner and outer disks.

Qualitatively, the flux and polarization fraction seen by Ob180 (Figure 3.5) match that seen by Ob135 (Figure 3.4). The polarization fraction, though, matches the completely aligned disk instead of the completely misaligned disk. Cheng et al. [31] reported that the warped disk polarization angle matched that of their completely aligned disk. Their system orientation was limited to one similar to our Ob180 (Figure 3.5), though; the previously examined observers make it clear that in general this is not the case.

Ob225 (Figure 3.6) and Ob270 (Figure 3.7) are qualitatively similar to Ob135 and Ob90,

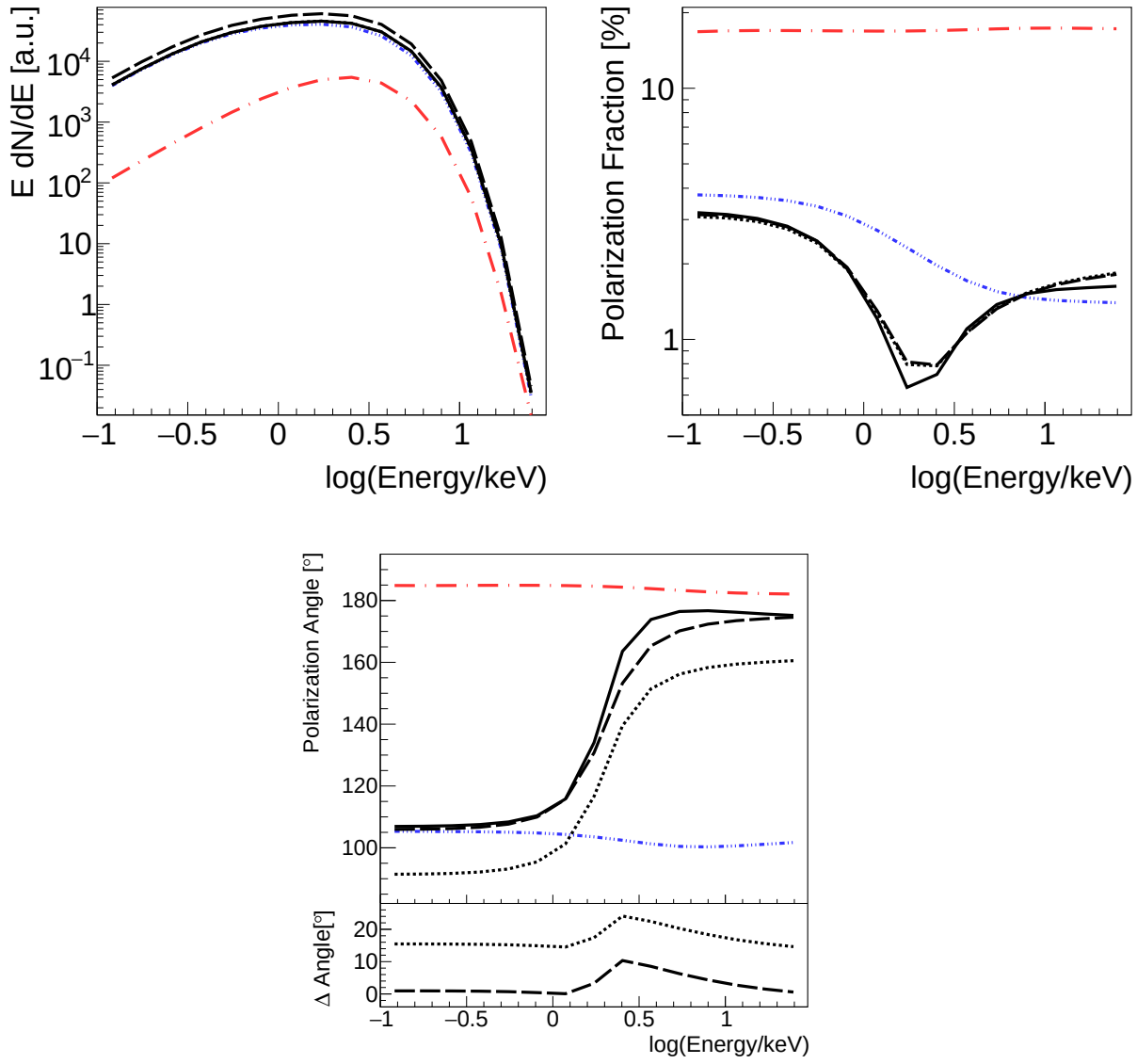

Fig. 3.2: Energy spectrum (top left), polarization fraction (top right), and polarization angle (bottom) for the warped disk simulations ($r_{BP} = 8\,r_{\rm g}$, $\beta = 15°$) and selected results from the equatorial disk for an observer at $\theta = 75°$ and $\phi = 90°$. Included are the total emission (thick black), direct emission (dash-dot-dotted blue), and reflected emission (dash-dotted red). These are compared to the total emission of the completely aligned (equatorial) disk (dotted black) and the completely misaligned disk (dashed black). The bottom panel of the polarization angle plot shows the difference between the warped disk and the aligned disks.

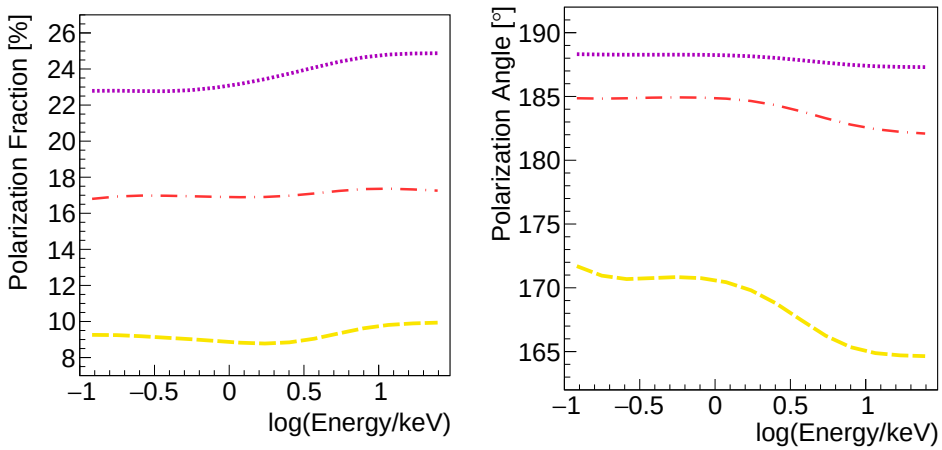

Fig. 3.3: Polarization of the reflected emission (dash-dotted red) from Fig. 3.2 split up into the portion reflected only off the inner disk (dashed yellow) and only off the outer disk (dotted purple).

respectively, since their outer disk inclinations match.

Ob315 (Figure 3.8) sees the outer disk almost edge on, and thus sees fewer photons from it. The light that curves around the bottom of the black hole is visible, which is not true of the completely aligned disk. This means the warped disk produces a slightly harder spectrum than the completely aligned disk. This may only be true for our razor thin disk model, however; in a physical disk, the vertical extension at large radii may block the emission curving around the bottom. The polarization fraction of the warped disk fits squarely between two aligned disks. Polarization angle even further deviates from either aligned disk at high energies; it appears to carry the difference between the two aligned disks at low energies up past the swing, presumably because many of the high energy photons emitted from the inner disk are scattering off the inclined outer disk instead. This gives us a clear indication that the polarization angle does not always line up with either that of the inner or outer disks.

Ob0 (Figure 3.9) sees the outer disk fully edge on, and thus is somewhat qualitatively similar to Ob315 (Figure 3.8). The polarization angle, though, fully matches the inner disk; in this sense, Ob0 is similar Ob180 (Figure 3.5), since to both of these observers the angular momentum axes of both disks appear to be parallel.

The last azimuth, for Ob45, is shown in Figure 3.10, and is qualitatively similar to Ob315.

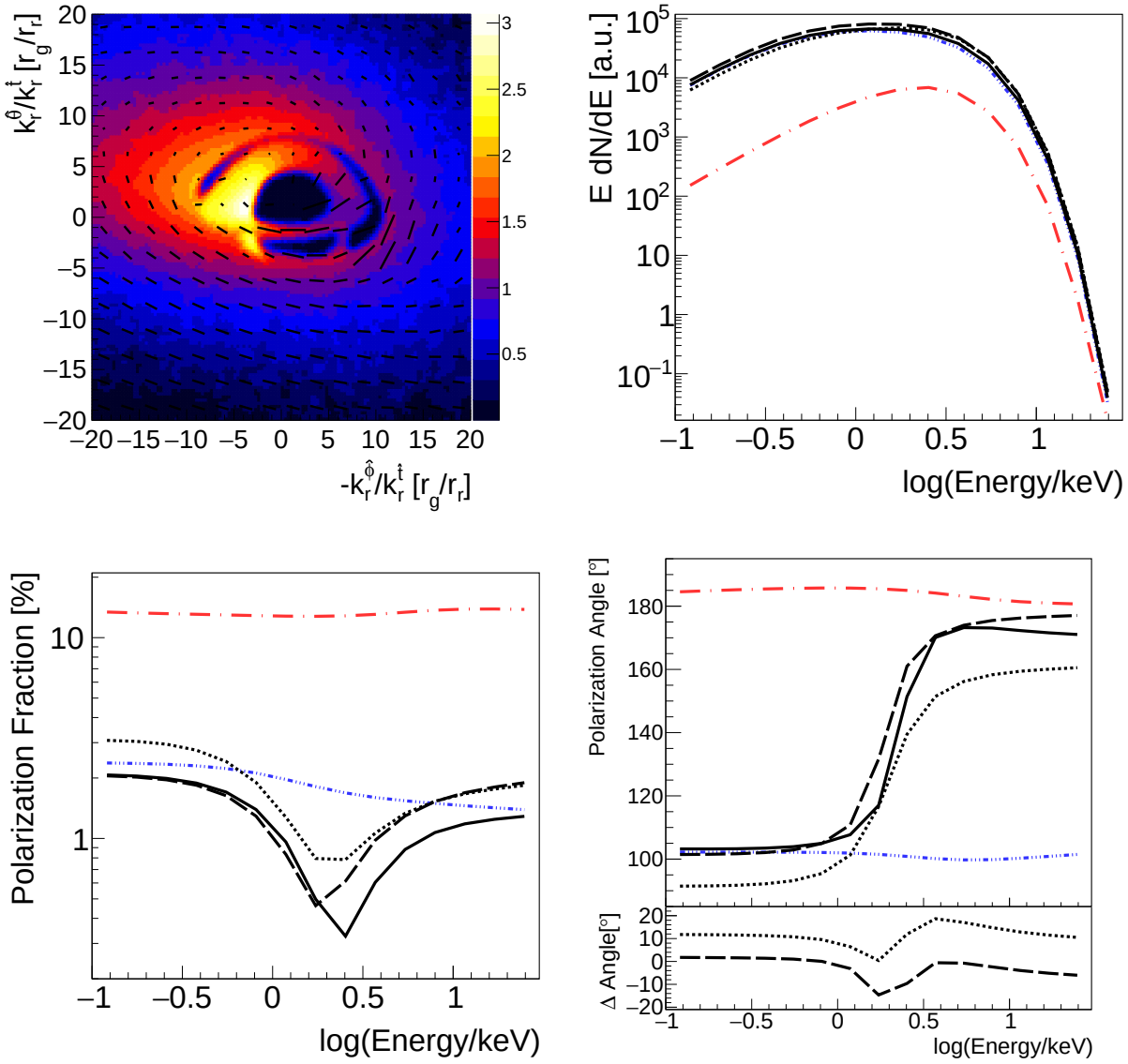

Fig. 3.4: Image of the black hole (top left), energy spectrum (top right), polarization fraction (bottom left), and polarization angle (bottom right) seen by Ob135. Included are the total emission, direct emission, and reflected emission of the warped disk, as well as the total emission of the completely aligned and completely misaligned disks. This uses the same style conventions as in Figure 3.2.

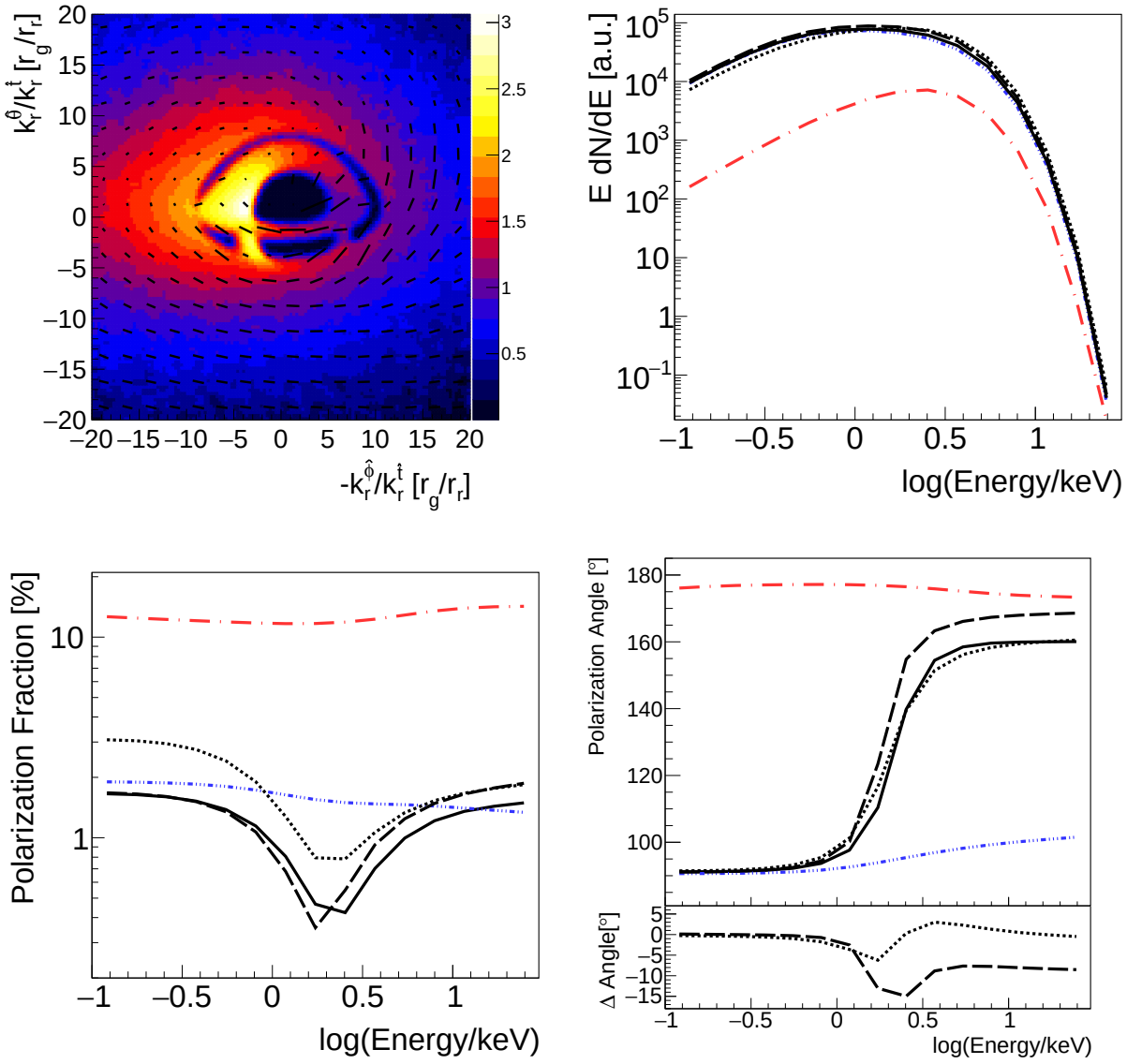

Fig. 3.5: As in Figure 3.4, but for Ob180.

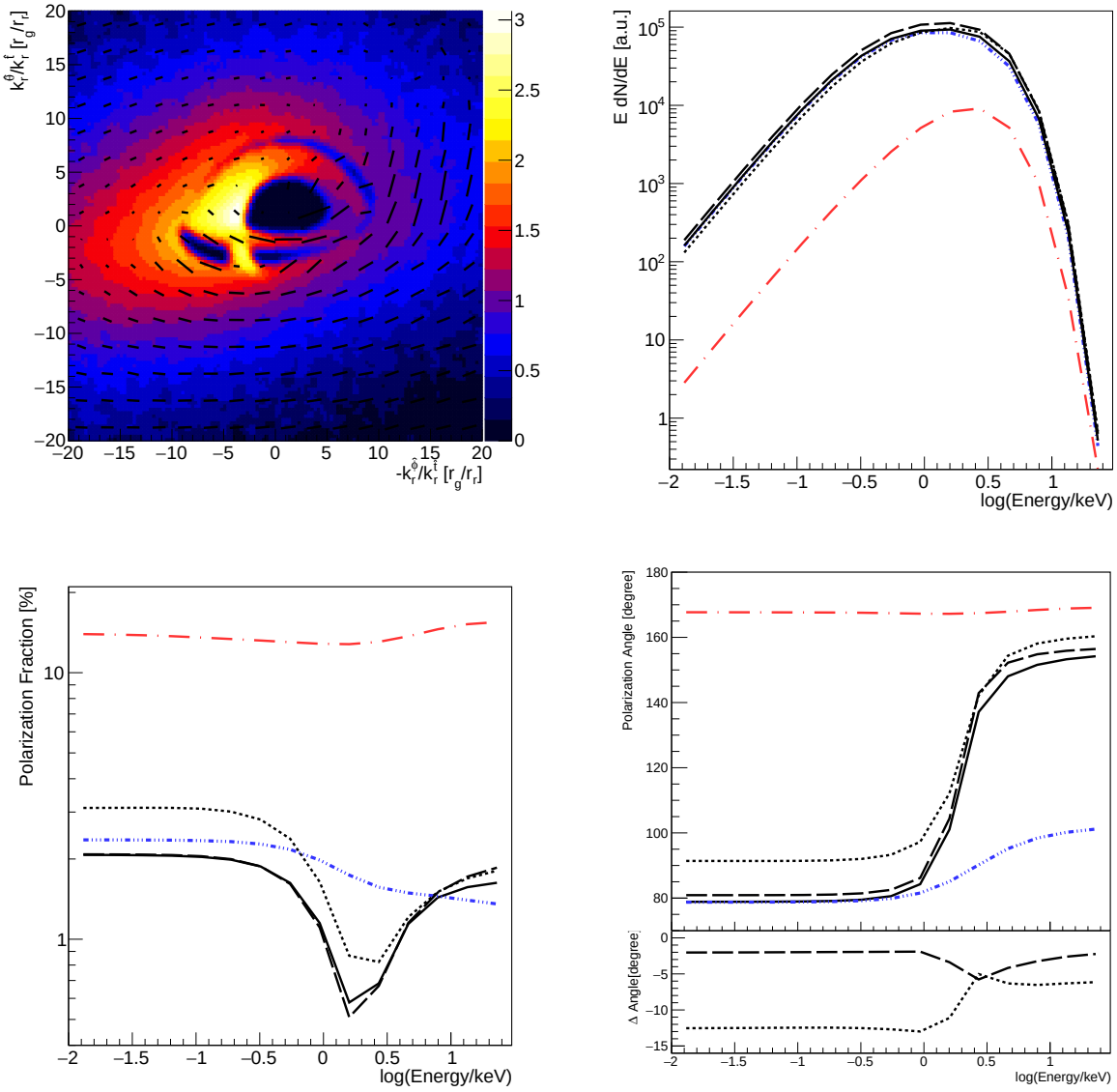

Fig. 3.6: As in Figure 3.4, but for Ob225.

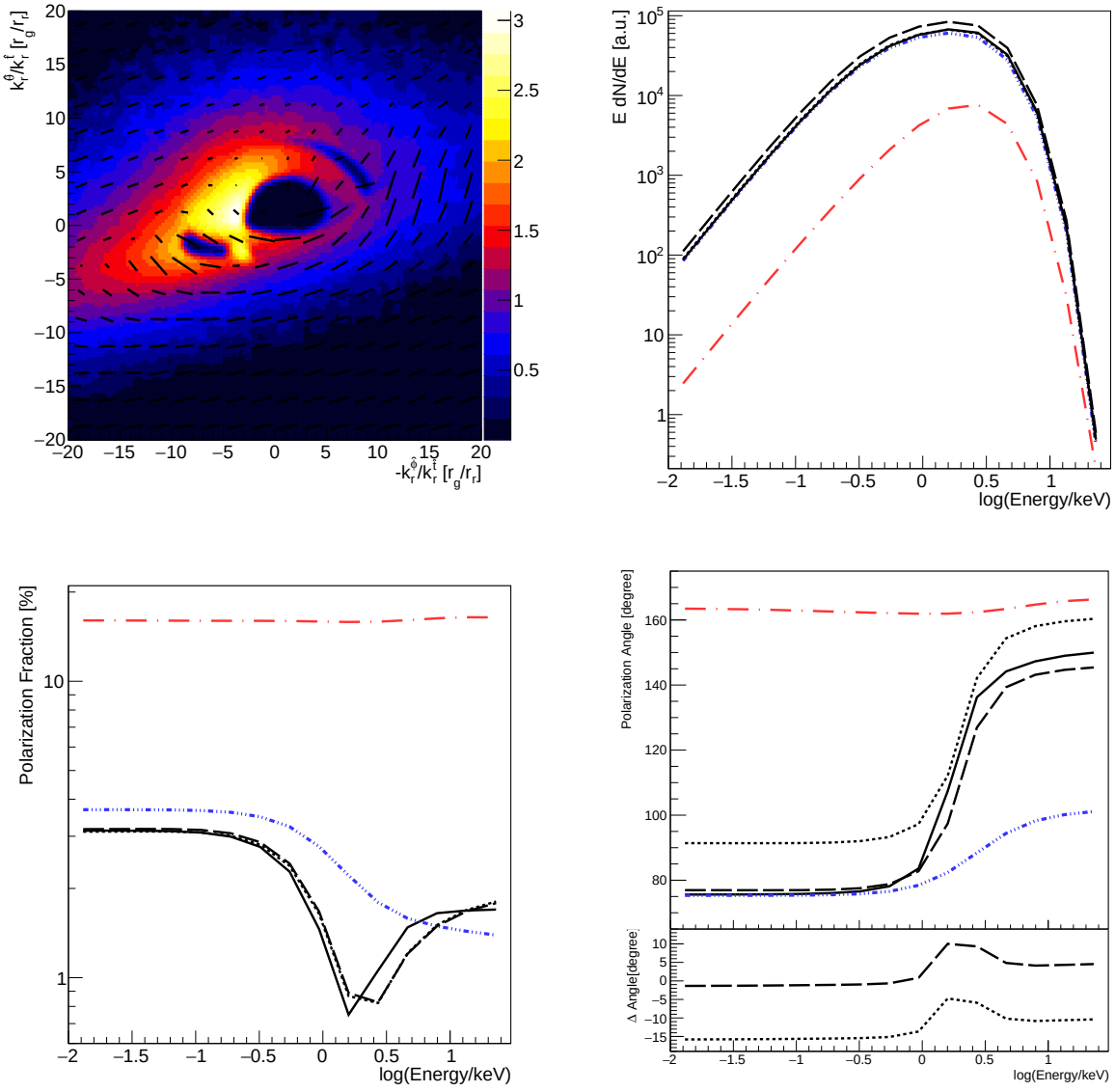

Fig. 3.7: As in Figure 3.4, but for Ob270.

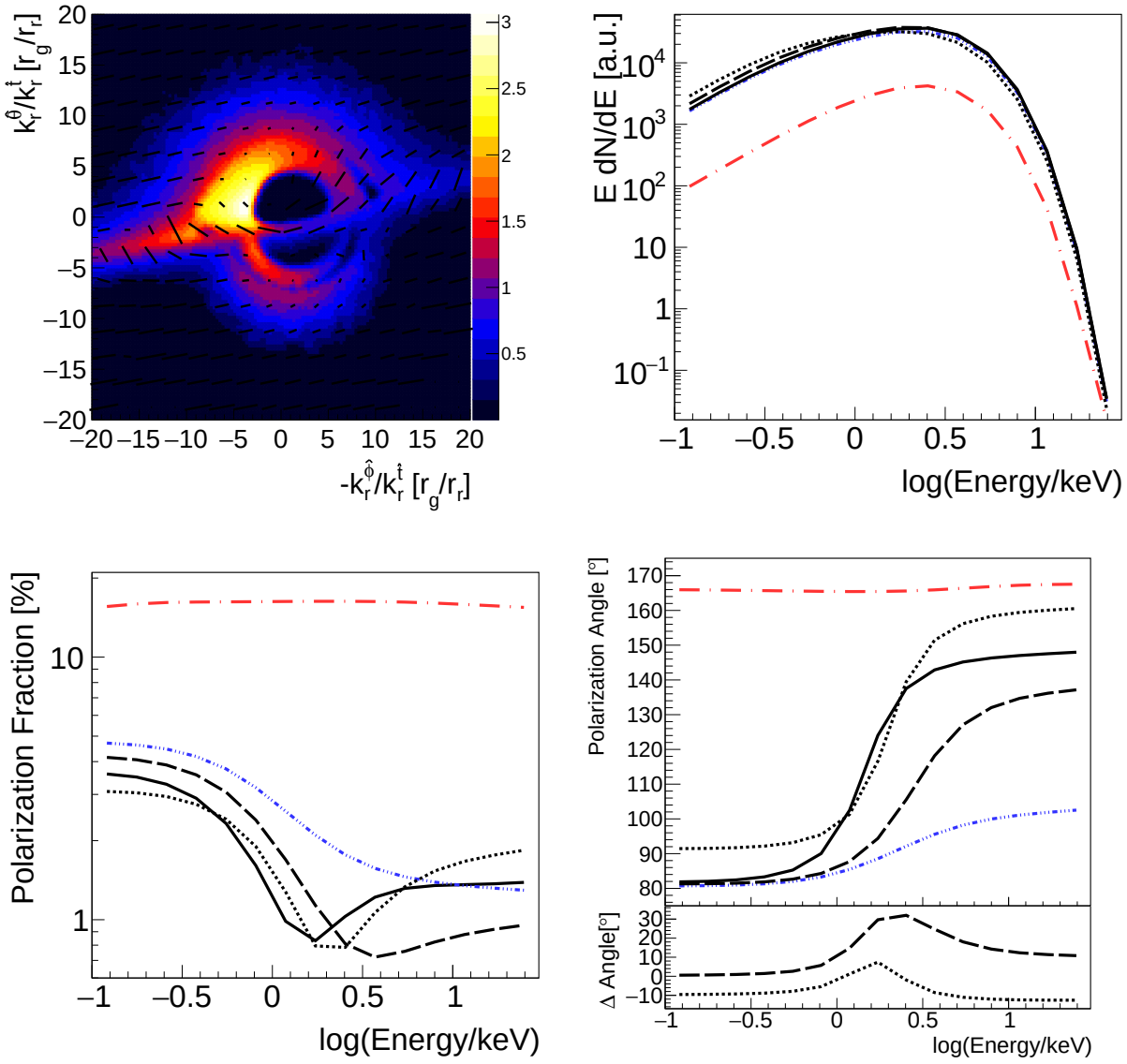

Fig. 3.8: As in Figure 3.4, but for Ob315.

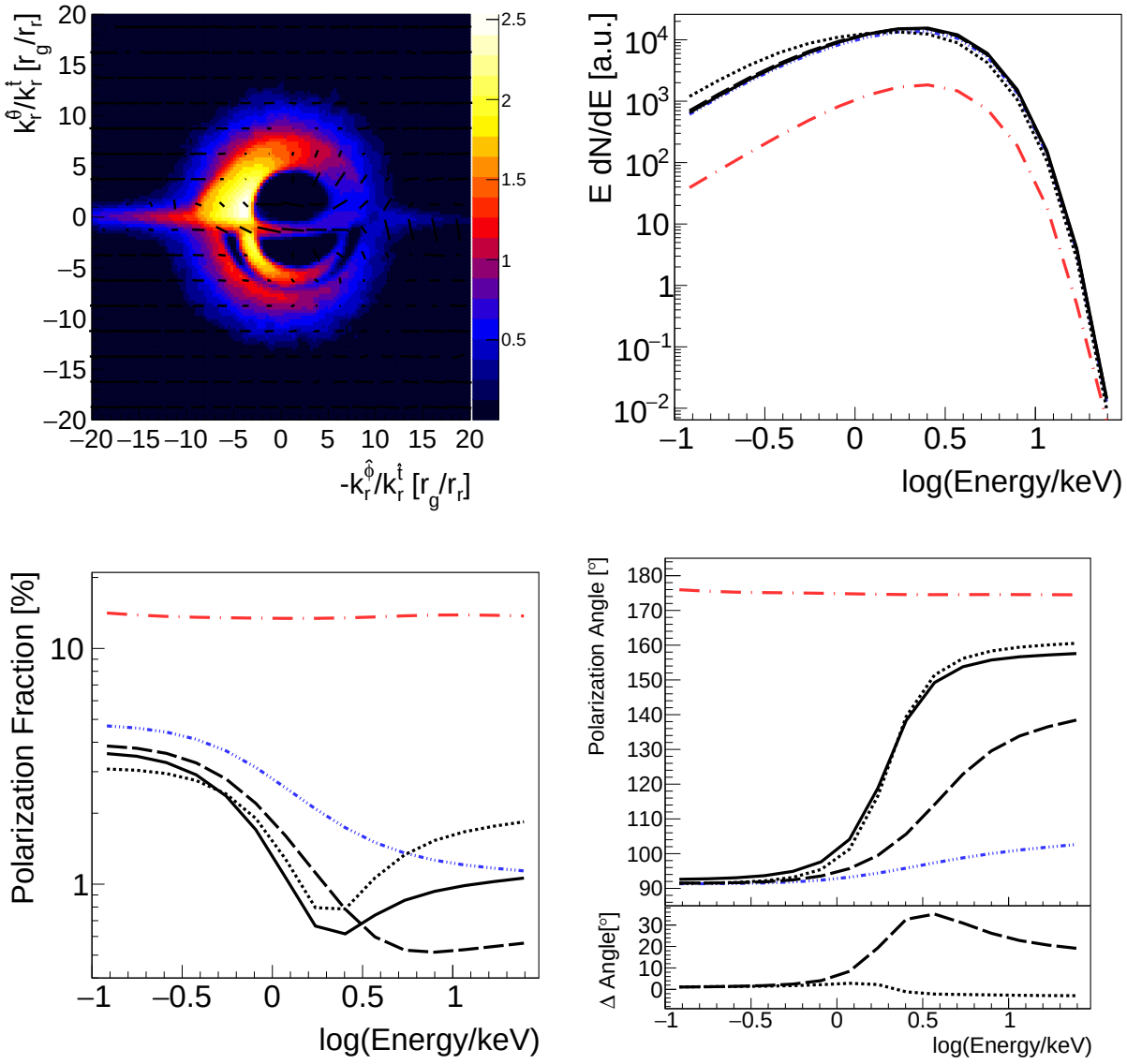

Fig. 3.9: As in Figure 3.4, but for Ob0.

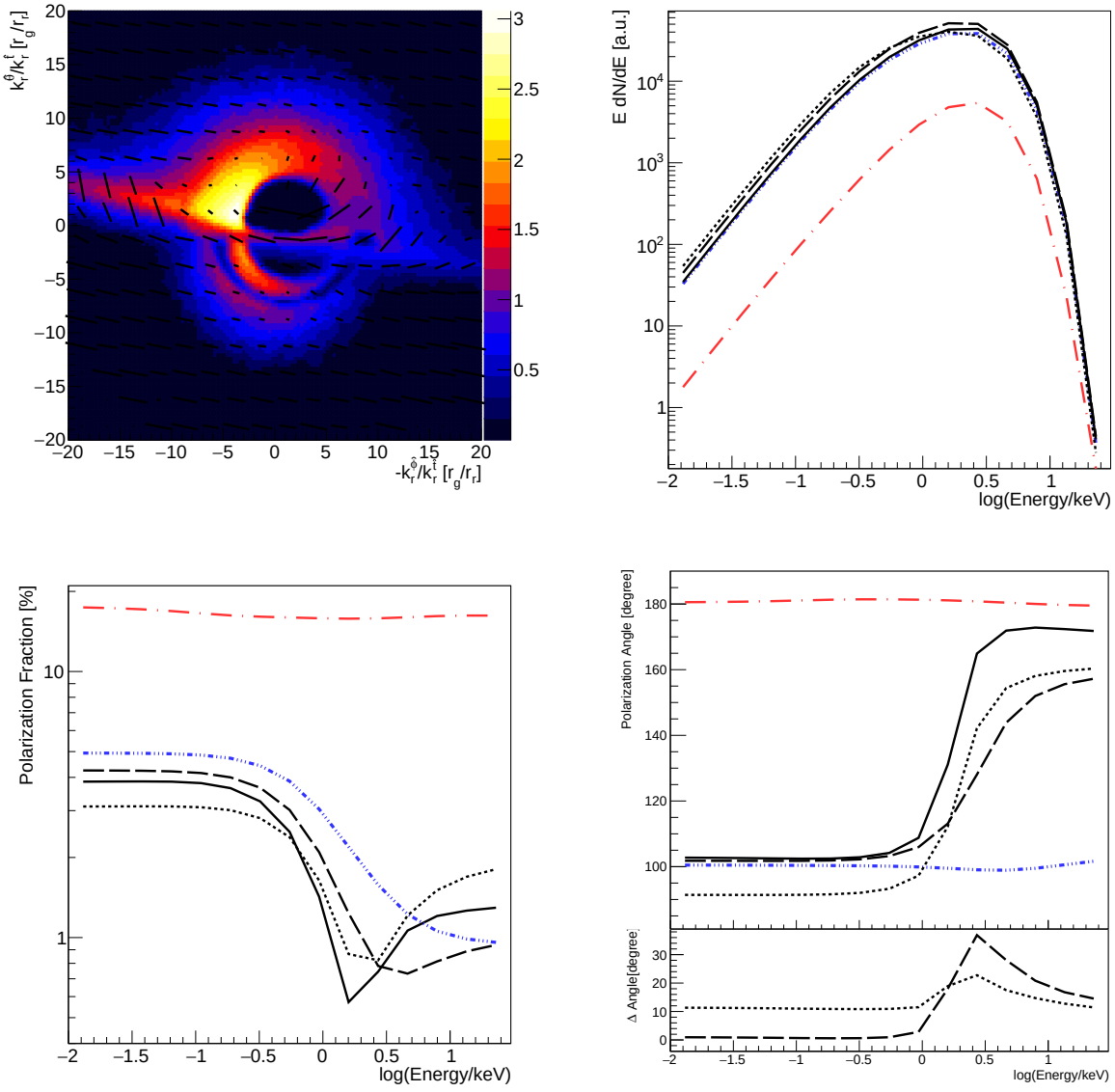

Fig. 3.10: As in Figure 3.4, but for Ob45.

3.2.2 Comparison to Earlier Results

Our results can be compared to Figure 5 of Cheng et al. [31] showing the polarization of disks with r_{BP} values between 30 and 1000 r_g. Their inner disk is inclined at 75°, matching ours, while their inner disk is at 45°; this corresponds to a $\beta = 30°$. They ignore radiation which is curved by the black hole, returns to disk, and is reflected, as well as radiation emitted from the outer disk and reflected by the inner disk. They find that the disk warp does not affect the polarization angle, but that it is imprinted on a transition in the polarization fraction from matching the inclination of the outer disk at low energies to matching the inner disk at high energies, with the transition changing with r_{BP}.

My results show that in general the polarization does not behave so predictably. At low energies, where the polarization is dominated by the direct emission from the outer disk, the polarization angle matches the case of the completely misaligned disk. Polarization fraction at high energies either matches or is lower than that of the completely aligned disk, while it can be higher or lower than the completely misaligned disk depending on the observer. Polarization angle tends to be offset from the completely aligned disk by the rotation between the two disk axes. When there is no visible rotation between the axes of the outer and inner parts of the warped disk (i.e. the outer disk is tilted directly towards or away from the observer), the polarization angle matches the completely aligned disk. For every other observer, the polarization angle roughly matches the completely misaligned disks until the observer sees the warped outer disk close to edge on; in these cases, the scattered X-rays at high energies carry the angle of rotation between the inner and outer disks.

Thus, with some measure of the jet direction, the polarization angle can give a lower limit on the misalignment between the inner and outer disks. Cheng et al. [31] note that the energy at which the polarization fraction transitions from that of the outer disk inclination to the inner disk inclination is inversely related to r_{BP}. Since the closest of our observers to theirs is Ob180 (Figure 3.5), where the polarization fraction is lower across the board, I assume that the transition energy corresponding to $r_{BP} = 8\,r_g$ is greater than the energy range of

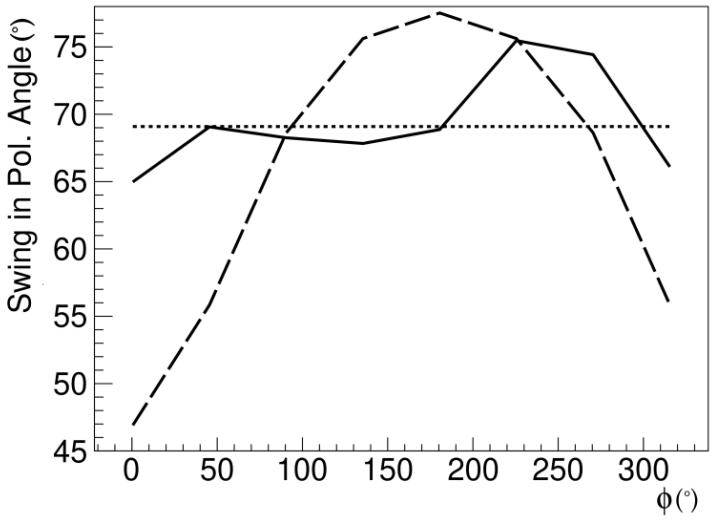

Fig. 3.11: The swing in polarization angle over this inclination. Shown are for the warped disk (solid black), the fully aligned disk (dotted), and fully misaligned disk (dashed).

our analysis. I also note that this is not true for other observers, where the misalignment is not entirely measured by the difference in inclinations between the inner and outer warped disks.

To see how these observers might be distinguished, Figure 3.11 shows the swing in polarization angle for each warped disk, completely misaligned disk, and the completely aligned disk. This shows us that the warped disk at this inclination has a swing that could always be mistaken for an aligned disk.

3.3 Potential Sources with Warped Accretion Disks

Cygnus X-1

The inclination of the binary orbit of Cygnus X-1 has been measured to be $(27.1 \pm 0.8)^\circ$ [129], while the inclination of the reflecting region (likely the innermost part of the accretion disk) has been measured to be $\sim 40^\circ$ [149, 155]. I simulated one possible polarization of this system based on these measured values, taking the value of the tilt to be 15°, roughly the observed angle of misalignement. This is not a trivial assumption, however: the tilt could

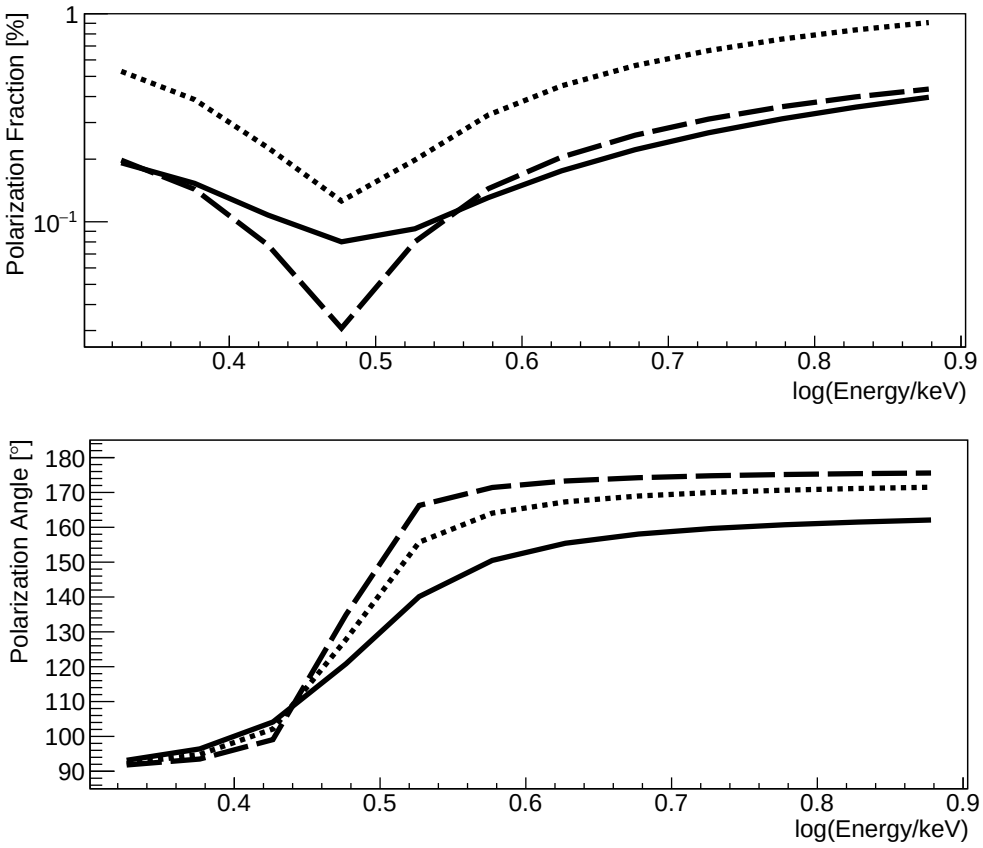

Fig. 3.12: Possible polarization fraction and direction for Cygnus X-1, based on disagreement between measured inclinations of the system. This polarization assumes an observer located at $\phi = 180°$ such that the tilt angle is entirely carried in the visible misalignement. Included are the polarization for the warped disk (solid line), fully aligned disk (dotted), and fully misaligned disk (dashed).

be 30° if we are observing the system from $\phi = 137°$. Figure 3.12 shows these results in the energy range of IXPE. It shows that the warped disk sees a swing in polarization angle that differs from either aligned disk by >10°. Due to the low inclination of the system, however, the degree of polarization is incredibly low; a very long observation would be required to achieve an MDP this small.

Recent results indicate that the inner disk inclination may be much closer to binary orbit inclination; the previous results required iron abundances upwards of an order of magnitude greater than solar values. Tomsick et al. [150] fit data from NuSTAR and Suzaku and found that by keeping the iron abundance at the solar value and increasing the inner edge of the

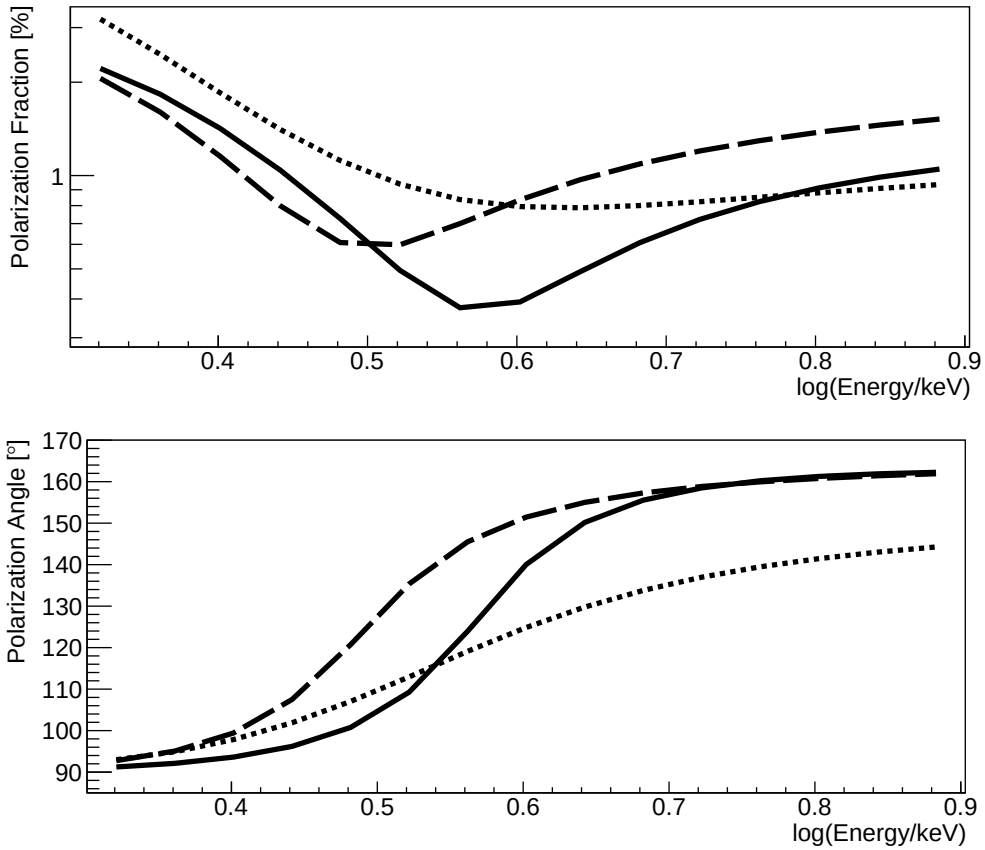

Fig. 3.13: Possible polarization fraction and direction for GRO J1655-40, based on disagreement between measured inclinations of the system. Polarization is shown for the warped disk (solid line), fully aligned disk (dotted), and fully misaligned disk (dashed).

disk to $\sim 3\,r_{ISCO}$, the inclination drops to $\sim 20°$. While this does not exactly agree with the value found by Orosz et al. [129], it does cast doubt on the possibility that Cygnus X-1 contains a warped disk.

GRO J1655-40

GRO J1655-40, another binary black hole, has a disagreement of $\sim 15°$ between measured inclinations: Hjellming and Rupen [70] measured the inclination of the radio jet at $(85 \pm 2)°$, while Greene, Bailyn, and Orosz [64] measured the binary orbit inclination at $(70.2 \pm 1.9)°$. Offering the same caveat as before that I have assumed the measured misalignement is equal to the warp angle, I have plotted the polarization for GRO J1655-40 in Figure 3.13. We see that the swing in polarization angle differs significantly from both aligned cases; it is

$\sim$20° higher than the swing by a aligned disk with the inclination of the jet. Though the inclination of the system is higher than Cygnus X-1, the polarization fraction is still quite low, never surpassing 2 %. So, although this makes a slightly better target than Cygnus X-1, it would still require a long observation to see such low polarization levels.

3.4 Discussion

In this chapter, I examine the spectropolarimetric signature of a warped accretion disk, similar to what might result from the Bardeen-Petterson effect. I find that small values of r_{BP} complicate the simple picture that the inner accretion disk properties are responsible for the polarization at high energies while the outer disk properties are responsible at low energies. Since most returning radiation scatters within $\sim 10\, r_g$, a small value for r_{BP} means that some of this radiation reflects off the outer disk. Figure 3.1 shows that the disk warp leads to a larger fraction of photons scattering at larger radii. Our results show that the measured polarization is highly dependent on the azimuthal viewing angle of the misaligned system, especially in regards to the polarization angle.

Since a warped disk does not affect the energy at which the polarization angle swings, polarization can still be used to measure black hole spin (see Fig. 7 in Schnittman and Krolik [138]). Similarly, the continuum-fitting method [107] is still valid as the spectrum is not significantly modified by the presence of a warped disk. The complication to using the continuum-fitting method is instead in assuming the inclination of the inner accretion disk based on eclipse observations (though jet inclinations are still valid). For a given source, then, polarimetric observations could tell us whether the binary plane inclination is an appropriate assumption. We may also expect to measure a lower misalignment with polarization than by comparing the jet and binary inclinations, as Liska et al. [95] showed that global alignment can make the disk warped smaller than the overall system misalignment.

I investigate the possible polarization measurement of Cygnus X-1 and GRO J165-40, two

binary black holes in which different measures of inclination disagree. I do not analyze all possible configurations due to the degeneracy between visible misalignment, warp angle, and azimuth, but for the simulated parameters both sources would show low polarization levels that would require very long observations.

Another possible target for observation is 4U 1957+11, a low-mass X-ray binary that is a black hole candidate. It is consistently in the spectrally soft state, and is likely highly spinning and highly inclined [123]. Most of the time it is well fit by a purely thermal spectrum, so would be a good test case for the results in this chapter.

Without some prior measure of the orientation of a system, we would be unable to interpret the polarization results. We are fortunate, then, that misaligned accretion is thought to be a driver of corona and jet formation in black hole binaries [85], and so an observed jet is an indication that the source would be a good target for polarimetric measurement. Another benefit to focusing on sources with visible jets is their association with a strong power law component; I expect that the time lag in the reflected power law emission from the corona will track r_{BP} and the misalignment, and in Chapter 4, I investigate the impact a warped disk has on the iron line profile resulting from reflected power law emission.

The Bardeen-Petterson effect has many interesting implications on the dynamics of accreting black holes, and polarimetry is in a unique position to examine this. X-ray polarimetry could confirm that the precession of the inner disk before its angular momentum is aligned with the black hole is the driver of quasi-periodic oscillations [74]. The BP effect could help explain state transitions in black hole X-ray binaries according to Nixon and Salvesen [118]. In their model, a warp or break in the disk is present in both the soft intermediate state (SIMS) and the thermal state, so we would expect to see some polarimetric signature of these, possibly of both the thermal and power law emission (which becomes prominent in the SIMS).

Chapter 4

Iron Line Profile from Warped Accretion Disks

4.1 Introduction

This chapter is adapted from Abarr and Krawczynski [2]. I produced all of the simulated data, performed all of the analysis, and wrote the majority of the text.

Emission lines are a powerful tool for probing the geometry and structure of the inner accretion flows of compact objects. In the case of stellar mass and supermassive black holes, the fluorescent iron Kα emission centered at 6.4 keV has proven to be a particular powerful diagnostic [see 136, 19, 108]. In some objects, this line is broadened by the gravitational redshift from the potential well and Doppler shift from the orbital motion of the disk plasma. The resulting profile is peaked both above and below 6.4 keV, with both blueshifted and redshifted 'horns'. The line shape depends on many parameters, including the emissivity profile of the disk, the ionization state of the disk material, the inner edge of the disk, and the inclination of the observer relative to the angular momentum vector of the disk. When studying the spectra of black holes, the inclination and spin of the black hole are often inferred from a fit to the data assuming that the disk is geometrically thin with parallel black hole spin and accretion disk spin axes. This assumption, although common, may not be accurate in a significant fraction of observed objects.

Since warped disks may be relatively common, it is important to understand how the disk warp impacts the observed properties of the X-ray emission. Fragile, Miller, and Vandernoot [52] showed that the iron line profiles are sensitive to the tilt and radius of the warp [see also 156]. They argue that the broadened iron line of the AGN MCG–6-30-15 may require a warped disk model. Ingram and Done [73] linked the change in median iron line energy to the frequency of quasi-periodic oscillations (QPOs) if the QPO comes from precession of the inclined hot inner flow.

In this chapter, I present results from modeling the reflected emission in greater detail than before. I assume a lamppost geometry to infer the irradiation of the accretion disk with hard X-rays (rather than assuming a power law emissivity profile). Furthermore, I replace the delta function line emissivity in the plasma frame ($\epsilon \propto \delta(E-6.4\,\mathrm{keV})$) used by Fragile, Miller, and Vandernoot [52] and Wang and Li [156] with the inclination dependent reflection energy spectrum inferred from detailed radiation transport calculations [55]. Invoking simplifying assumptions (i.e. neglecting radiative heating of the emitting plasma), I explore the impact of photons that scatter in the warped disk configuration. I fit the results with the commonly used `relxill_lp` model [56] and show how the warp impacts the inferred black hole disk properties, such as inclination and spin.

The outline of this chapter is as follows. In Section 4.2, I present the simulated energy spectra, including the contribution of photons which scatter multiple times off the disk, and show how the line profiles change as a function of the warp geometry. In Section 4.3 I fit the simulated energy spectra with `relxill_lp`, emphasizing that some of the energy spectra can be fit rather well with a two-component disk model. Finally, in Section 4.4, I summarize the main results.

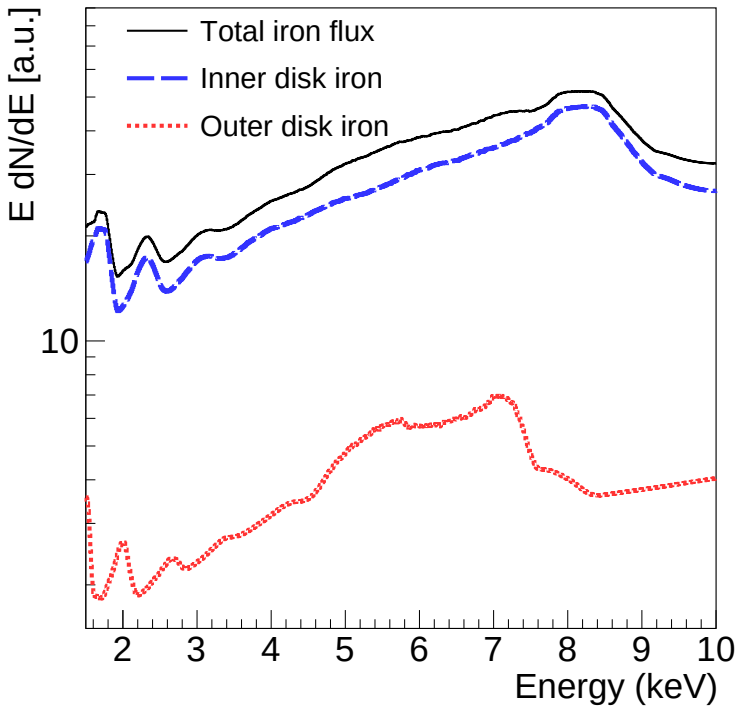

Fig. 4.1: For a simulation with $r_{BP} = 15\,r_g$, $\beta = 15°$ and an observer located at $\phi = 270°$, $\theta = 75°$, the total reflected flux (in black) is broken down into contributions from the photons reflected off the inner disk (blue) or outer disk (red).

4.2 Iron Emission from Warped Disks

In this chapter, I track photon beams originating in the lamppost corona. I vary β, r_{BP}, and h, but for all simulations I use a black hole spin of $a = 0.9$ since the affect of spin on the iron line profile is well studied [see e.g. 136]. The default simulation parameters are $r_{BP} = 15\,r_g$, $\beta = 15°$, and $h = 5\,r_g$; if not otherwise stated, these will be the parameters used. I focus on the reflected emission from AGN, so I use the XILLVER results for a power law index of $\Gamma = 2$, ionization of $\log(\xi) = 1.3$, and iron abundance $A_{Fe} = 1$.

In Figure 4.1 the iron line profile for our standard simulation observed from $\phi = 270°$, $\theta = 75°$ is broken down into the contributions from photon beams which scatter once off either the inner or outer disk. Each contributes a blue and red horn, and so even though the blueshifted peak of the inner disk is the dominant feature, there is an enhancement in the profile at the peak red and blue energies from the outer disk.

4.2.1 Photon beams undergoing multiple scatterings

Previous studies have used backwards ray-tracing codes, which cannot account for photon beams which are incident on the disk multiple times before arriving at the observer. With our forward ray-tracing code, we can track photon beams through an arbitrary number of scattering events before reaching the observer, allowing an investigation of the effect this has on the iron line profile. The question of how to weight photons which scatter multiple times is a difficult one. Consider a beam which scatters twice, for example: at the second scattering the incident flux would not be a pure power law, like XILLVER assumes, but would instead be a combination of the power law and the fluorescence from the first scattering.

To get a rough approximation of the magnitude of multiple scatterings, I do the following: For photons which scatter multiple times, I take the XILLVER spectrum of the first scattering event. Then, I apply the frequency shift of the geodesic from the final scattering event to the the coordinate stationary observer. This profile will obviously not be accurate, but should give us a useful estimate of how much of a correction the inclusion multiple scatterings would be.

In Figure 4.2, I show result from this analysis. There is an approximately order of magnitude drop in flux with each subsequent scattering event. The profiles are mostly similar in shape, although the multiple scatterings show a slight enhancement around 5 keV, likely from scattering off the outer disk since this is the peak of the redshifted energy of the outer disk contribution in Figure 4.1. To investigate this, in Figure 4.3 I show two images of the disk: on the left is the net frequency shifts between emission in the plasma frame and detection in the observer frame for all detected photon beams, and on the right is the apparent surface brightness of the disk, but only from photon beams which scatter multiple times. There is a significant asymmetry in the intensity from the outer disk, with the majority coming from the part of the disk inclined above the equatorial plane. This is likely because photons do not have to bend as much when they travel over the black hole to encounter the inclined outer disk as they would to encounter an unwarped disk in the equatorial plane. This enhanced

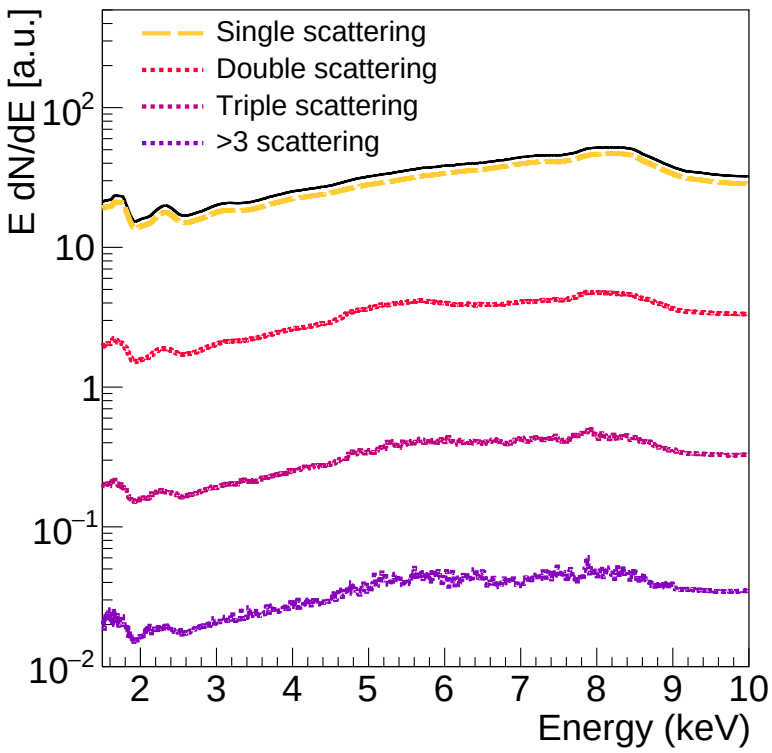

Fig. 4.2: For a simulation with $r_{BP} = 15\,r_g$, $\beta = 15°$ and an observer located at $\phi = 270°$, $\theta = 75°$, the total reflected flux (in black) is broken down based on the number of times the contributing photons scatter.

region of the outer disk is orbiting away from observer, and based on the left hand plot in Figure 4.3 this region has a shift of ∼0.8, which lowers the iron peak to ∼5 keV.

In Figure 4.4, I compare the contributions to flux in the unwarped and warped cases. On the left I plot the fraction of flux between 1.5 and 10 keV from multiply scattered photons in an unwarped disk. At the highest inclination shown (75°), multiple scatterings accounts for about 10 % of the total flux. For a warped disk, shown on the right in Figure 4.4, flux fraction modulates with ϕ (thus with outer disk inclination; see Equation 3.1), and the degree of modulation increases with the inner disk inclination. The contribution increases by almost 5 % at the highest inclination when $\phi = 0°$.

To see how the flux fraction varies with the warped disk geometry, I have plotted the fraction at 75° inclination for simulations with increasing values of r_{BP} and tilt in Figure 4.5. The modulation is proportional to β and inversely proportional to r_{BP}, with the contribution

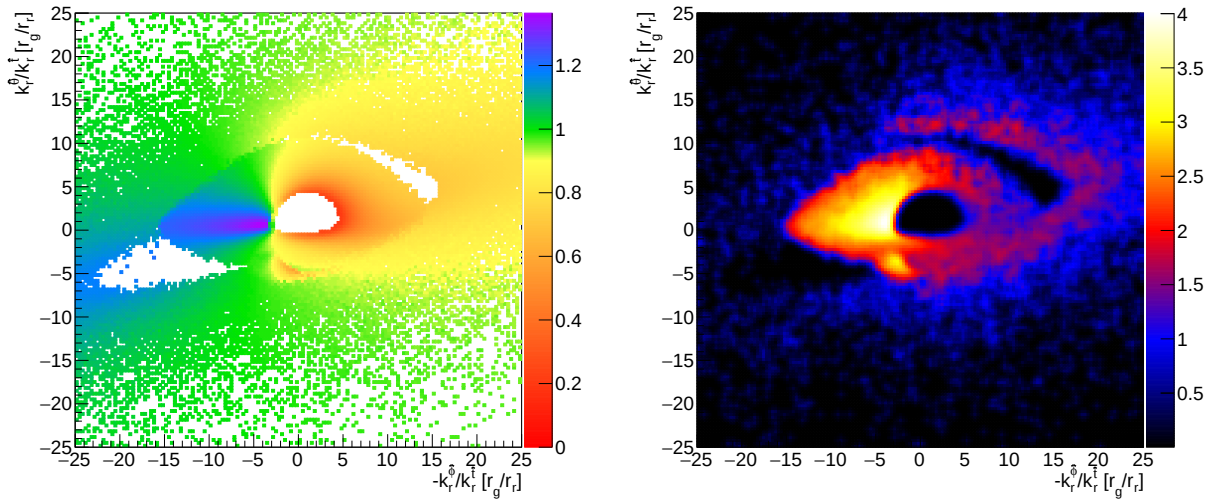

Fig. 4.3: Left: Map of the net frequency shift of photon beams between emission and detection, and Right: intensity map of the reflected emission from two or more scatterings, both as seen by an observer at $10\,000\,r_g$.

increasing to $\sim$18 % for $r_{BP} = 8\,r_g$, almost twice the value for an unwarped disk. Though the specifics of these results are based on a rough estimation, clearly disk warping increases the importance of multiple scattering photons, especially when the disk tilt is large and warp radius is small. A future effort to integrating the recent XILLVERRR results [162], which calculates the reflection spectra of radiation returning to the disk (i.e. two scatterings), will allow for a more accurate treatment of the reflection spectra of warped accretion disks.

4.2.2 Shadowing of the Outer Disk

In Figure 4.6 I show g-maps of four observers around a black hole with the inner disk fixed at a 45° inclination. The figure shows that the inner disk shadows the lamppost emission reaching the inner edge of the outer disk that lies below the inner disk (i.e. on the right in the $\phi = 90°$ g-map).

This is even more apparent when the degree of tilt is larger; in Figure 4.7, I show the g-map for a tilt of 20°. Almost the entire blueshifted portion of the outer disk is shadowed. This

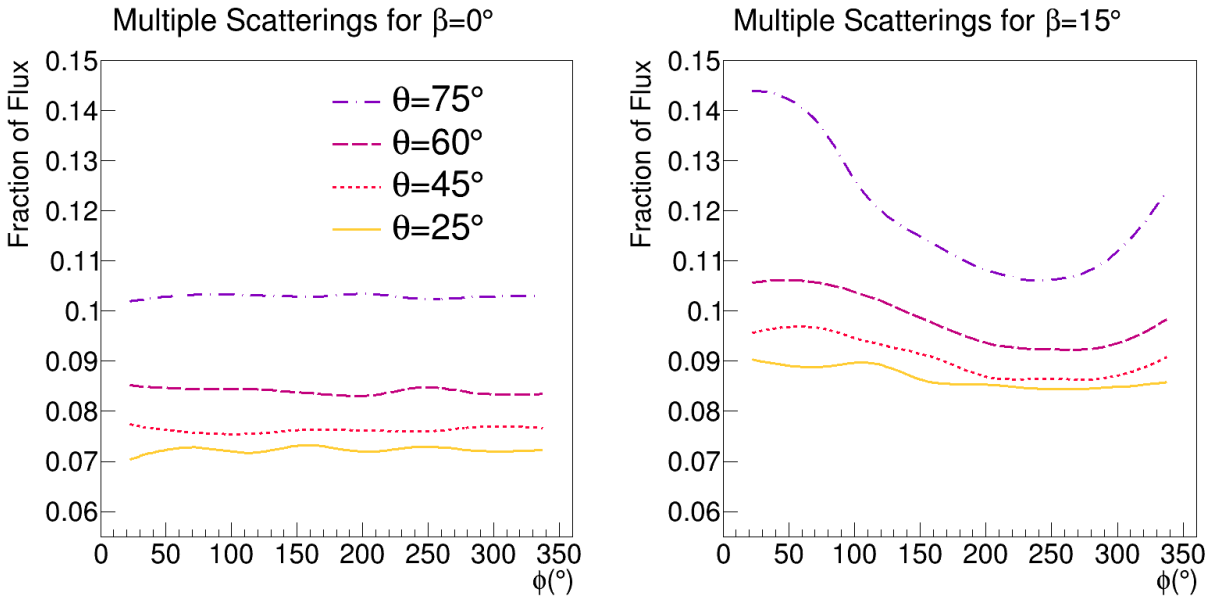

Fig. 4.4: Left: The contributions of multiply scattered photons to the flux for an unwarped disk and Right: the contributions for a warped disk with a 15° tilt, both as a function of the observer's inclination.

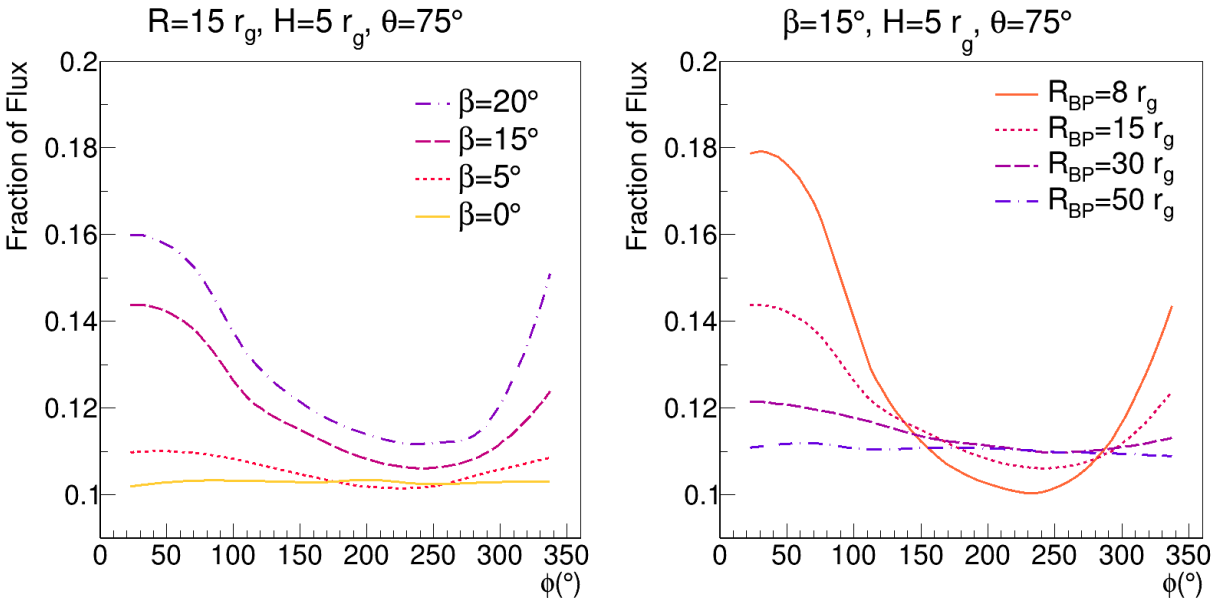

Fig. 4.5: Left: The fraction of flux contributed by photons scattering multiple times for several values of disk warp, and Right: for several values of r_{BP}.

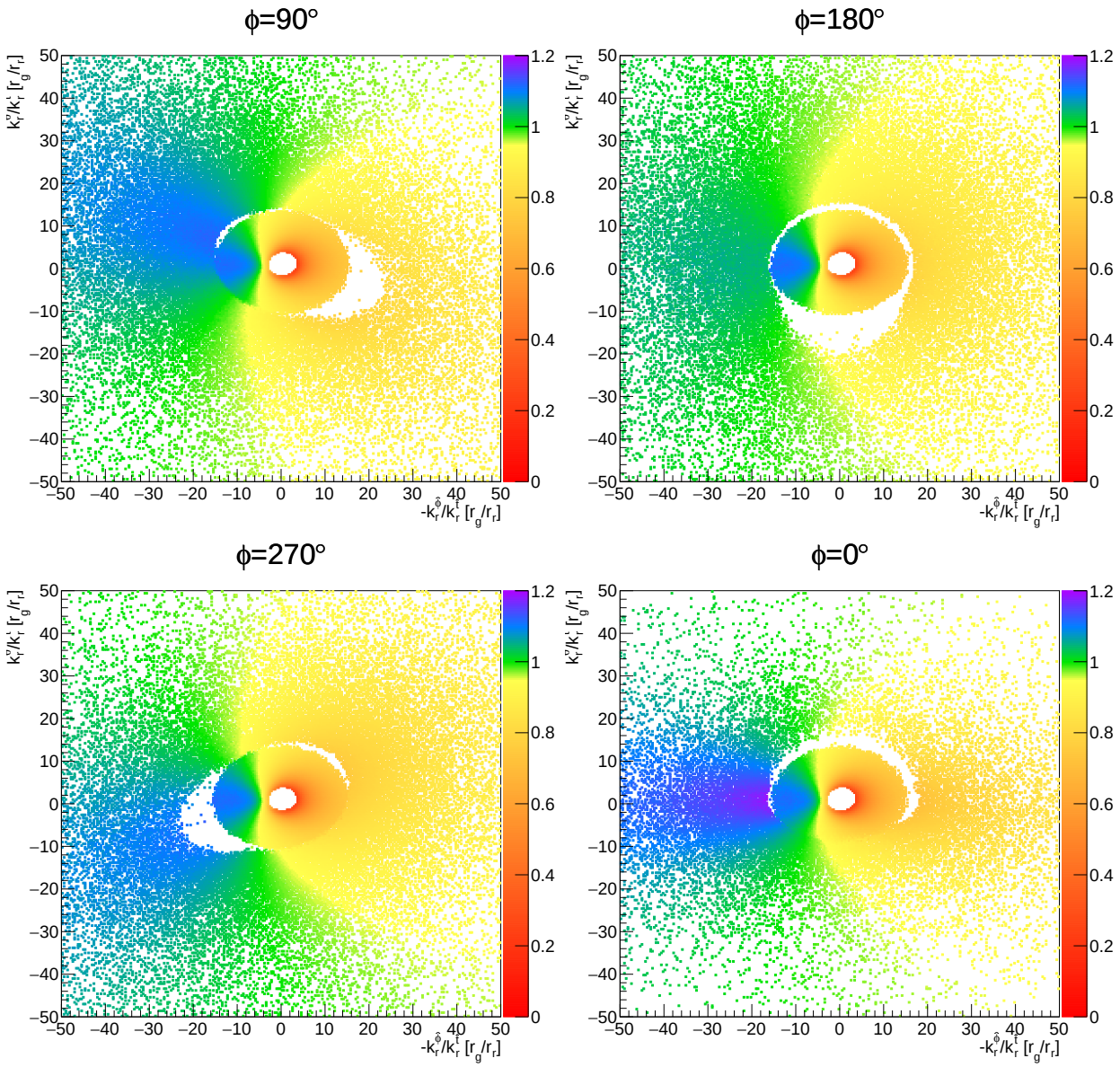

Fig. 4.6: Maps of the frequency shift factor between emission and observation for our default configuration. The inclination of the inner disk is fixed at 45°, and the azimuth moves around the disk. At $\phi = 180°$, the outer disk is inclined at 60°, and at $\phi = 0°$ it is inclined at 30°.

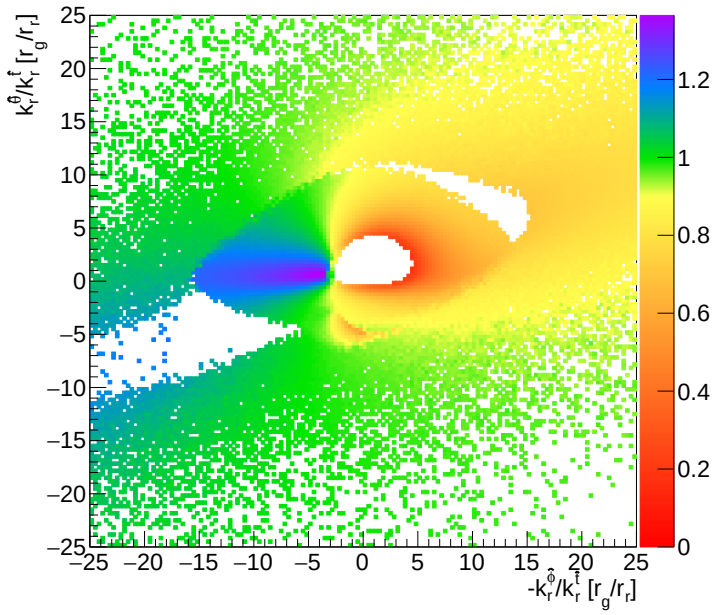

Fig. 4.7: Map of the frequency shifts between emission and detection for an observer located at $\theta = 75°$, $\phi = 270°$. The disk has tilt of 20°, r_{BP} of 15 r_g, and lamppost height of 5 r_g.

should affect the iron line profile from the outer disk, as the red or blueshifted portion will be suppressed, depending on which region of the disk is shadowed.

4.2.3 The Line Profile from Warped Disks

In Figure 4.8, I look at the iron line profiles for observers at four inclinations between $\theta = 25°$ and $\theta = 75°$ at azimuths all around the system. For the small r_{BP} value used here, the reflection off the outer disk contributes significantly to the shape of the profile.

The tendency of a warped disk seems to be to smear out the iron line further, though if the inclinations are different enough two peaks may be visible. This tends to occur around $\phi = 180°$, where the outer disk is seen with its lowest inclination relative to the inner disk, and thus the blue horn contributed to the line profile is at its lowest energy. This is most obvious in the 60° inclination plot (lower left) of Figure 4.8. The contribution from the inner disk is peaked around 7.5 keV. Around $\phi = 0°$, the outer disk is inclined at about

75°, so contributes less flux at higher energies. As the azimuth approaches 180°, the outer disk inclination approaches 45° and the blue horn shifts down in energy to just below 7 keV, becoming clearly separate from the inner disk contribution. Though in our simulated data these two peaks are also distinct in the bottom right plot of 75° inclination, the higher inclination means that both peaks are already smeared and are thus less sharply separated. Returning to the 60° inclination plot, one might expect the profiles of $\phi = 90°$ and $\phi = 270°$, to be identical: their outer disks have the same inclination and are simply rotated with respect to the inner disk. The profiles, though, show that the blueshifted contribution from the outer disk is less prominent at $\phi = 270°$ – the region of the outer disk orbiting away from the observer is elevated above the inner disk and thus is irradiated more by the lamppost, while the blue region is irradiated less as well as shadowed.

Next, I examine the ways that changing properties of the disk misalignment affects the reflected spectrum. In Figure 4.9, I show the profile for four values of r_{BP}, between 8 and 50 r_g, for several different observers. The chosen viewing angles exhibit the most salient features seen in all the simulations. I vary the warp radius while holding the tilt and lamppost height constant at 15° and 5 r_g, respectively.

The azimuth from which the system is viewed has a strong effect on the reflected spectrum. At 60° inclination and 45° azimuth (top left), where the inclination of the outer disk is approximately equal to the inclination of the inner disk (61.12°), the profile is largely unchanged, aside from some minor differences in the shape of the peak.

When the outer disk has a lower inclination than the inner disk, as in the top right at 60° inclination and 180° azimuth ($i_{out} = 45°$), the two visible peaks from the inner and outer disk trade prominence as the warp radius extends. Thinking about r_{BP} as the 'ISCO' of the outer disk, as r_{BP} extends further out this emission peaks at lower and lower energies and contributes less to the total reflected flux. This causes the energy of the peak flux to shift from being contributed by the outer disk to the inner disk, while in the middle they are relatively equal. This trend is also seen in the bottom left at 75° inclination and 135°

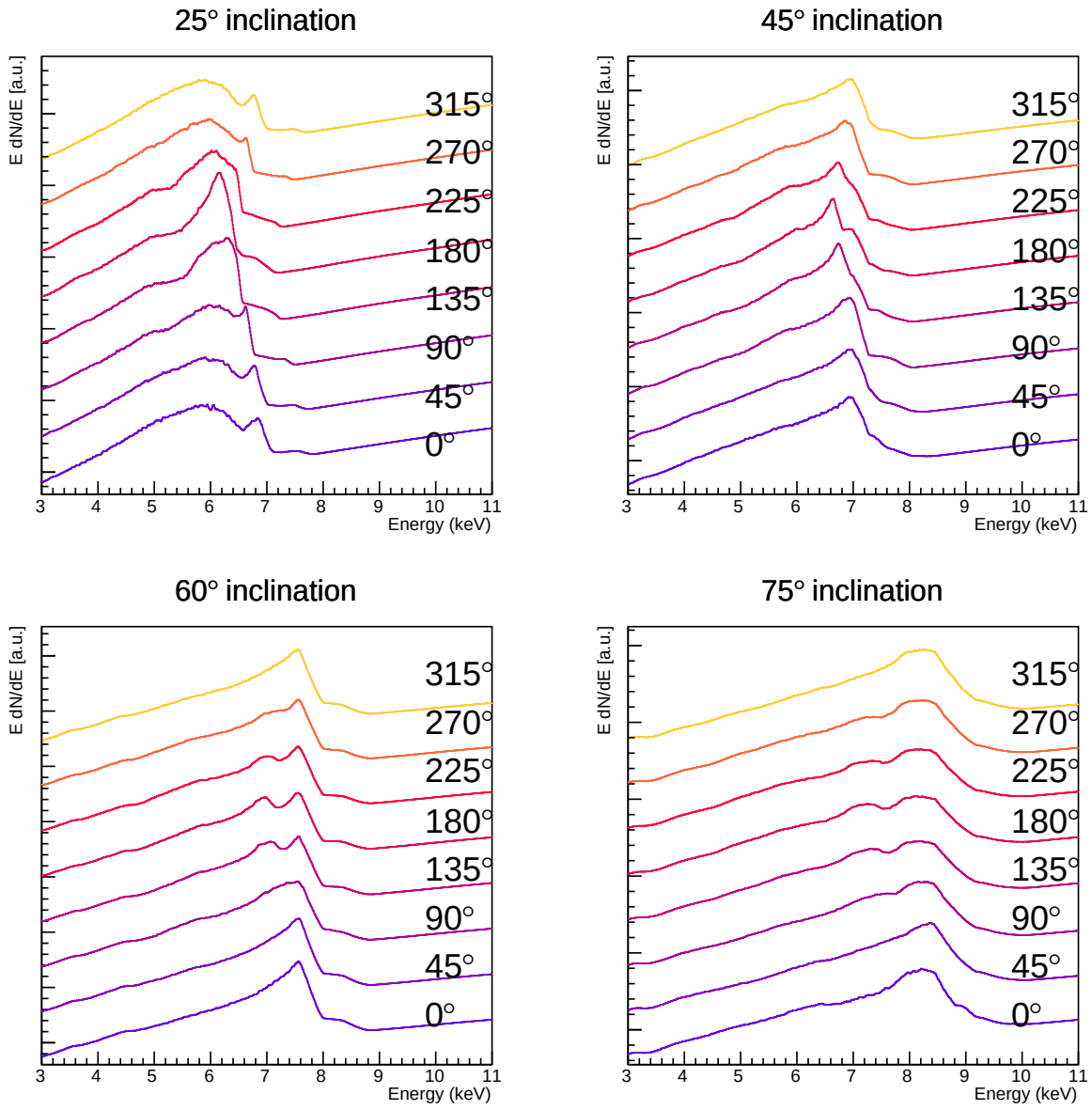

Fig. 4.8: Line profiles for observers at different azimuth angles, including the four shown in Figure 4.6. The profiles are normalized to the same energy flux above 6.4 keV and have been offset from one another for clarity. Each profile is labeled with azimuth angle on the right hand side.

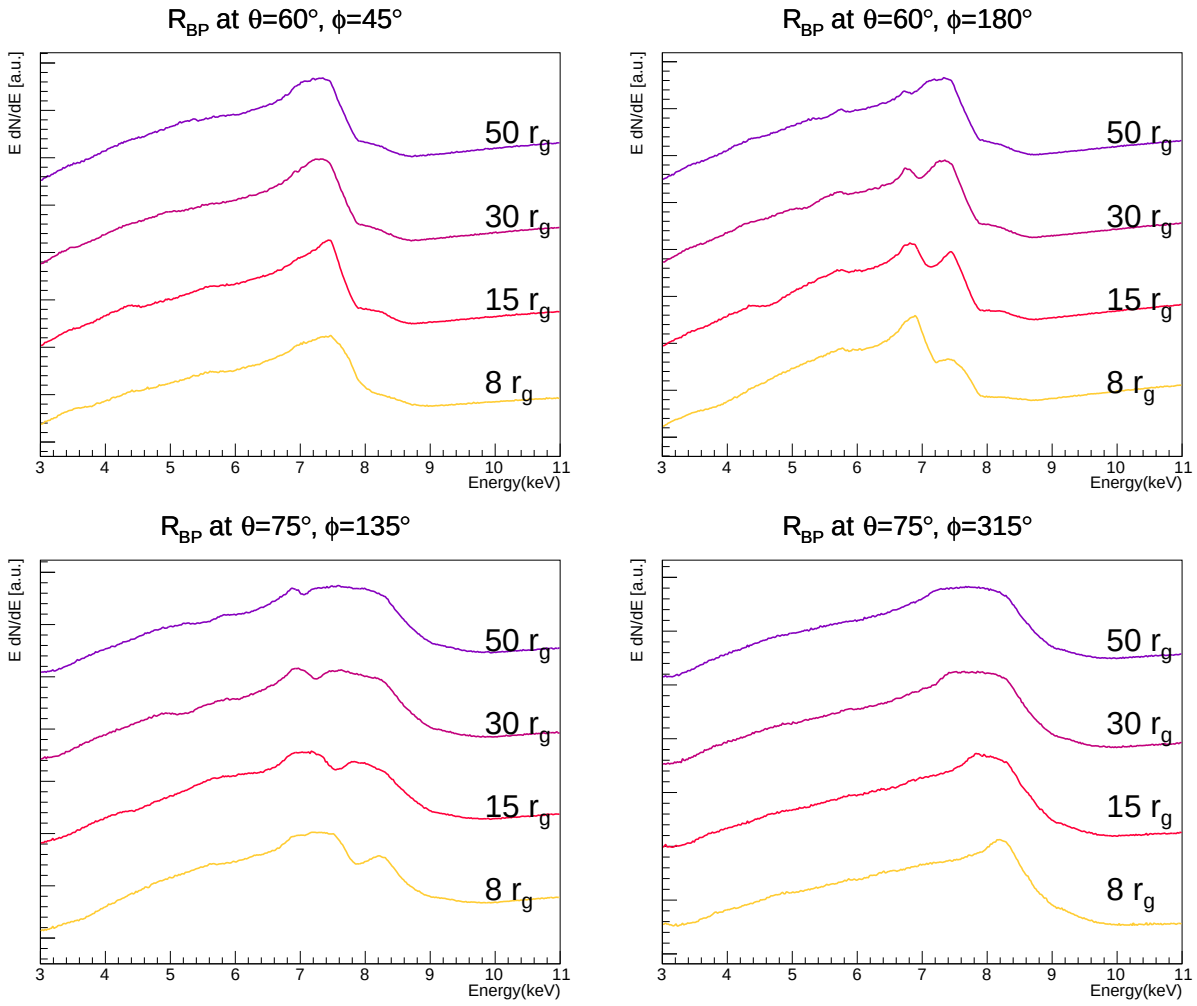

Fig. 4.9: Line profiles for four different values of r_{BP}, with $a = 0.9$, $\beta = 15°$, and $h = 5\,r_g$. On the right, each profile is labeled with the radius of the warp r_{BP}, between 8 and $50\,r_g$.

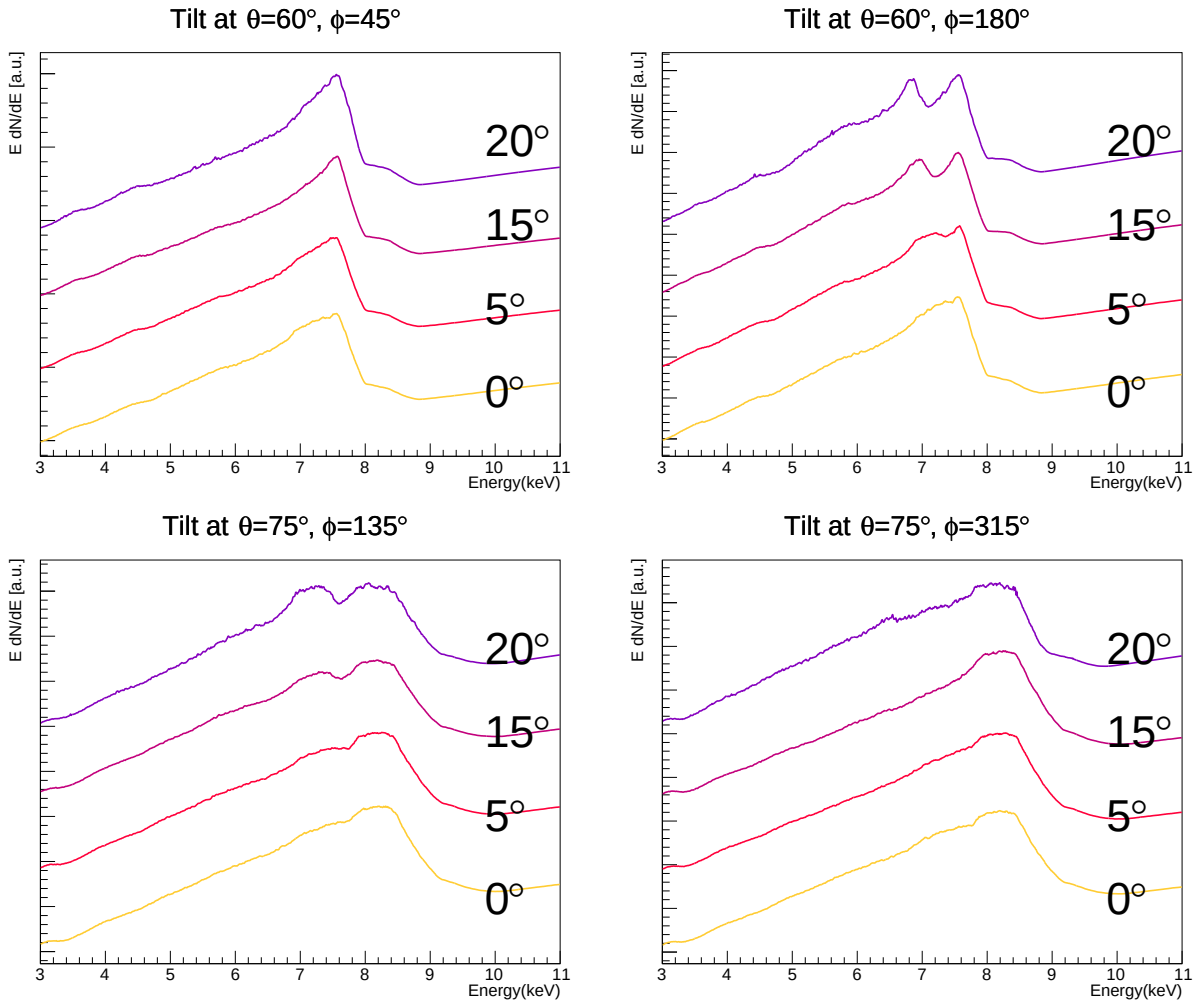

Fig. 4.10: Line profiles for four different values of β, with $a = 0.9$, $r_{BP} = 15\,r_g$, and $h = 5\,r_g$. On the right, each profile is labeled with the tilt angle, between 0 and 20°.

azimuth, where the outer disk similarly has a lower inclination ($i_{out} = 64.7°$).

In the bottom right plot, the inner disk inclination is 75°, the azimuth is 315°, and the outer disk is nearly edge on at $i_{out} = 85.8°$. Here there are apparently not two peaks; instead, as the inner edge of the outer disk r_{BP} gets larger, this emission from the outer disk moves to lower energies, causing the peak to smear out. The the falling edge of the Fe Kα peak remains in the same place, the plateau of maximum flux extends, apparently pushing the energy of the peak lower; this further broadening of the iron line may cause an overestimating of the spin of the black hole.

Figure 4.10 shows the profile for different values of the disk tilt seen by the same observers as

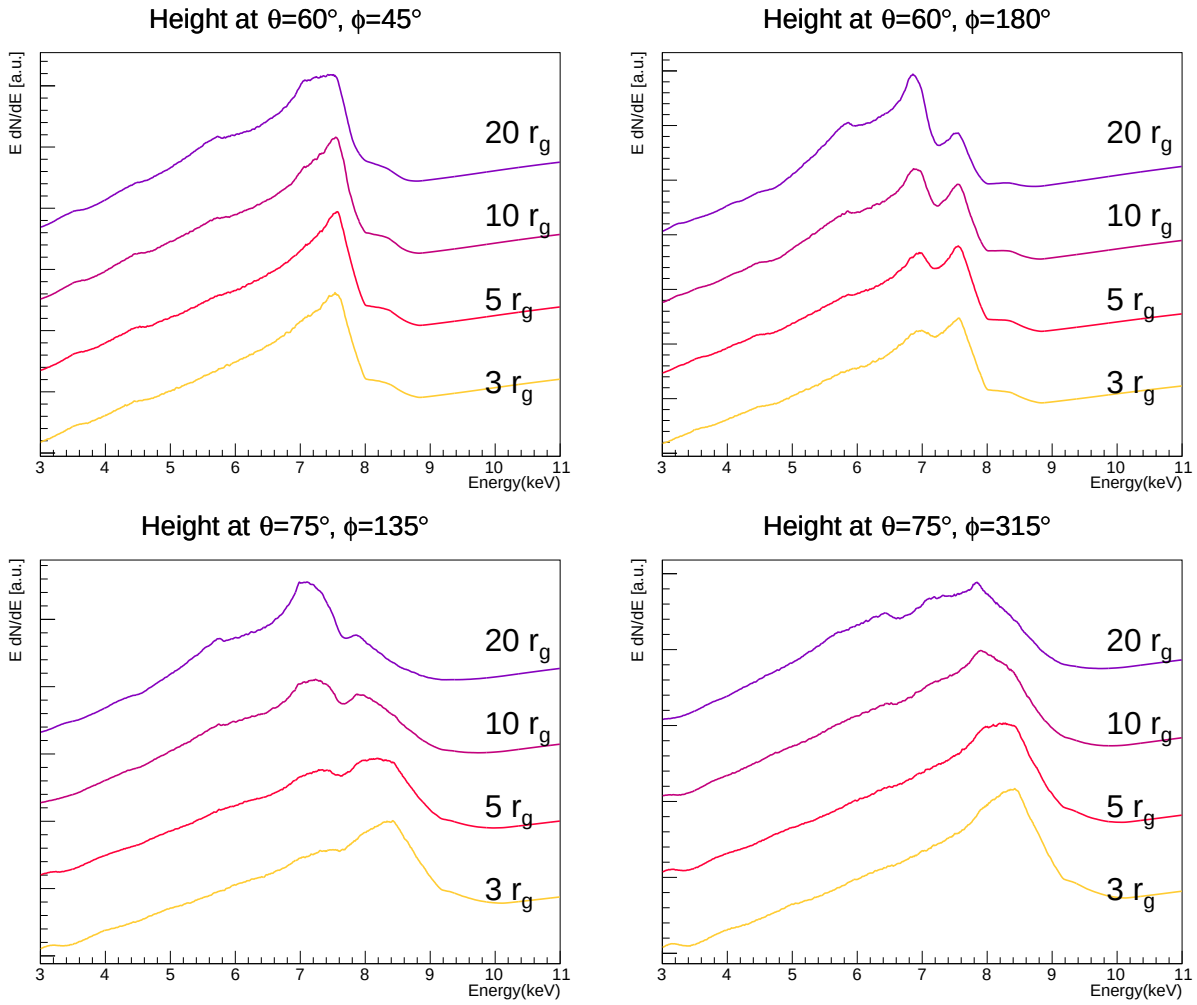

Fig. 4.11: Line profiles for four different values of lamppost height, with $a = 0.9$, $r_{BP} = 15\,r_g$, and $\beta = 15°$. On the right, each profile is labeled with the height, between 3 and $20\,r_g$.

in Figure 4.9. In the top right and bottom left, where the outer disk has a lower inclination than the inner disk, increasing the disk tilt has the effect of shifting the blue horn of the outer disk to the left, as higher tilt further lowers the inclination of the outer disk. In the other two plots, the increasing tilt serves to shift the outer disk emission towards higher energies, though it is already obscured by the peak from the inner disk.

Figure 4.11 shows how the profile changes with lamppost height. The taller the lamppost is, the larger the break radius of the emissivity, and the more prominent the contribution of the outer disk to the profile. This is very clear in the top right plot, where at $H = 20\,r_g$ the entire profile from the outer disk is clearly separated from the blue horn of the inner disk

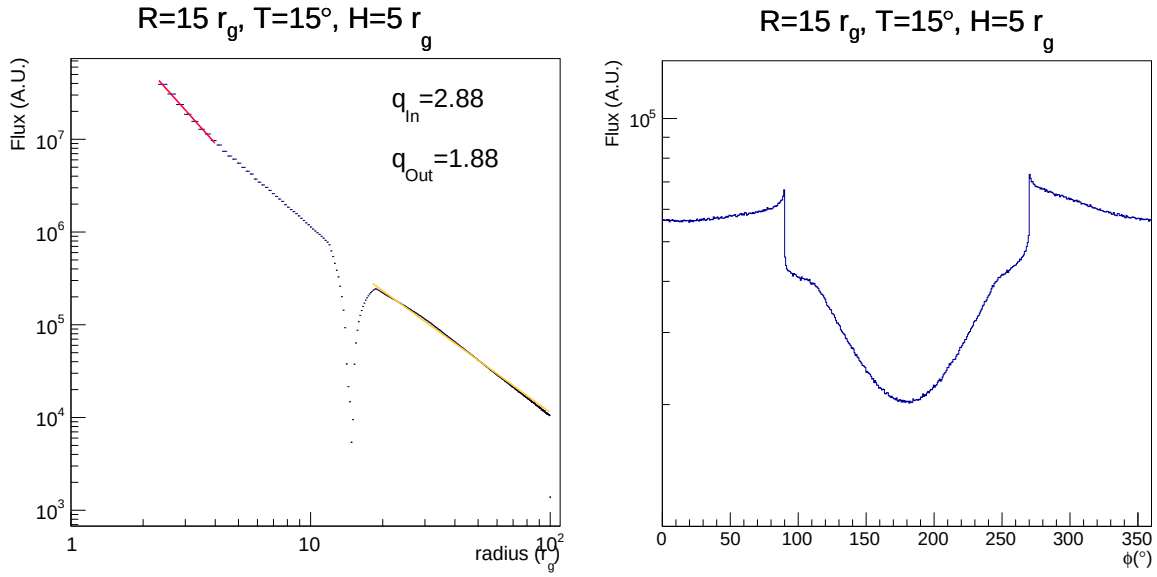

Fig. 4.12: Left: Radially dependent emissivity profile, showing the index for the inner and outer disks. Right: ϕ-dependent profile for the outer disk ($15\,\mathrm{r_g} < r < 100\,\mathrm{r_g}$), highlighting the asymmetry caused by the lamppost being off-axis as well as shadowing by the inner disk.

contribution.

4.2.4 Emissivity profile

Figure 4.12 shows the emissivity profile (i.e. the energy flux ε of photons with an energy exceeding the energy threshold for iron line emission) for the entire disk, as well as the ϕ-dependent profile for just the outer disk (in this case, $\mathrm{r_{BP}} > 15\,\mathrm{r_g}$).

There is a dip in the profile at $\mathrm{r_{BP}}$, so for fitting the break in emissivity, I fit q_{in} inside $r = h$ or $\mathrm{r_{BP}}$, whichever is smaller, (from $\varepsilon \propto r^{-q_{in}}$) and q_{out} outside $\mathrm{r_{BP}}$ or h, whichever is larger. For all simulated models, the results are collected in Table 4.1.

4.3 Fitting of Simulated Iron Profiles

To determine how disk warping effects the spin measurement of a black hole, I have imported our profiles into XSPEC [6] and used them to generate simulated energy spectra. To make our profiles compatible for fitting with `relxill`, I only use the profiles from photon beams

$r_{BP}(r_g)$	$\beta(^\circ)$	$h(r_g)$	q_{In}	q_{Out}
		Default model		
15	15	5	2.88	1.88
		Varying transition radius		
8			2.92	2.00
30	15	5	2.86	1.88
50			2.86	1.90
		Varying tilt		
	0		2.86	1.98
15	5	5	2.87	1.99
	20		2.89	1.83
		Varying lamppost height		
		3	2.74	1.83
15	15	10	1.76	1.92
		20	1.21	1.75

Tab. 4.1: Emissivity indices for inner and outer disks. I show results for our default parameter values, and group the remaining results into three groups for the varied parameter: transition radius r_{BP}, tilt β, and lamppost height h.

which scatter a single time. Subsequently I fit them with the lamppost source version of `relxill`, called `relxill_lp` [56]. For faking our simulation results as data in XSPEC, I use the Cycle 22 sample response files for the HETG instrument on *Chandra* and bin the spectra with a resolution of 10 eV. This resolution is similar to that of the microcalorimeters on the upcoming *XRISM* [164] and *Athena* [115] missions and I expect these results will prove more useful once these two large effective area missions are in operation. For our `relxill_lp` model, I fix the inner and outer radius of the disk to the ISCO and $100\,r_g$, respectively; the cutoff energy to 300 keV; the reflected fraction to -1 (so our model does not include any of the direct emission from the lamppost); and the redshift of the source to 0. I freely fit spin, inclination, lamppost height, power law index, the ionization, and the iron abundance, with each initially set to their simulated value.

To verify that our code broadens the reflected energy spectra from XILLVER in a manner

compatible with `relxill`, I first fit our results for a flat, unwarped disk. I fit four inclinations, $\theta = 25°$, 45°, 60°, and 75°, and eight azimuths, $\phi = 0°$, 45°, 90°, 135°, 180°, 225°, 270°, and 315°. Figure 4.13 shows the collected results of these fits, with one panel for each inclination. In general, the results are accurate, though not always within the 90 % errors. The inclination specifically is under or overestimated, though not by more than a degree. Similarly, the spin can be under or overestimated, though it is still fit as highly spinning.

I next fit our default warped disk model. The plots of the results from these fits, including 90 % confidence error bars, are in Figure 4.14. The goodness of the fit depends on ϕ, with the best fit occurring around $\phi = 90°$ and/or 270°, where the outer and inner disk inclinations are closest to matching. For these azimuths at $\theta = 25°$, h, Γ, $\log(\xi)$, and A_{Fe} are all fit close to their true values. The spin is consistently fit too low, though it is still fit with high spin ($\sim$0.75 – 0.85). This underestimation is greater than I found for the aligned disk, which was only lower than the true value by $\sim$0.05. At azimuths near $\phi = 0°$, where the outer disk is more highly inclined than the inner disk, the reduced χ^2 tends to be reasonably good, but the fit values poorly match the simulated values; this is particularly true at $\theta = 25°$, where the height is half its true value and inclination is off by 15°.

In the case of the 45° inclination results in Figure 4.14, all parameters except the lamppost height are fit rather well for the azimuths with good fits ($\sim$270 – 90°). For 60° inclination the best fit appears to be around $\phi = 270°$. Here, once again, the inclination, power law index, disk ionization, and iron abundance are fit very close to their true values, while the lamppost height and spin parameter are slightly off. For 75°, the $\phi = 270°$ is among the azimuths with the lowest χ^2, though the best fit is actually at 315°. As predicted from the spectra in Figure 4.9, the spin is consistently overestimated because the profile has been broadened by the contribution of the outer disk.

The overall result seems to be that there is difficulty finding a good fit for out data with `relxill_lp` when the angular momenta axes of the two disks appear aligned to the observer (at $\phi = 0°$ and $\phi = 180°$), likely because these viewing angles are where the tilt manifests

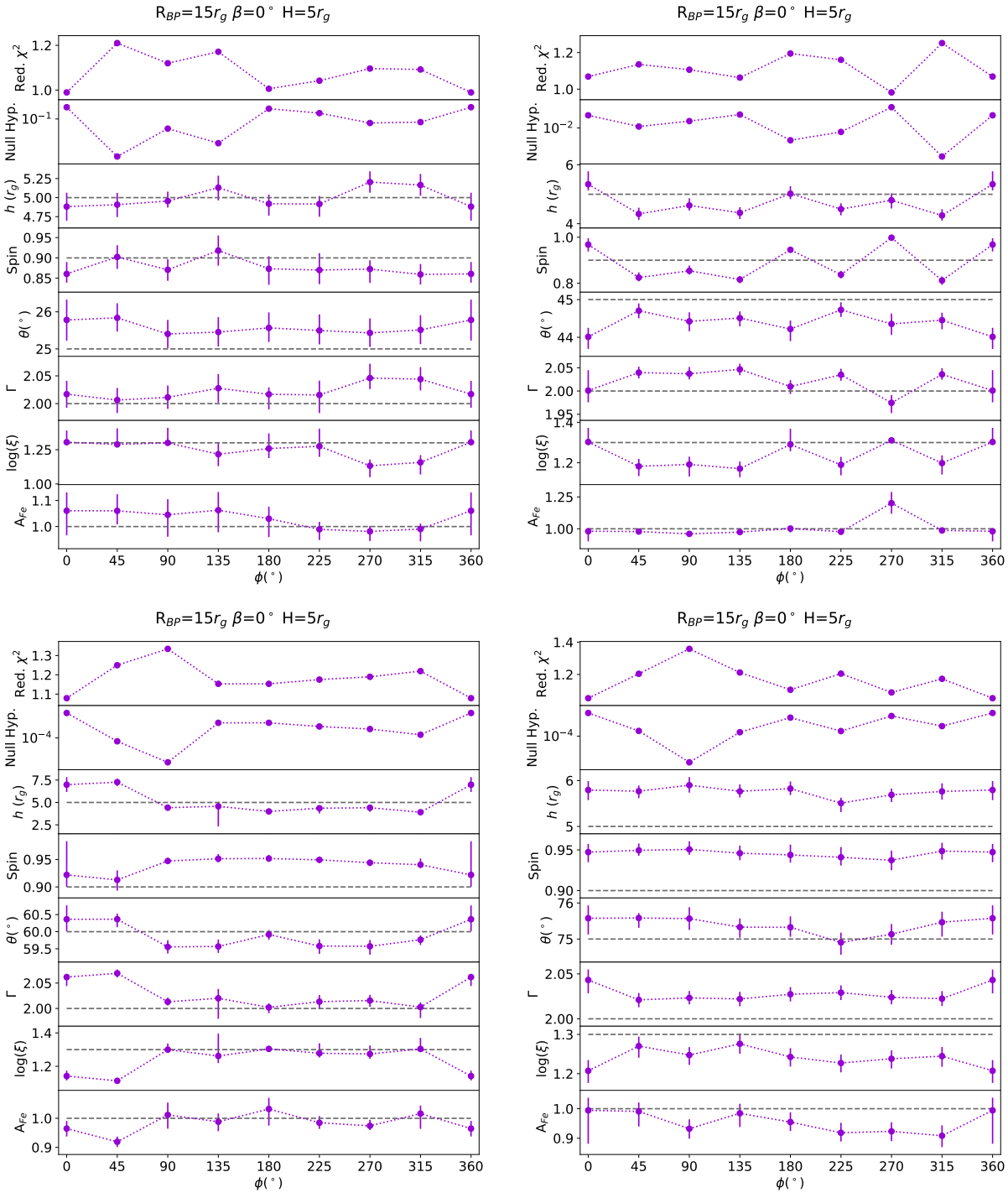

Fig. 4.13: For an unwarped disk, the XSPEC results obtained with `relxill_lp` for all ϕ values. In purple are the fit values with 90 % confidence error bars; the points are connected by a dotted line for clarity. The dashed grey lines show the simulated parameter values.

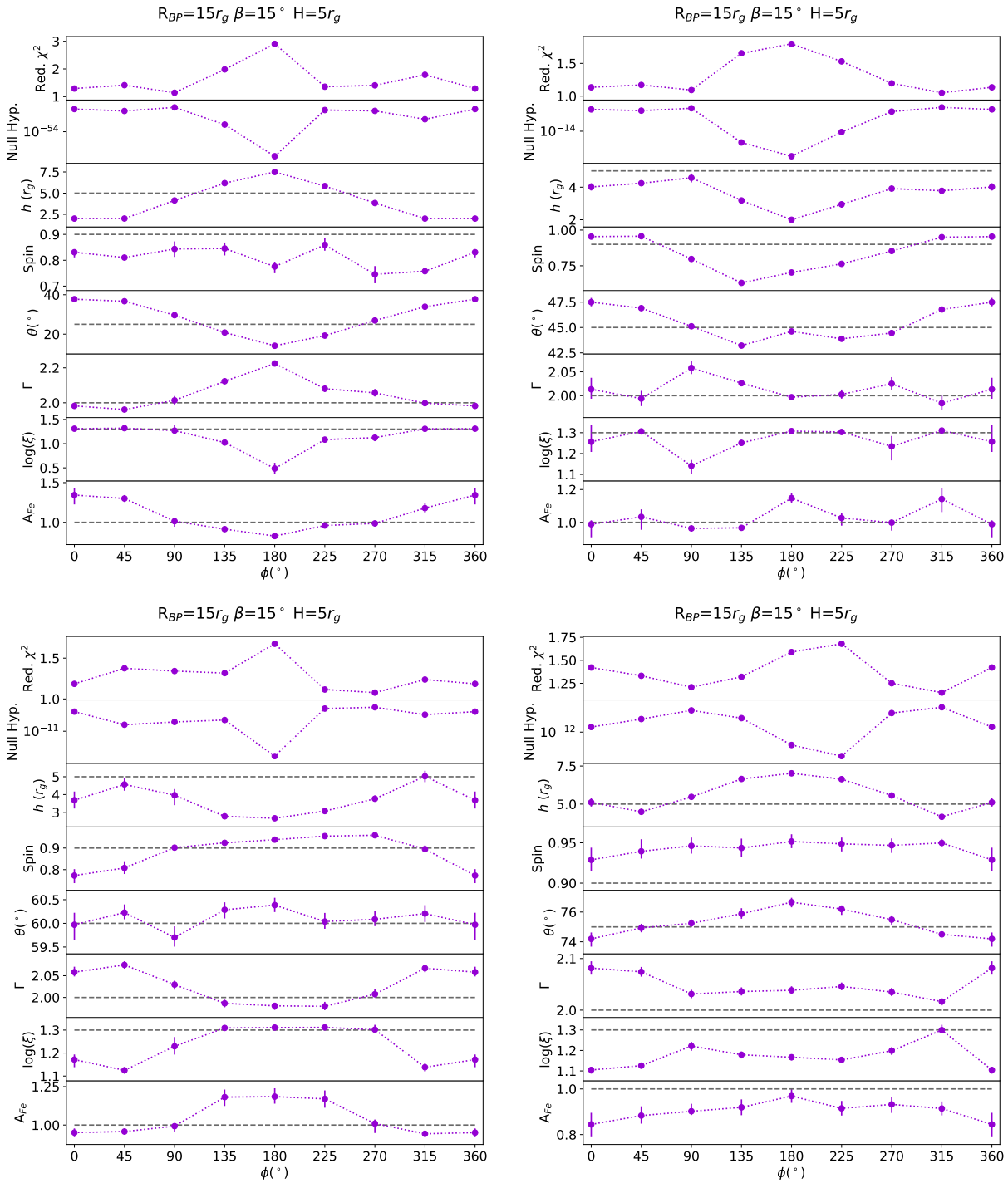

Fig. 4.14: For an warped disk with tilt $\beta = 15°$, I show the XSPEC results obtained with `relxill_lp` for all ϕ values. The formatting is the same as in Figure 4.13. Note: for $\phi = 180°$ at 45° inclination (the middle point in the top right plot), XSPEC was unable to calculate errors with all of these parameters varying freely. I instead froze the lamppost height at $2\,r_g$, its best fit value, and thus there are no error bars on this point.

Parameter	Simulated Value	Fit Value
Reduced χ^2	—	1.414
Null hypothesis	—	2.13×10^{-10}
Lamppost height (r_g)	5	$2.006^{+0.145}_{-0.0}$
Spin	0.9	0.811 ± 0.004
Inclination(°)	25	$36.694^{+0.241}_{-0.227}$
PL Index	2.0	1.961 ± 0.004
$\log(\xi)$	1.3	1.320 ± 0.002
A_{Fe}	1.0	1.300 ± 0.043

Tab. 4.2: Results of the fit for a warped disk with a single `relxill_lp` model.

to the observer entirely as difference in inclination. For other azimuths, where the difference between the inclinations of the disks is smaller (i.e. close to $\phi = 90°$ or 270°), there can be a reasonable fit with parameters close to their true value, especially at higher inclinations. Next, I explore the possibility of fitting our data with a two-component `relxill_lp` disk and see if it yields better results.

4.3.1 Fitting with a Two-Component Disk

An obvious choice to improve the fitting of a warped accretion disk is to use a two-component `relxill` model. For an illustrative example, let us examine the XSPEC fit for 25° inclination from 45° azimuth, shown on the left in Figure 4.15. The data shows a spur at 6.4 keV, which a single `relxill_lp` model is unable to account for. From this fit, I get the values displayed in Table 4.2. In particular, the fit values for inclination and lamppost height are significantly off.

I find that a two-component `relxill_lp` gives higher-accuracy estimates of the simulated system parameters than a one-component fit. I perform the two-component fit by adding two `relxill_lp` models in XSPEC. I tie the spin, lamppost height, and power law index for the two `relxill_lp` models together. Furthermore, I tie the outer radius of the first

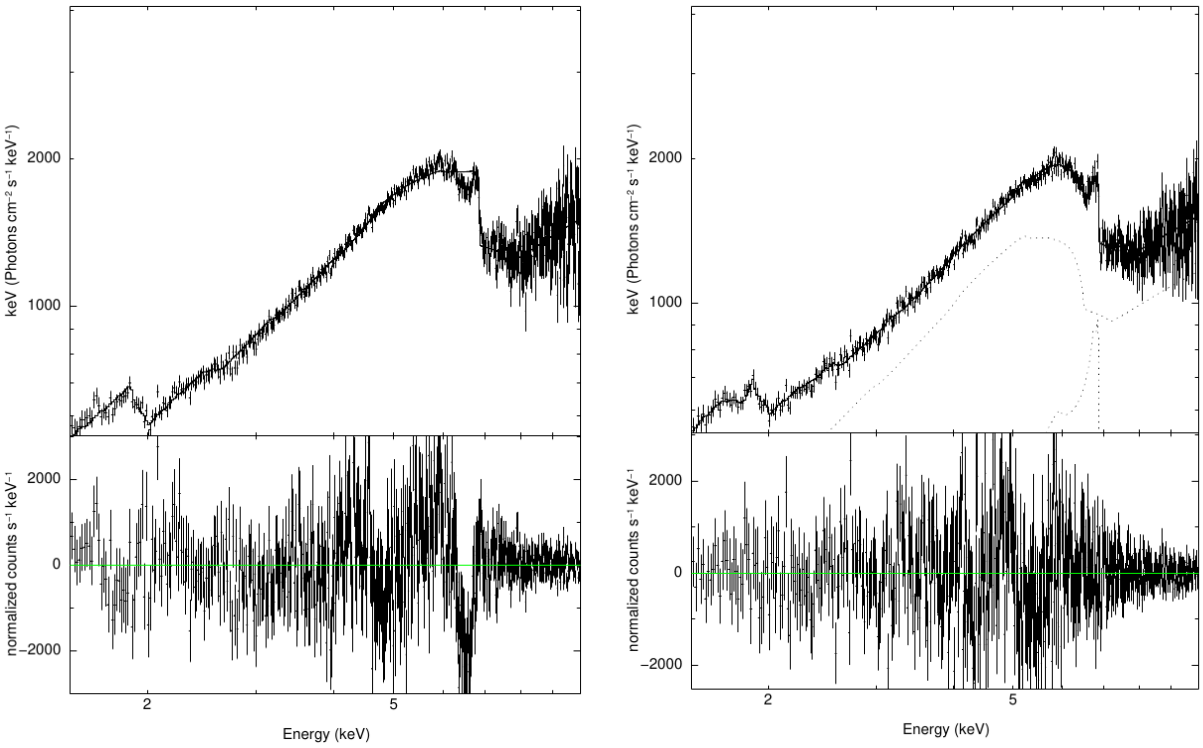

Fig. 4.15: Left: XSPEC fit with a single `relxill_lp` disk model with 25° inclination and ϕ = 45°. Right: For the same simulated profile, the fit with a double `relxill_lp` model.

`relxill_lp` model to the inner radius of the second model. For the inclination of the outer disk, I tie it to inner disk inclination with Equation 3.1, using the simulated values of the tilt β and observer azimuth ϕ. Note that these angles would not be known for actual systems. I do not fix the outer disk ionization and iron abundance to the inner disk values; I expect that the asymmetric illumination due to the lamppost being offset from the outer disk angular momentum and shadowing by the inner disk may cause these values to be poorly fit. Thus, the values that I am fitting for the two component model are: lamppost height, black hole spin, θ, r_{BP}, Γ, inner $\log(\xi)$, inner A_{Fe}, outer $\log(\xi)$, and outer A_{Fe}.

The right plot in Figure 4.15 shows the result of the two-component fit, which has much better residuals. The fit values are collected in Table 4.3, and should be compared to the results from the one-component fit in Table 4.2. The lamppost height and inclination results are much closer to the simulated results than in the case of the one-component fit. A possible explanation for the too-small lamppost height is that the tilted geometry results in

Parameter	Simulated Value	Fit Value
Reduced χ^2	—	1.037
Null hypothesis	—	2.64×10^{-1}
Lamppost height (r_g)	5	$4.061^{+0.345}_{-0.988}$
Spin	0.9	$0.790^{+0.023}_{-0.022}$
Inclination(°)	25	$24.294^{+0.519}_{-0.610}$
PL Index	2.0	$2.051^{+0.023}_{-0.024}$
Inner log(ξ)	1.3	$1.083^{+0.104}_{-0.054}$
Inner A_{Fe}	1.0	$0.949^{+0.276}_{-0.068}$
r_{BP} (r_g)	15	$16.294^{+3.010}_{-1.160}$
Outer log(ξ)	1.3	$1.299^{+0.020}_{-0.196}$
Outer A_{Fe}	1.0	$1.014^{+0.791}_{-0.259}$

Tab. 4.3: Results of the fit for a warped disk with a double `relxill_lp` model, showing the simulated value and the fit value where $i_{\rm out}$ is constrained by the simulated values of β and ϕ.

the corona being closer to the elevated side of the outer disk than in a the case of a fully aligned flat disk. The spin is fit with roughly the same value as the single disk model, still slightly lower than the simulated value. Also noteworth is that the fit recovers the location of the transition radius r_{BP}. In terms of disk composition, the iron abundance was slightly overestimated by the single `relxill_lp` model but is accurate for both the inner and outer disks in the double `relxill_lp` model. The ionization, though, was accurate in the single `relxill_lp` model, but the double model accurately fits the outer ionization while slightly underestimating the ionization of the inner disk.

When I remove the constraint on ϕ and β based on the simulated value, I find that across all azimuths the fit recovers the simulated values with about the same accuracy as with the constraint. The outer disk inclination, though, can be off by as much as 20° at $\phi = 180°$, and so I leave the constraint on ϕ and β for the remaining fits.

I have fit the simulated data for all azimuths with the double `relxill` model and plot the

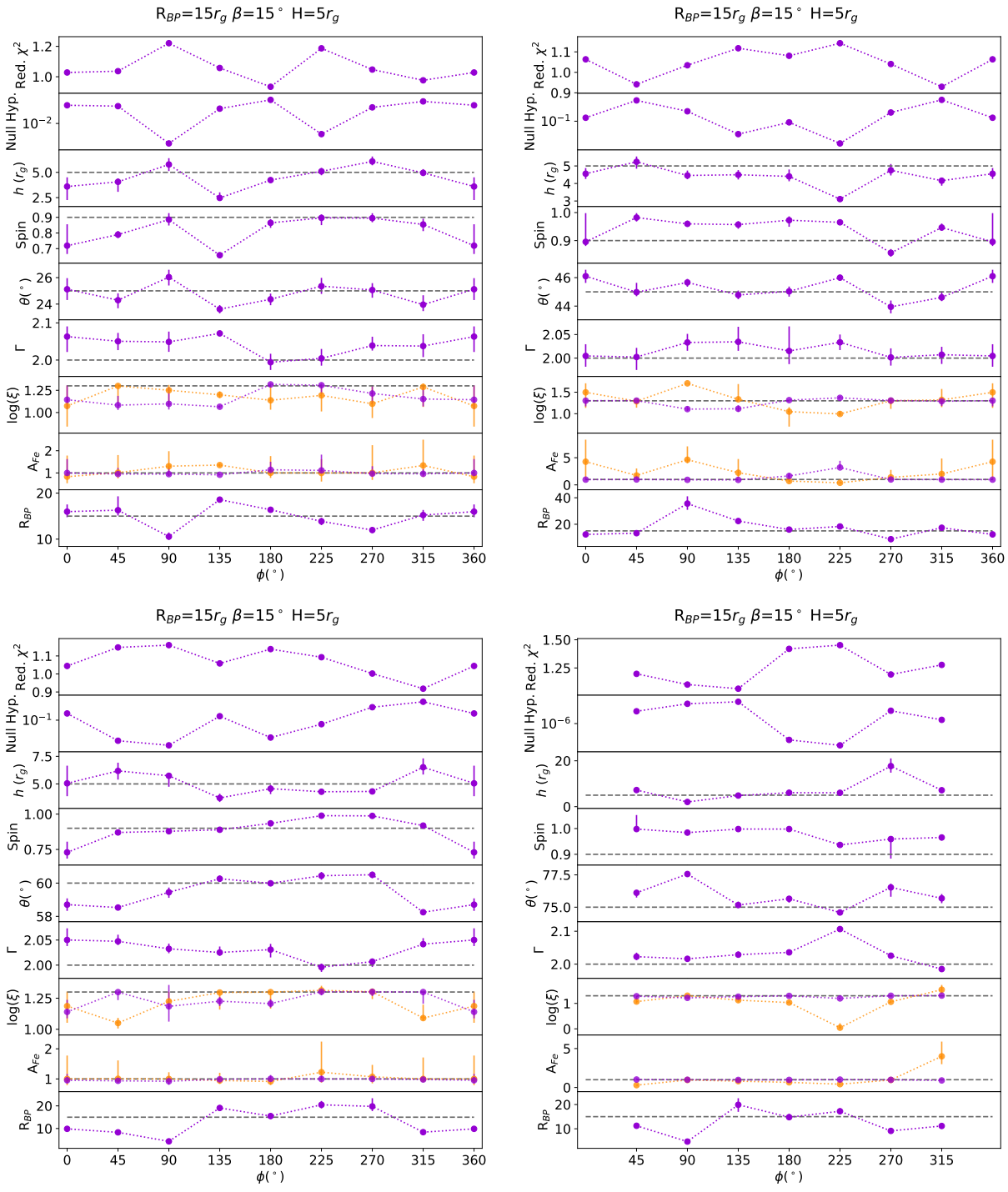

Fig. 4.16: Results of fitting our simulated data with a double `relxill_lp` model in XSPEC. For log(ξ) and A$_{Fe}$, the purple points indicates the inner disk result and the orange indicates the outer disk. I do not fit $\phi = 0°$ at 75° inclination (the bottom right plot) because the outer disk is viewed exactly edge on at 90°, and the `relxill_lp` model is only valid up to 87°.

results in Figure 4.16. The general trend continues that the two-component model fits the simulated data much better than the one-component model, specifically with regards to the lamppost height and inclination, though the spin is still underestimated for some azimuths.

4.4 Conclusions

In this chapter, I have shown the effect that disk warping has on the profile of the fluorescent iron line from black hole accretion disks. Though I have focused on AGN, our method is valid for binary black holes as well.

I have estimated the impact of multiple scatterings, finding that their contribution to the iron line flux is stronger for warped disks than unwarped disks. This contribution does not appear by eye to fundamentally change the profile of the fluorescent iron line, but due to the complexities of ray-tracing and fluorescence in the disk, more work is still required to determine the exact effect this has on the fitting of spin and inclination.

I find that the inclination and spin of a warped disk can be poorly fit using a standard single disk `relxill`, especially for viewing angles near $\phi = 0°$ and $\phi = 180°$ where the warp manifests to the observer entirely as difference in inclination between the two disks. This can lead to an under or overestimation of the spin and inclination by tens of percent, especially for systems with low inclinations. I have shown that by using a two-component `relxill_lp` model, the spin inclination, and corona height can be estimated with higher accuracy, and that this method can also estimate the inclination of the outer disk and the radius of the warp between the inner and outer disks.

Using two-component `relxill_lp` models will become more important for the analysis of the energy spectra that the upcoming high-throughput missions *XRISM* and *Athena* will deliver. Even though our simulations were done with the resolution of *XRISM* and *Athena*, the disk warping may already show in the data from current satellites. This is particularly true for systems for which the inclinations of the two disk components towards the observer

differ significantly ($\phi = 0°$ at 25° inclination in Figure 4.8).

There are several potential targets for observation which may exhibit reflected power law emission from warped accretion disks.

Ingram et al. [75] explain the QPO from H 1743-322 as the result of asymmetric illumination of the disk, which may be a result of disk warping. Their best fit result gives an inner disk radius of $31.47^{+5.83}_{-3.66}$ r_g. This could be the location of r_{BP}, or it could be that the inner flow within this radius is not dense enough to contribute significantly to the iron fluorescence. Based on their form of Equation 3.1, they show that $\beta = 15°$ is consistent with the data within 0.5σ.

Recently, Connors et al. [35] analysed ASCA+RXTE data of XTE J1550-564 during a 1998 outburst in the hard-intermediate state. Using the latest `relxill` models, they found the inclination of the reflection region of the disk to be 40°, disagreeing with previous measurements that the jet is inclined at 75° [128]. Though disk warping may be the cause of this disagreement, they suggest alternatives such as a thick inner disk. Further work confirms this low inclination, suggesting that XTE J1550-564 may indeed contain a warped disk [36]. Fitting the H 1743-322 and XTE J1550-564 data with the warped disk models described in this chapter would be a worthwhile activity.

Chapter 5

Hard X-ray Polarimetry with X-Calibur

There drew he forth the brand Excalibur,
And o'er him, drawing it, the winter moon,
Brightening the skirts of a long cloud, ran forth
And sparkled keen with frost against the hilt:
For all the haft twinkled with diamond sparks,
Myriads of topaz-lights, and jacinth work
Of subtlest jewellery.
—Lord Tennyson, *Morte d'Arthur*

5.1 Introduction

In this chapter, I will discuss my contributions to the hard X-ray polarimeter X-Calibur, developed at Washington University over the last decade and culminating in a flight from McMurdo, Antarctica in the 2018-2019 Austral summer. In Section 5.2, I will discuss the theoretical background of the instrument before describing its individual components. I focus on my contributions to the alignment system, in particular my temperature testing of the X-ray mirror and design of an in-field aligner which we used during the Antarctic campaign

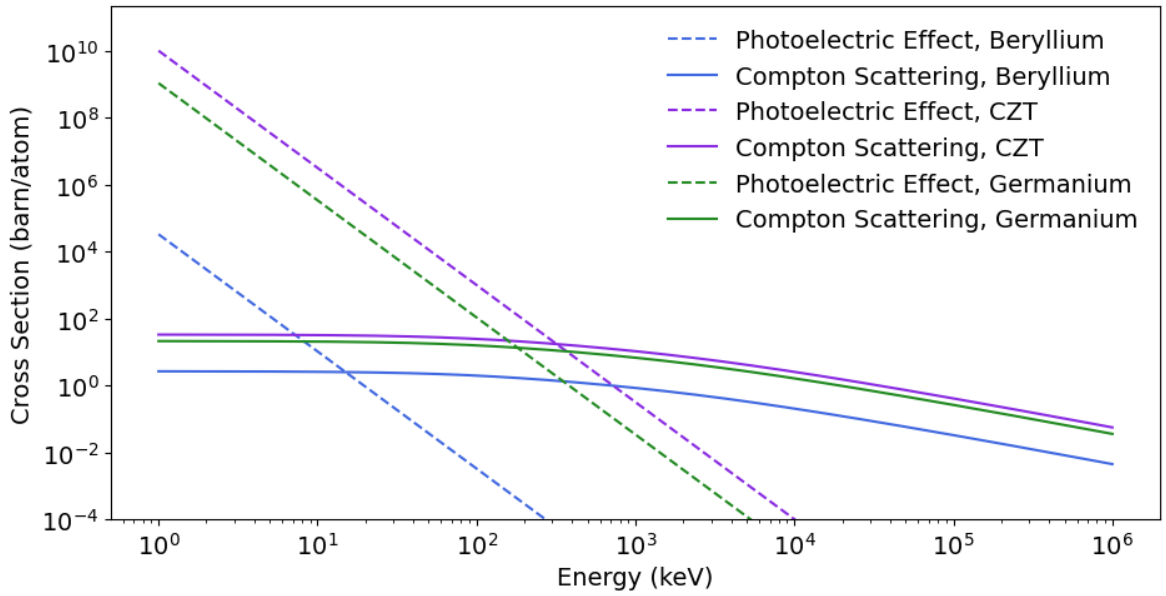

Fig. 5.1: The interaction cross sections for Compton scattering and photoelectric absorption in beryllium, CZT, and germanium.

to verify alignment of the mirror's optical axis with the polarimeter. In Section 5.3, I discuss the Antarctic campaign; this includes preparation and operation of the instrument, and background on the two mass accreting pulsars observed during the flight. Finally, in Section 5.4, I present and discuss the results from the flight.

5.2 Overview of X-Calibur

X-Calibur is a Compton polarimeter: its detection of the polarization is requisite upon the direction that X-rays Compton scatter. This is the dominant interaction for hard X-rays (above 10 keV or so). Below this, the photoelectric effect dominates; its cross section is proportional to $E^{-7/2}$, though, so quickly drops off with energy. It is also proportional to Z^5, so it is essential to choose a material with low effective atomic number. Figure 5.1 compares of the cross sections for Compton scattering and the photoelectric effect in several materials.

Krawczynski et al. [90] studied four potential detector geometries for a hard X-ray polarime-

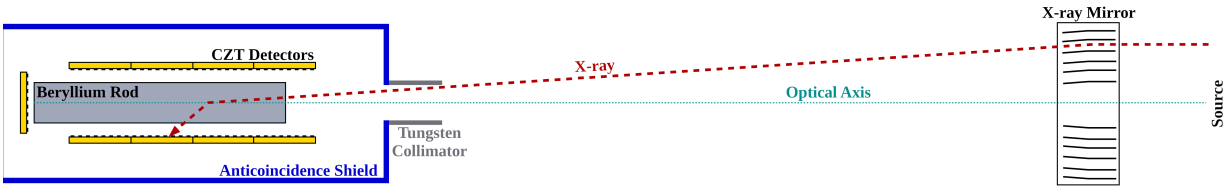

Fig. 5.2: Schematic view of X-Calibur. Source X-rays are focused by the InFocμs mirror onto a beryllium stick, where they scatter into the CZT detectors on all four sides of the stick. At the rear is a single CZT detector to image the X-rays which do not scatter in the beryllium stick. The entire detector is enclosed in a Caesium-Iodide anti-coincidence shield. (Adapted from Beilicke et al. [12])

ter, and found that a design consisting of a scintillating rod surrounded on four sides by CZT detectors offers the highest source rate and lowest MDP of the designs investigated. This geometry formed the basis for X-Calibur. X-Calibur has gone through several iterations during its design and testing stages (trading the scintillating rod for a beryllium scattering rod, for example), but I will focus on its final version which flew in 2018 and my contributions to this flight; for a description of the upgrades, see Beilicke et al. [12] and Kislat et al. [86].

A schematic view of X-Calibur is shown in Figure 5.2, and a picture of it assembled in McMurdo is shown in Figure 5.3. X-rays from the source are focused by a grazing incidence X-ray mirror onto the beryllium scattering stick, which is aligned with the mirror's optical axis. In the beryllium stick, photons scatter with an angular dependence according to the Klein-Nishina differential cross section [87]:

$$\frac{d\sigma}{d\Omega} = \frac{r_0^2}{2}\frac{k_1^2}{k_0^2}\left[\frac{k_0}{k_1} + \frac{k_1}{k_0} - \sin^2\theta\cos^2\eta\right], \tag{5.1}$$

where r_0 is the classical electron radius, k_0 and k_1 are the photon wave vectors before and after scattering, respectively, η is the incident angle between the photon electric field and the scattering plane, and θ is the outgoing angle of the photon after scattering. The Klein-Nishina cross section says that a polarized beam of light will scatter with a sinusoidal distribution peaked at $\pm 90°$ to the electric field direction of the polarized light.

After scattering in the beryllium stick, X-rays may deposit their energy in one of the CZT

Fig. 5.3: X-Calibur on 'The Boss' launch vehicle prior to its launch in 2018. On the left side is the detector, and on the right is the mirror.

detectors surrounding the stick, creating an electron-hole pair. These drift towards the anode and cathode of the pixel and their charge is read out by an Application Specific Integrated Circuit (ASIC). The polarimeter consists of sixteen CZTs surrounding the stick in four rings of four, and a seventeenth CZT at the rear for imaging. X-rays which pass through the scattering stick may deposit their energy in this CZT, providing rudimentary imaging that helps to verify alignment and pointing during the flight. Each CZT consists of thirty-two pixels and is read out by two ASICs of sixteen channels each.

One of the advantages of this 'scattering element' design is that due to the use of a focusing optic the collecting area is not tied to the size of the detector, and thus the polarimeter can be shielded from background on almost all sides. Compare this to the design of Compton polarimeters like PoGO+[26] or COSI[32], whose collecting area is based on the surface area of the polarimetry-sensitive detector, and by necessity their shielding cannot protect

one entire side of the polarimeter. X-Calibur is shielded by a Caesium Iodide 'bucket' into which the polarimeter is inserted and a 'plug' for the remaining side, which has a hole in it for the focused X-rays to go through. These two shield parts are each read out by four photomultiplier tubes. All of the focused X-rays travel through the hole in the top plug, and so anything going through the shield is background. Before a background particle deposits energy in one of the CZT detectors, it may scintillate in the CsI shield within a few microseconds of the polarimeter signal and be rejected.

The polarimeter is held in alignment with the optical axis of the mirror by a stiff truss made of carbon fiber tubes connected by aluminum joints. It is essential that the focal spot of the mirror is held as close to the center of the scattering stick as possible, and that any offset is well known; an uncorrected offset of just a few millimeters can create a false polarization signal of 10 % [see Figure 30 in 12, e.g.]. To monitor offset, we use camera aligned with the optical axis of the mirror to image an LED ring pattern attached to the polarimeter. The mirror's optical axis is aligned with the polarimeter pre-flight while truss at an elevation of 45°. By calibrating the LED ring position at this elevation, any deviation during flight is recorded as misalignment of the mirror optical axis.

Pointing of X-Calibur is done by the Wallops Arc-Second Pointer (WASP), a high precision pointing system designed for balloon platforms [146, 145]. The primary component of WASP is the pointing control system (PCS), consisting of two aluminium gimbal frames that provide pitch and yaw control. Each frame is rotated by two hubs; these consist of a brushless DC torque motor, with the central shaft constantly rotating to reduce the static friction. By finely balancing the truss such that its center of gravity is exactly at the intersection of the WASP hubs, pointing can be maintained with arcsecond precision. The Camera Attitude Reference Determination System (CARDS) star tracker is mounted on the front of the truss and is used to verify pointing.

5.2.1 The InFocμs X-ray Mirror

X-Calibur uses the InFocμs mirror, which has an 8 m focal length and 2.37′ angular resolution [127]. The InFocμs mirror consists of 255 shells of aluminium coated with platinum on carbon (Pt/C). It is a Wolter Type I mirror, meaning it consists of two sections, one paraboloid and one hyperboloid. Prior to the X-Calibur long duration balloon flight, the practice was to keep the mirror at roughly room temperature, above 20 °C at all times; any thermal deformation would move the focal spot or change its point spread function.

Temperature Testing

One of the critical concerns in launching balloon experiments is power usage; all instruments must either be powered by batteries stored onboard or through solar panels. To minimize power usage of mirror heaters during the flight, I temperature tested the mirror at Goddard Space Flight Center in the fall of 2017 with the guidance of Takashi Okajima and Takayuki Hayashi. They attached temperature sensors to all four quadrants of mirror and installed it in a thermal chamber on Goddard X-ray beamline. I lowered the temperature of the mirror down to 0.01 °C and imaged the focal spot. These images are shown in Figure 5.4; the reported temperatures are all averages of the values reported by all of the sensors. In Figure 5.5, I plot the movement of the focal spot with changing temperature against the size of the beryllium stick, as well as how the half power and 80 % power diameters change. I also plotted the point spread functions of the images, shown in Figure 5.6. The only PSF that is slightly different is at at 0.01 °C, possibly due to some instability in the cooler during this test. During flight, then, we switched on mirror heaters when the temperature reached 5 °C.

Alignment

A forward looking camera is installed on the InFocμs mirror and aligned with the mirror's optical axis. It is used to calibrate the WASP star tracker to position the target source in

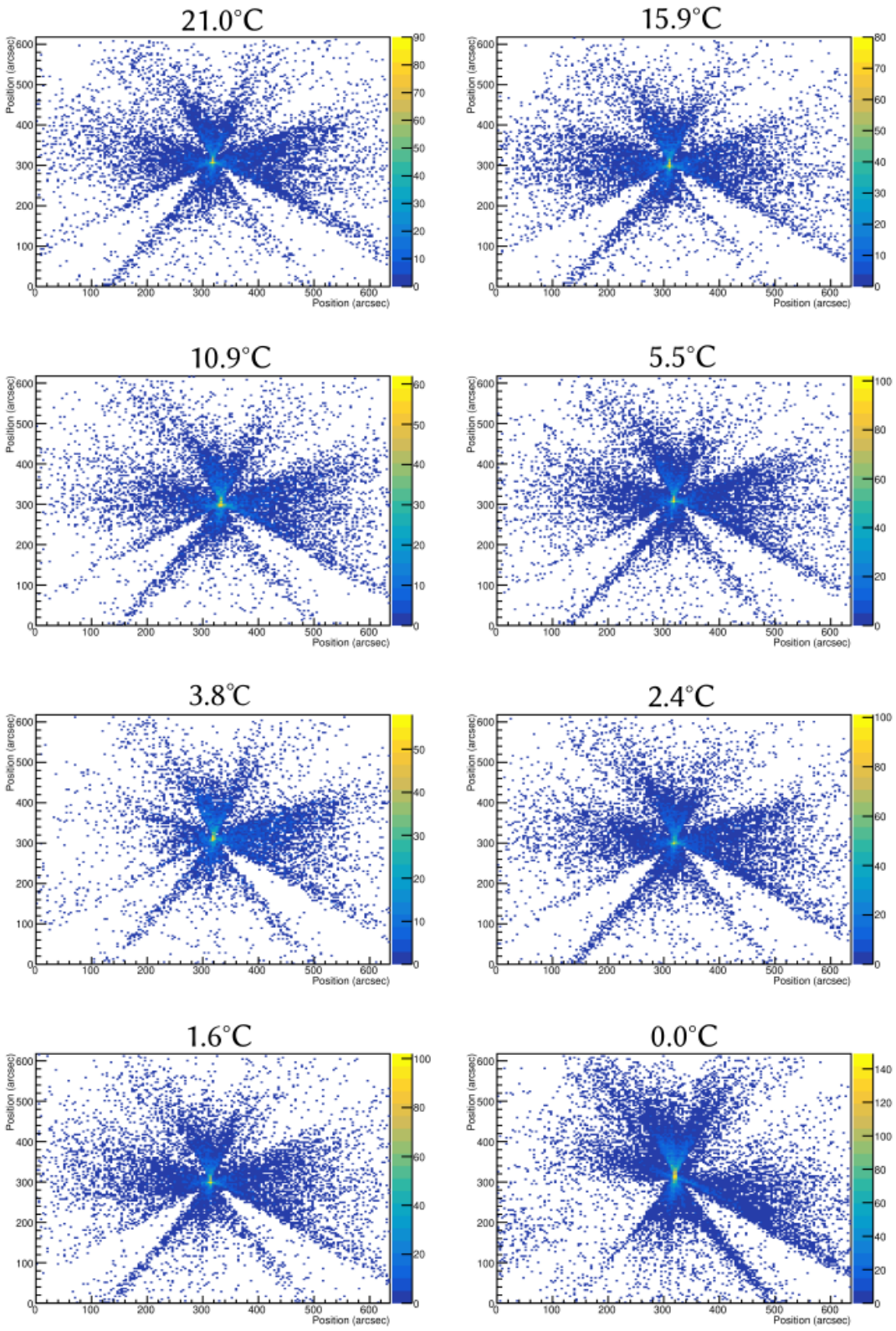

Fig. 5.4: Images of the InFocμs focal spot during temperature testing. The four quadrants of the mirror are clearly visible in all images. The color bars show the number of counts.

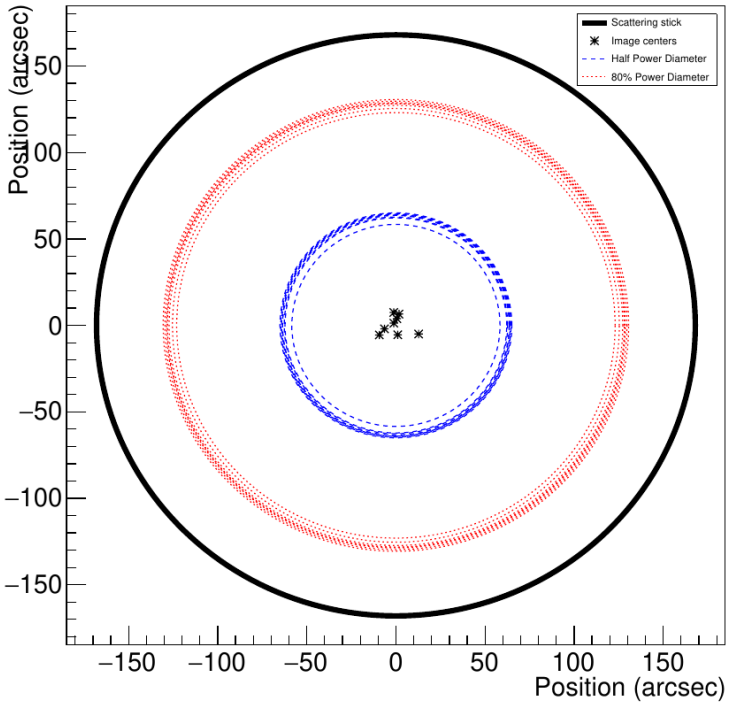

Fig. 5.5: The focal spot positions at all temperatures, and their half power (blue) and 80 % power diameters (red) compared to the size of the beryllium stick. The plotted diameters remain centered on the center of the beryllium stick, and are only shown to highlight that they do not significantly change with temperature. Assuming the focal spot is initally centered on the stick, lowering the temperature will have no significant effect on its position.

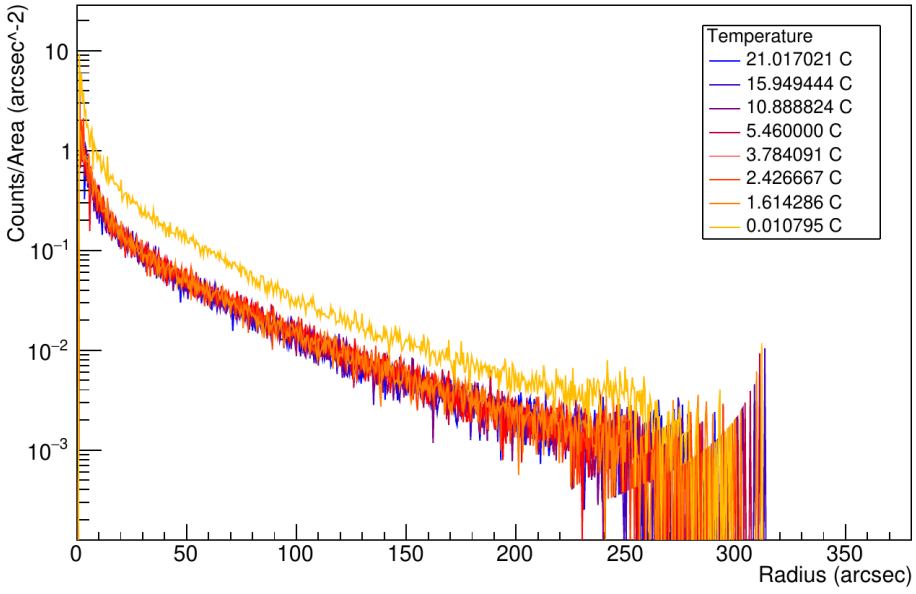

Fig. 5.6: Point spread functions of the InFocμs mirror during temperature testing. All PSFs look the same, with the exception of the lowest temperature at 0.01 °C. The reason is unknown, but possibly related to issues with the thermostat during this test.

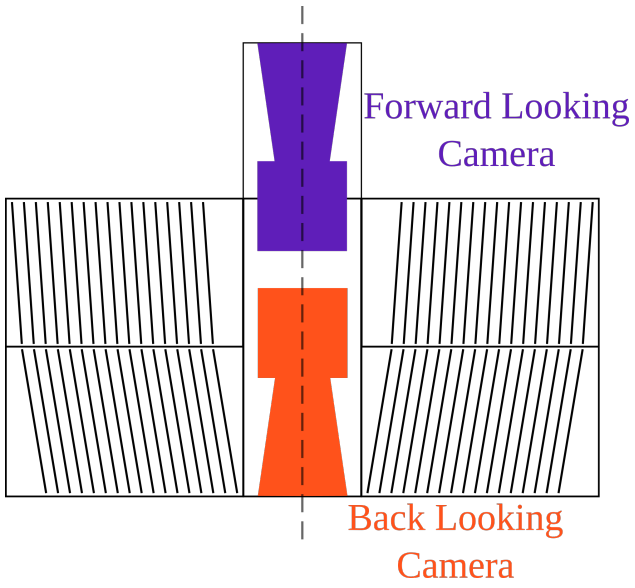

Fig. 5.7: Schematic of the mirror with the forward and back looking cameras, aligned with the optical axis of the mirror.

the field of view of the InFocμs mirror such that the X-rays are focused exactly onto the center of the scattering stick. A second camera is installed on the mirror looking backward, also aligned with its optical axis but viewing the polarimeter; this is the same camera used to image the LED ring. The positions of the target source in the forward looking camera and its focal spot in the back looking camera are recorded. A schematic of the mirror and cameras is shown in Figure 5.7.

At Goddard, the two cameras are installed and calibrated using a parallel beam of light. The parallel beam is created by a fiber-coupled lamp where the fiber endpoint, which emits as a point source, has been precisely placed at the focus of an off-axis parabolic mirror. The X-ray mirror is illuminated by this beam and a screen (simulating the polarimeter) is positioned 8 m away from the mirror so the focal spot lies on the screen. The back looking camera views this spot, and the forward looking camera views the light source (simulating the target source in the sky). The positions of these two points are recorded, so during flight we guarantee the focused X-rays are hitting the center of the scattering stick by positioning the target source in the corresponding position in the field of view of the forward looking camera.

Installation and calibration of the cameras were done at Goddard before the mirror unit was shipped to the field to be installed on the telescope. We wanted to check that the calibration remained valid after installation on X-Calibur, so I designed a portable alignment system, called the in-field aligner, based on the system at Goddard. To create the parallel beam of light, I used an off-the-shelf Schmidt-Cassegrain telescope and a fiber-coupled laser diode. By positioning the endpoint of the fiber in the eyepiece hole of the telescope at the focus of the telescope mirror assembly, I was able to create a parallel beam of light emitted from the front of the telescope. For the light source, I used a Class 3R 637.4 nm laser from ThorLabs, and for the telescope I used a 14 inch Celestron. We needed to be able to adjust the direction of the telescope assembly so the point source position in the forward looking camera matched the calibration, so the telescope was mounted on Newport rotation and tilt stages with millimeter precision. These stages were then attached to an aluminum frame which was mounted in front of the InFocμs mirror on the front panel of X-Calibur.

I tested the in-field aligner at Goddard in the summer of 2018 with the help of Takashi Okajima, practicing the procedure and verifying that in the lab the calibration was good. We recorded the image and source positions in the Goddard parallel beam, and then mounted the in-field aligner in front of the InFocμs mirror on a portable stand. Using the tilt and rotation stages, I moved the aligner until the source position in the forward looking camera matched the calibration, and verified that the position of the focal spot in the back looking camera matched the recorded position. Pictures of the focal spot produced by the Goddard lab setup and the in field aligner are shown in Figure 5.8.

In December 2018 in McMurdo, the procedure I developed was used to verify that the image locations in the forward and back looking cameras agreed to within 10″. An image of the aligner mounted on the front of X-Calibur during testing is shown in Figure 5.10, and the focal spot produced by the aligner on the detector is shown in Figure 5.9.

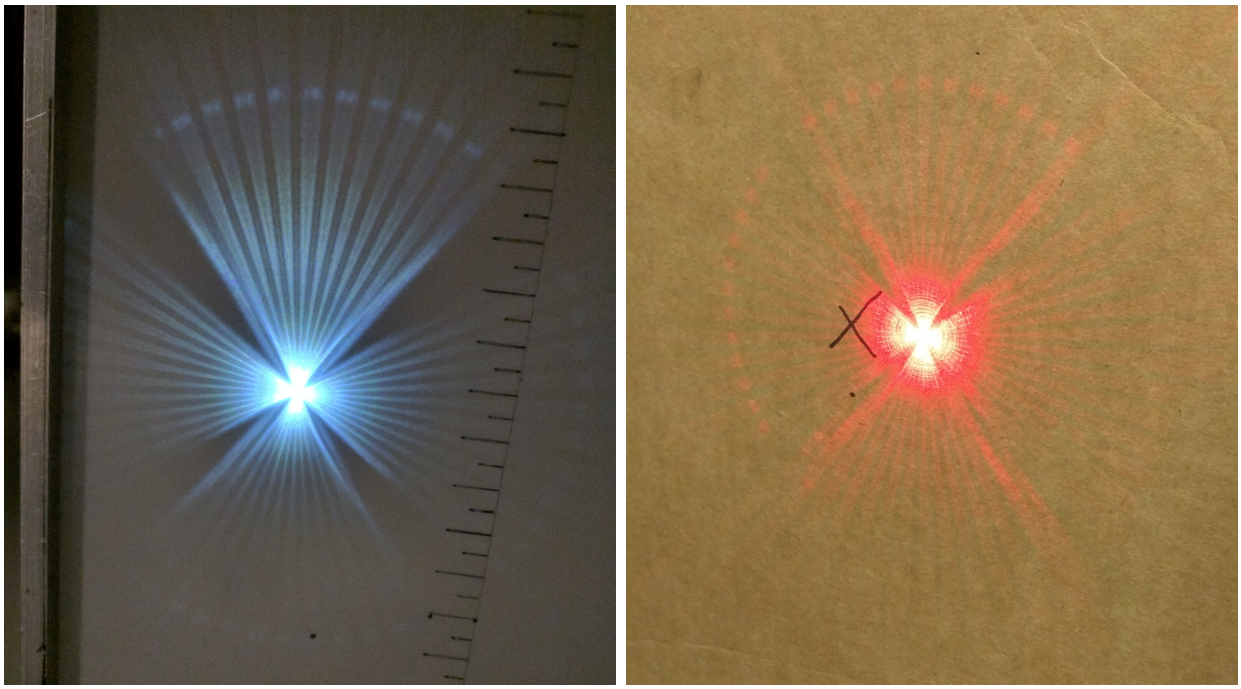

Fig. 5.8: Left: The focal spot of the parallel light beam produced by the calibration system at Goddard. This is on a screen placed approximately 8 m from the mirror. Right: Focal spot produced by the in-field aligner during testing at Goddard.

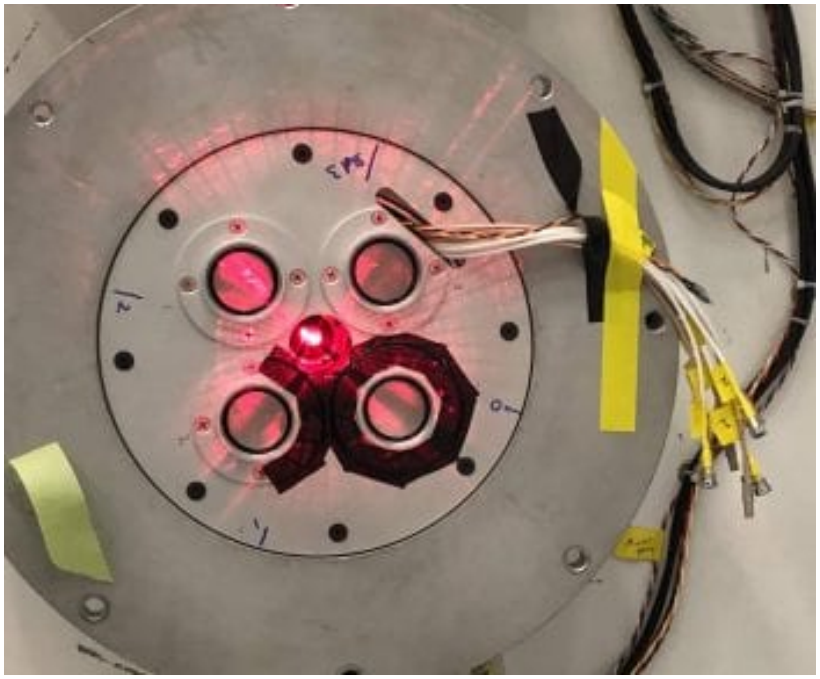

Fig. 5.9: The focal spot produced on the detector of X-Calibur by the in-field aligner in McMurdo. The focal spot is on the surface of the beryllium stick. Also visible are the four windows into the to CsI shield, onto which four photomultiplier tubes were attached before launch. Photo from Henric Krawczynksi.

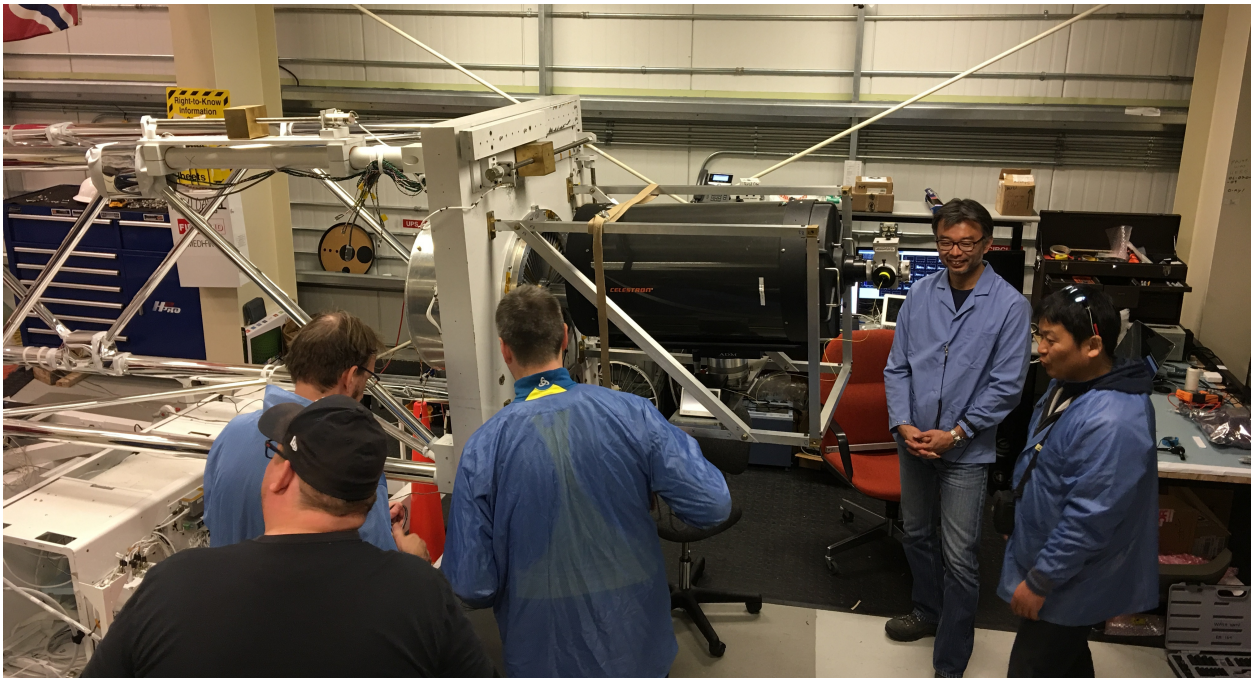

Fig. 5.10: The in-field aligner mounted on X-Calibur in front of the InFocμs mirror during preparation for the 2018 flight in McMurdo, Antarctica. Photo from Dana Braun.

5.3 2018-2019 Antarctic Campaign

After integration at the Wallops Flight Facility in February 2018 and the Columbia Scientific Ballooning Facility in July 2018, integration of X-Calibur began in McMurdo in mid November 2018. It launched at 20:45 UTC on 29 December. After several hours, it reached float altitude (39 km) and began alternating observations of two accreting pulsars, GX 301-2 and Vela X-1. About three days after launch, the flight was terminated prematurely over the Antarctic plateau due to a leak in the balloon. A single recovery trip to the remote landing site was conducted during the same season, bringing back the polarimeter to allow for refurbishment. During the 2019-2020 season, there was one more recovery trip (after a reconaissance flight to assess the landing site) during which the InFocμs mirror was recovered. Images of X-Calibur taken during these trips are shown in Figure 5.11.

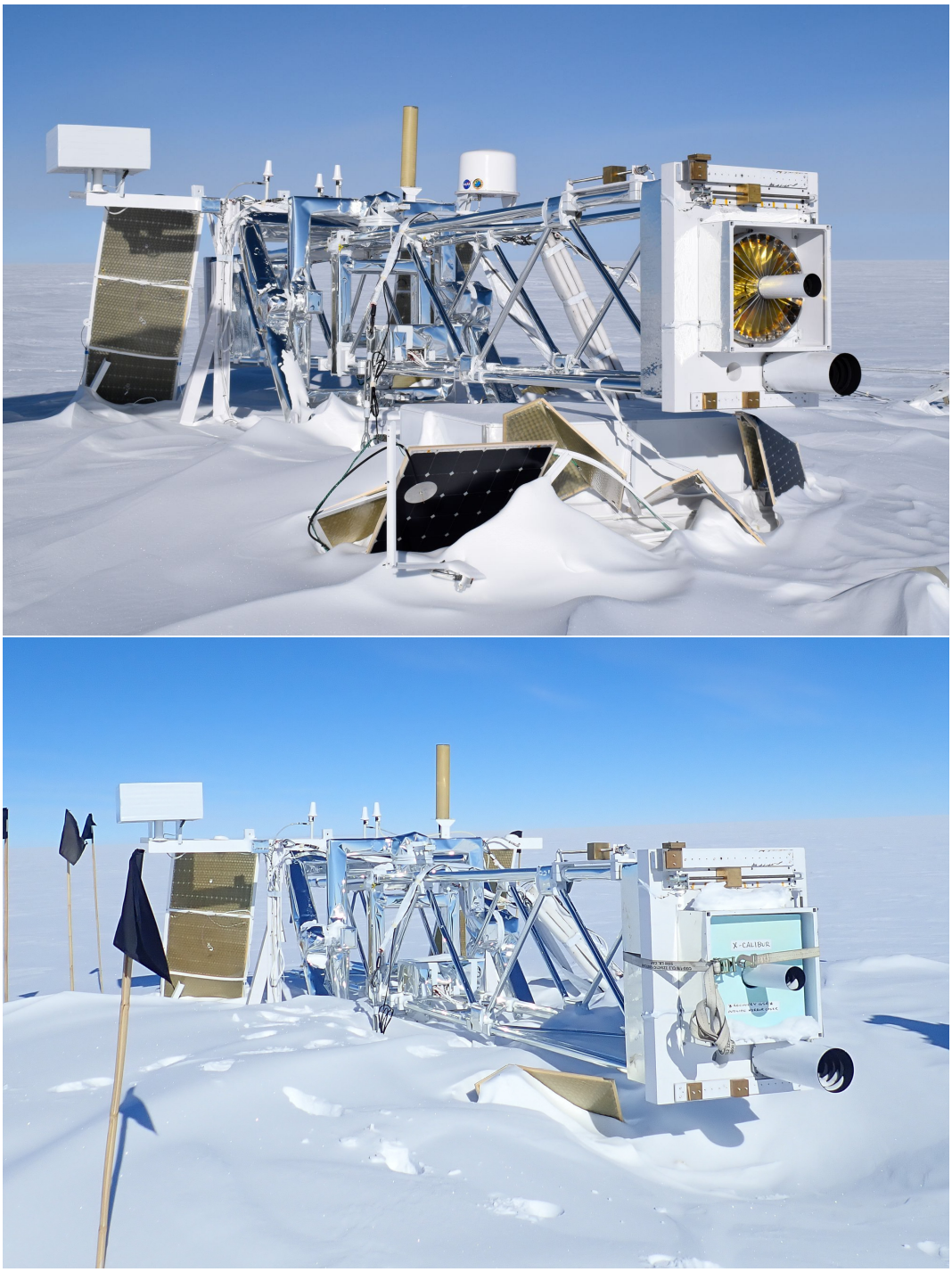

Fig. 5.11: Top: X-Calibur during recovery in 2019, approximately one month after the flight. The polarimeter end (back left, obscured by the gondola structure) was recovered, along with equipment from CSBF and WASP. Styrofoam panels were placed around the mirror to protect it from the weather until it could be recovered. Flags were places around the instrument to help future recovery missions find it. Photo from Scott Battaion. Bottom: X-Calibur during recovery in 2020, approximately one year after the flight. The mirror end of the truss (front right) was recovered. Photo from Lauren Brown.

Right Ascension	$12^{\,h}\ 26^{\,m}\ 37.561^{\,s}$
Declination	$-62°\,46'\,13.260''$
Orbital period	41.5 days
Spin period	681 s
Companion type	B1.5Ia
Accretion rate	$10^{-5}\,M_\odot\,yr^{-1}$[81]

Tab. 5.1: Summary of properties of GX 301-2 and its optical companion Wray 997, compiled from Bildsten et al. [14] unless otherwise noted.

5.3.1 Observed Sources

GX 301-2

GX 301-2 is a pulsar orbiting the star Wray 997 (aka BP Crucis); Table 5.1 summarizes its known properties. The mass of the neutron star is not well constrained, though the optical companion is 39–53 $M_\odot$[81].

The magnetic field estimates from its CRSF are on the order of 10^{12} G[42], which is lower than the $\sim 10^{14}$–10^{15} G generally required to explain the pulsar period: the lower magnetic field strength would not exert enough torque on the neutron star to prevent the accreting matter from spinning it up to a higher period than we observe [141]. This discrepency may suggest that the CRSF originates high up in the accretion column, which is consistent with the fan beam model [42].

Fürst et al. [54] resolved the CRSF into two separate features, one at 37 keV and one at 50 keV, though their energy can shift by several kiloelectronvolts over the pulsar phase [147]. They posit that these two lines are not harmonically related, but instead are two separate features from regions at different heights above the neutron star: the higher energy feature comes from the surface, and the lower energy feature comes from a shock in the accretion column about 1.4 km above the surface.

Very predictably during its 40.5 days orbit, GX 301-2 is bright for several days as it approaches periastron; occasionally, it also flares right before apastron. In the past, GX 301-2

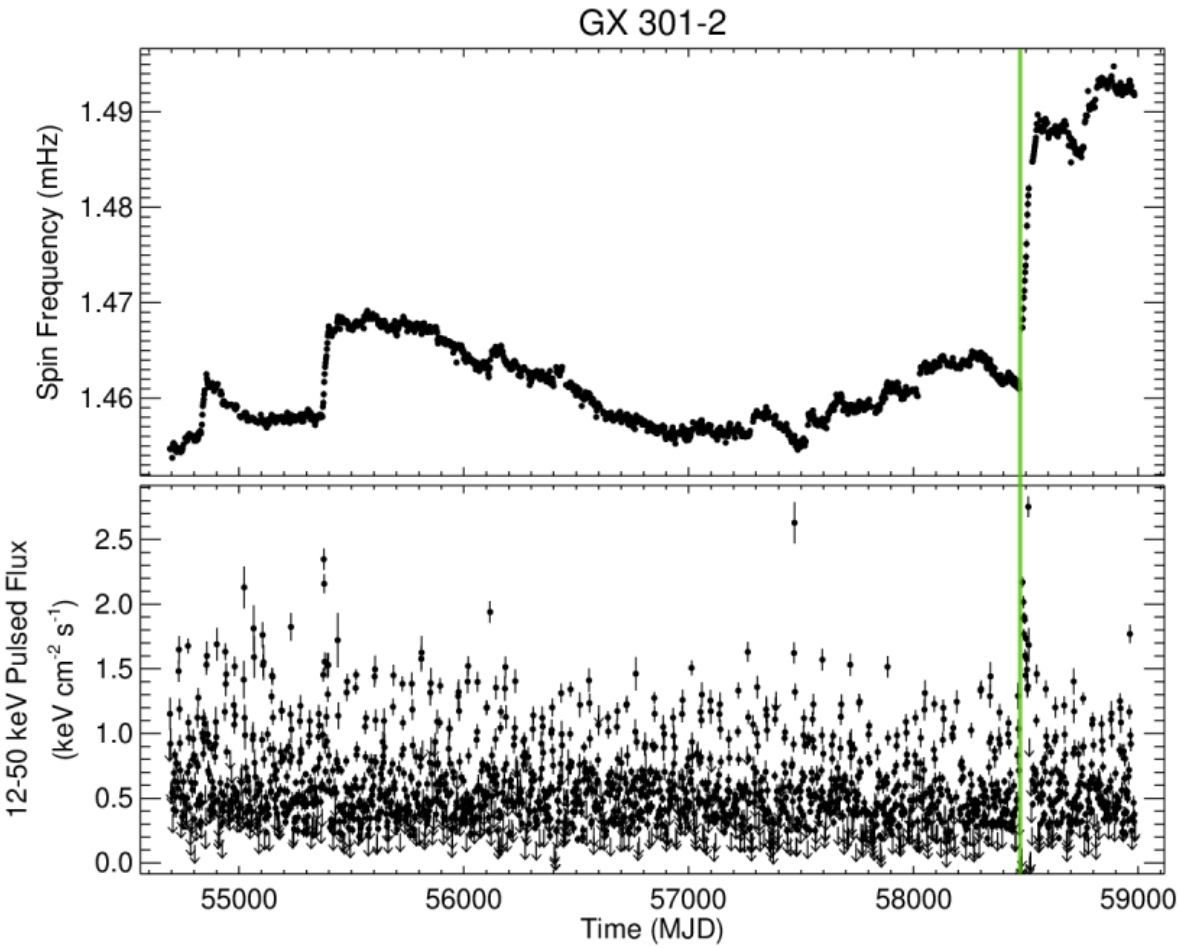

Fig. 5.12: Fermi Gamma-Ray Burst Monitor result for GX 301-2 (from NSSTC Web Page [124]), showing an unusual period of spin-up in the top plot beginning during the X-Calibur observation (approximate duration highlighted in green). Simultaneous was a period of high flux, unusual during this part of the binary orbit.

has undergone periods of rapid spin-up and associated flares [88, 14]; one such example is visible around MJD 55400 in the spin frequency and flux from the Fermi Gamma-Ray Burst Monitor shown in Figure 5.12. When X-Calibur launched, GX 301-2 was in the midst of a similar period of spin-up, during which a temporary disk likely formed around the neutron star [114]. The approximate duration of the X-Calibur observation is highlighted in green on Figure 5.12.

Right Ascension	$9^{\,h}\ 2^{\,m}\ 6.861^{\,s}$
Declination	$-40°\,33'\,16.91''$
Orbital period	8.96 days
Spin period	283.2 s
Companion type	B0.5Iae
Accretion rate	$6.3 \times 10^{-7}\,M_\odot\,yr^{-1}$[62]
Orbital separation	$1.8\,R_\star$[134]
Neutron Star Mass	$2.12\,M_\odot$

Tab. 5.2: Summary of properties of Vela X-1 and its optical companion HD 77581, compiled from Bildsten et al. [14] and Falanga et al. [47] unless otherwise noted.

Vela X-1

Vela X-1 is an accreting pulsar whose properties are summarized in Table 5.2. Its binary orbit is highly inclined; for one day out of the nine day orbit, we see the source eclipsed, with little to no X-ray flux [47]. The other eight days it is persistently active at a rate around 200 mCrab, with occasional outburts of much higher activity; this reliability makes it an ideal target for a long-duration balloon campaign. The orbital separation is quite small, leaving the neutron star embedded within the stellar wind. This helps explain the persistant X-ray flux, as it has a constant source of matter for accretion. It is possible that amidst this wind-fed accretion, a persistent disk-like structure is able to form due to beaming of the outflow by the orbit [45].

5.3.2 Flight Operations

After the WASP checkout and calibration sequence at the beginning, X-Calibur began observing GX 301-2 at an elevation of ∼55°. Once it rose above 60°, X-Calibur slewed to Vela X-1 and observed this until the next day when GX 301-2 lowered below 60°. This observing pattern is visible in Figure 5.13, where the pointing elevation is shown. Above 60° the balloon blocks the field of view of the CARDS star tracker, leaving WASP unable to maintain pointing.

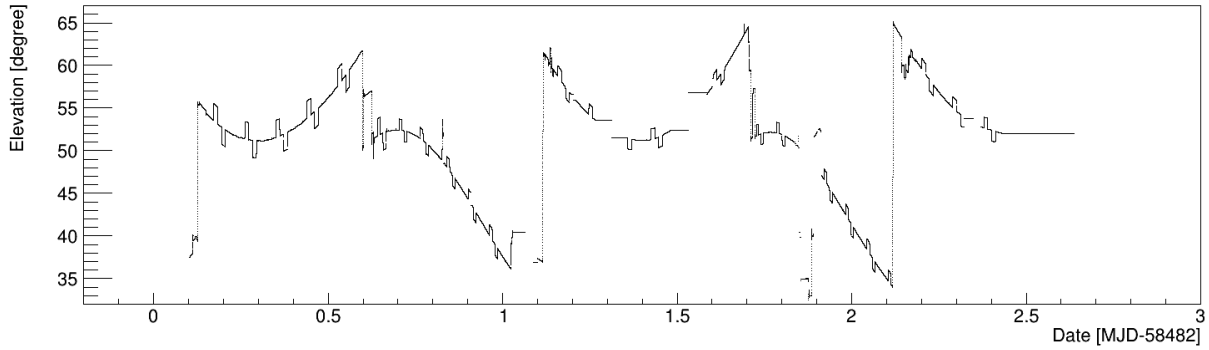

Fig. 5.13: Pointing elevation of X-Calibur during the flight. The arcs of GX 301-2 and Vela X-1 elevation are visible as X-Calibur alternated between the two. The excursions above and below each arc are from background pointings 1° away from the source every 15 minutes.

X-Calibur alternated 15 minutes pointing at the source and 15 minutes pointing 1° away for background measurement. Off pointings cycled through four directions so as not to contaminate the off measurements with some unknown source or anisotropy in the X-ray background. To reduce systematic errors and non-uniformities in the detector, the polarimeter unit rotated at 2 RPM.

To minimize the rate of telemetered data, X-Calibur performed several data cuts onboard; specifically, it cut events that coincided with a shield trigger and events with more than three pixels. When an X-ray deposits energy in the CZT, there is a slight (a few percent) chance that its charge will be shared between neighboring pixels, thus being read out as a two-pixel event. In general, though, a multipixel event occurs when an atmospheric particle travels through the detector, depositing energy on opposite sides of the polarimeter, or when electronic noise is present in the ASICs.

5.4 Results from the Flight

This section contains results originally presented in Abarr et al. [1]. I helped to take the data during the flight, made minor contributions to the text, and contributed to the development of 'xana', the code used to produce these results; in particular, I added a module to convert

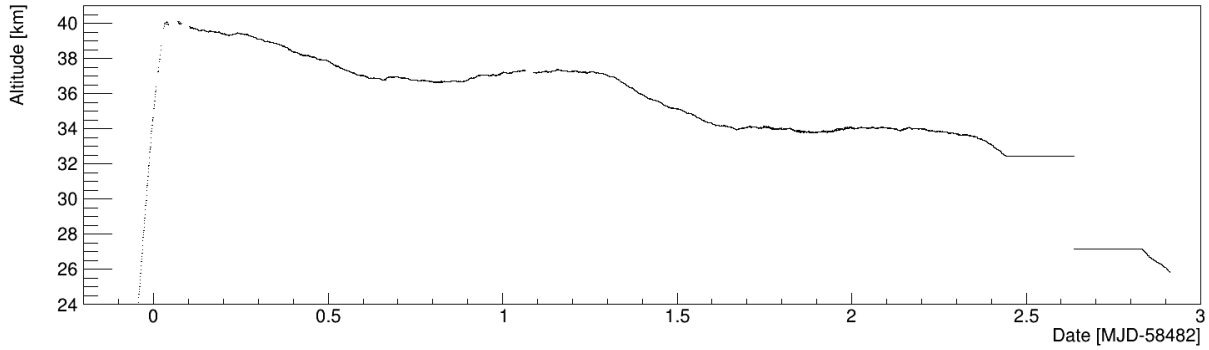

Fig. 5.14: Altitude of X-Calibur during the flight. After about 1.5 days, it dropped low enough in the atmosphere to block the majority of source X-rays.

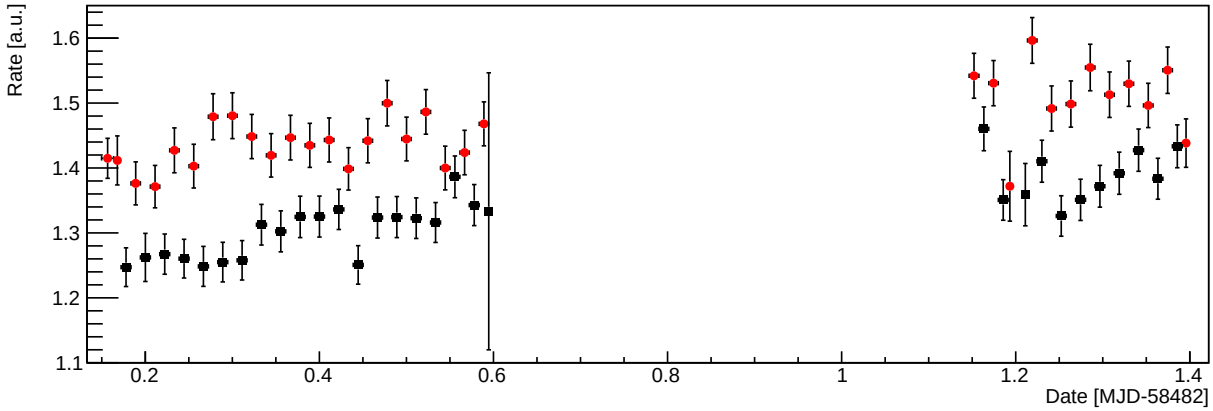

Fig. 5.15: Light curve for GX 301-2 taken by X-Calibur, in 20 min bins. In red are the ON pointings and in black are OFF. The average source count rate is 0.23 Hz

photon arrival time into pulsar phase.

Only data from the first day and a half of the flight show a significant detection; after this, the atmospheric column above the instrument was too large. In Figure 5.14 it is clear that around the 1.5 day mark X-Calibur dips below 35 km and never regains altitude before the end of the flight.

The total observation length for GX 301-2 was 8.0 h on source and 7.8 h off, and for Vela X-1 was 7.9 h on and 7.8 h off. This produced the light curves shown in Figures 5.15 and 5.16, respectively.

The Vela result is consistent with no detection, likely because its low elevation required a longer observation than the abbreviated flight allowed.

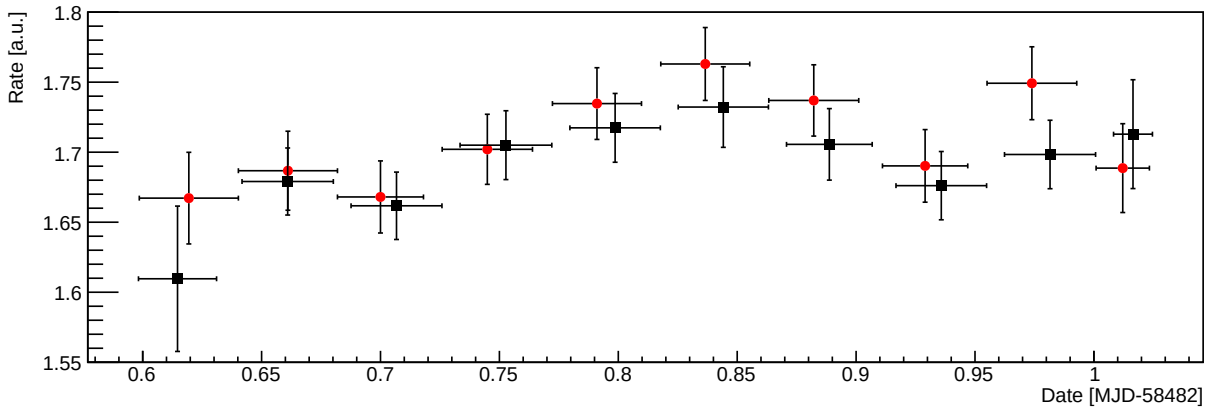

Fig. 5.16: Light curve for Vela X-1 taken by X-Calibur, binned in 1 h intervals. In red are the ON pointings and in black are OFF. At all times the source rate is consistent with a non-detection.

There is, however, a clear signal from GX 301-2. We see in Figure 5.15 the excess while pointing at the source, which gives an average source rate of 0.23 Hz. Using the spin-up measurements from Fermi GBM [124], we were able to phase-bin the spectrum. The average pulse profile measured over the entire X-Calibur observation is shown in Figure 5.17. Since our statistics are not high enough for a full phase-resolved polarization analysis, we calculated the polarization for two division: the pulse peak, with phase 0.8 to 1.14, and the off peak, with phase 0.14 to 0.8.

For the polarization analysis, each event is given a scattering angle $\chi = \arctan(x/y)$, where in the polarimeter frame x points east and y points north. Based on this scattering angle, each event is assigned Stokes parameters $Q = -\frac{2}{\mu}\cos(2\chi)$ and $U = -\frac{2}{\mu}\sin(2\chi)$, and an intensity $I = 1$. The Stokes parameters of all the contributing events are summed with weights based on their location within the polarimeter. One weighting factor is based on the depth of the event in the polarimeter, since photons are more likely to Compton scatter towards the top. The other factor is based on its scattering angle, since pixels towards the center of the CZTs cover a larger angle from the scattering axis. Q and U are then normalized to $\mathcal{Q} = Q/I$ and $\mathcal{U} = U/I$, so if $\mathcal{Q} = 1$ or $\mathcal{U} = 1$ the signal is fully polarized. From these normalized Stokes parameters, the polarization fraction is calculated with $\sqrt{\mathcal{Q}^2 + \mathcal{U}^2}$ and polarization

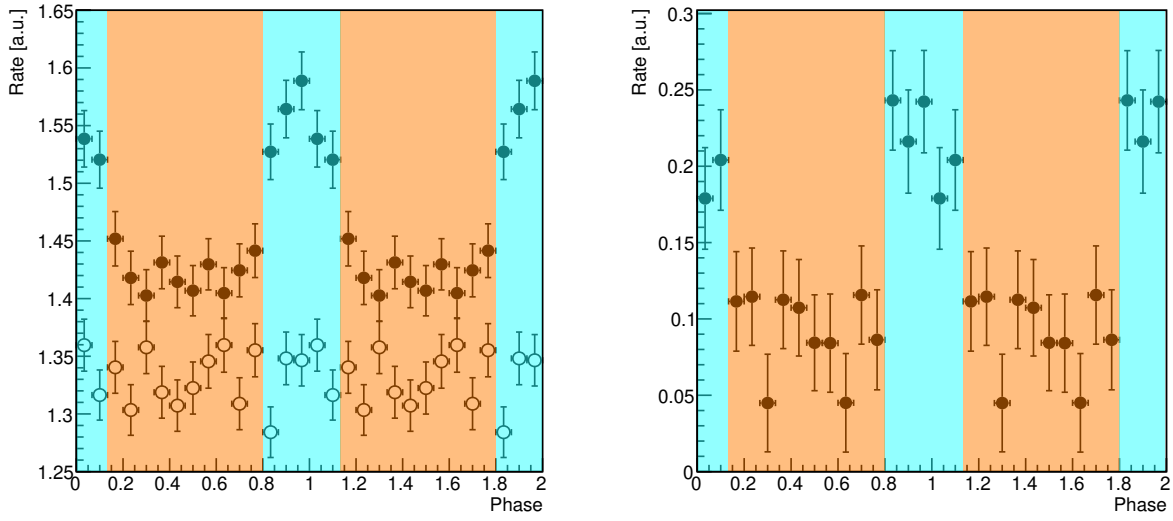

Fig. 5.17: Left: On-source (filled points) and off-source (open) phase binned light curve for GX 301-2. Right: On-off pulse profile. Highlighted in blue is the pulse peak (phase 0.8-1.14), and in orange is the off peak (0.14-0.8).

	Entire Pulse	Pulse Peak (0.8-1.14)	Off Peak (0.14-0.8)
$\mathcal{Q}$	0.184 ± 0.194	0.266 ± 0.212	0.083 ± 0.335
$\mathcal{U}$	0.202 ± 0.194	0.161 ± 0.211	0.246 ± 0.336
$\Pi(\%)$	27^{+38}_{-27}	32^{+41}_{-32}	27^{+55}_{-27}
$\chi(^\circ)$	21 ± 43	30 ± 40	10

Tab. 5.3: Polarization results from X-Calibur for 15-25 keV, with errors reported at the 90 % confidence level. The Off Peak polarization angle is unconstrained at this level.

angle with $\frac{1}{2}\arctan(\mathcal{U}/\mathcal{Q})$. Results are shown in Figure 5.18 plotted in the $\mathcal{Q}-\mathcal{U}$ plane, and are summarized in Table 5.3.

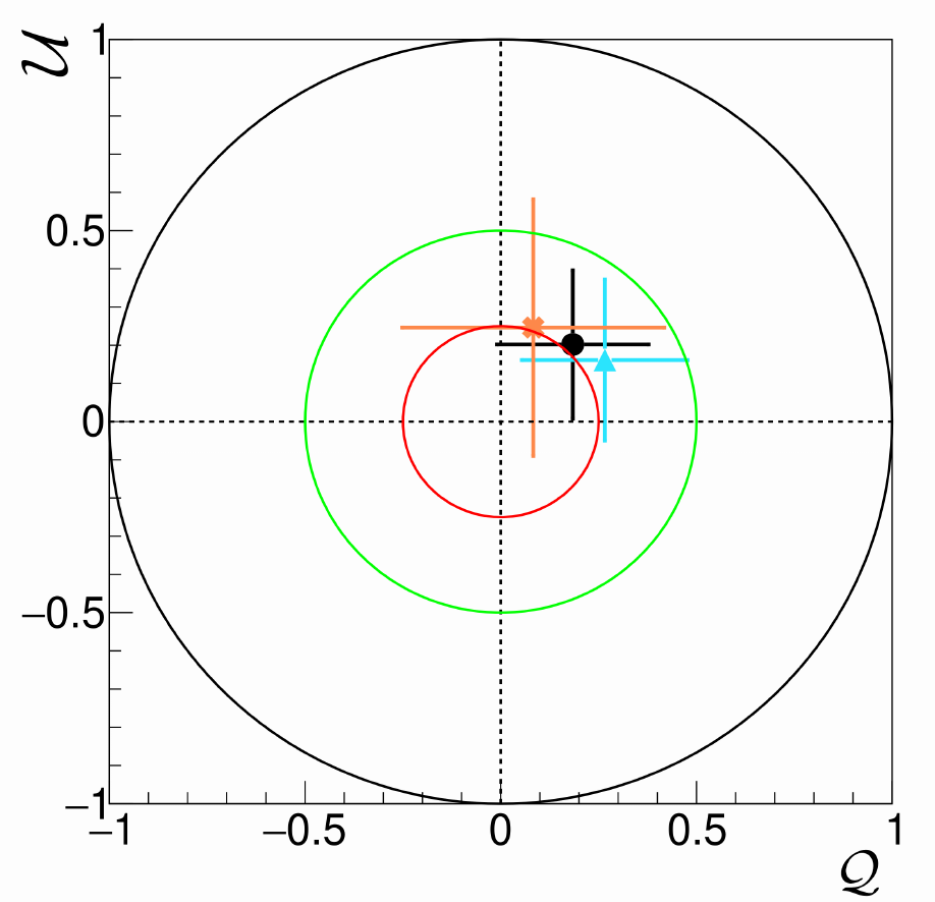

Fig. 5.18: Normalized Stokes parameters for the entire pulse (black dot), peak (blue triangle), and off peak (orange cross). Error bars on each show the 1σ statistical errors. The red circle corresponds to 25 % polarization, the green circle to 50 % polarization, and the black circle to 100 %. An unpolarized source would lie at the origin, with $\mathcal{Q} = \mathcal{U} = 0$.

Chapter 6

Outlook and Summary

Sanity returns (in most cases) when the book is closed.

—Ursula K. Le Guin, *The Left Hand of Darkness*

6.1 Future X-ray Polarimeters

6.1.1 XL-Calibur

To build on the success of the first flight, the X-Calibur collaboration is currently planning and constructing its follow-up, XL-Calibur, scheduled to fly from northern Sweden across the Atlantic Ocean on a roughly week-long flight in 2022. It is based on the same design principles but with several key upgrades. The truss length will be extended from 8 m to 12 m to accomodate the focal length of a new mirror, originally fabricated for the FFAST mission [151]. The FFAST mirror is made of 213 aluminum shells coated with a Pt/C multilayer, and has an energy-dependent effective area 3 to 10 times better than the InFocμs mirror [7, 105]. At the time of writing, the second out of three alignments has taken place at the SPring-8 facility in Japan; the third will take place in late 2020 or early 2021, and the final calibration of the mirror will take place in 2021. Construction and testing of the new 12 m truss is in progress at Washington University in St. Louis, led by Lindsey Lisalda. I expect that with minor refurbishment the in-field aligner will be reused during campaigns to verify alignement of the FFAST mirror with the polarimeter.

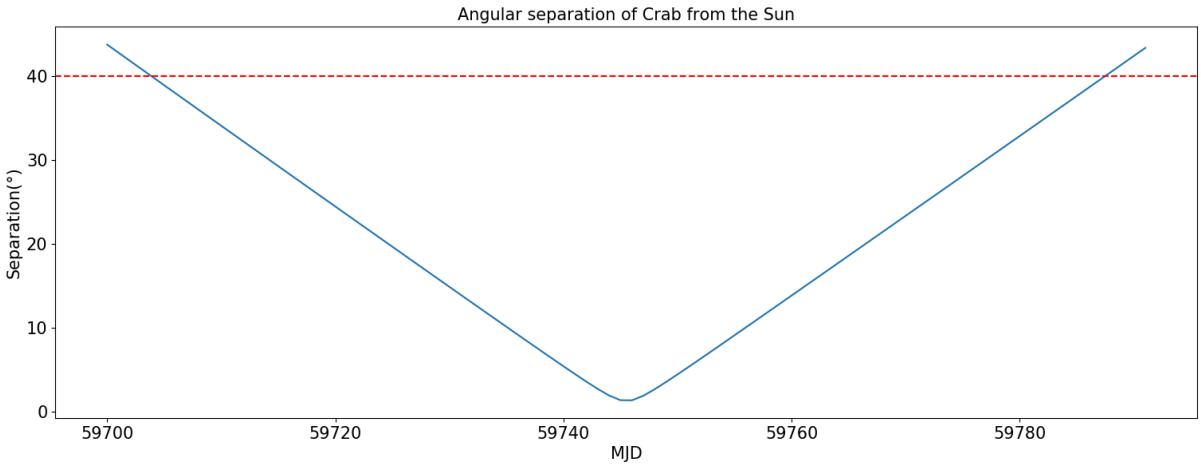

Fig. 6.1: The angular distance in the sky between the Crab nebula and the Sun during the months of May, June, and July in 2022, when XL-Calibur is planning to fly from Sweden. The Crab will be at its closest on June 15, about 1° from the Sun. The dotted red line marks the limit for how close X-Calibur could observe near the Sun during its 2018 flight.

A key target for the flight from Sweden will be the Crab nebula, one of the best studied X-ray sources in the sky. During the summer, though, the Crab goes behind the Sun; a plot of their separation is shown in Figure 6.1. This presents an issue because X-Calibur was unable to observe sources within 40° of the Sun. Within this limit, sunlight washes out all the background stars in the CARDS star tracker and pointing cannot be maintained; this prevented X-Calibur from observing a flaring black hole candidate during the 2018 flight. From Sweden, X-Calibur would be unable to view the Crab during all but the very earliest and very latest launch windows. To address this, an off-axis star tracker and a sun sensor will be installed on XL-Calibur. This will allow pointing to be maintained for the Crab, as well as any target of opportunity sources, throughout a much larger portion of the flight window. The new limiting factor will be the thermal limits of the FFAST mirror and polarimeter as they approach direct illumination by the sun.

XL-Calibur will also use an improved polarimeter. In addition to an all new ASIC readout system, incorporating the noise-reducing lessons learned during preparation for the 2018 flight, the 2 mm thick CZTs used during the 2018 flight will be replaced by 0.8 mm thick CZTs. While 1-5 % fewer signal photons will be absorbed by these thinner detectors, the

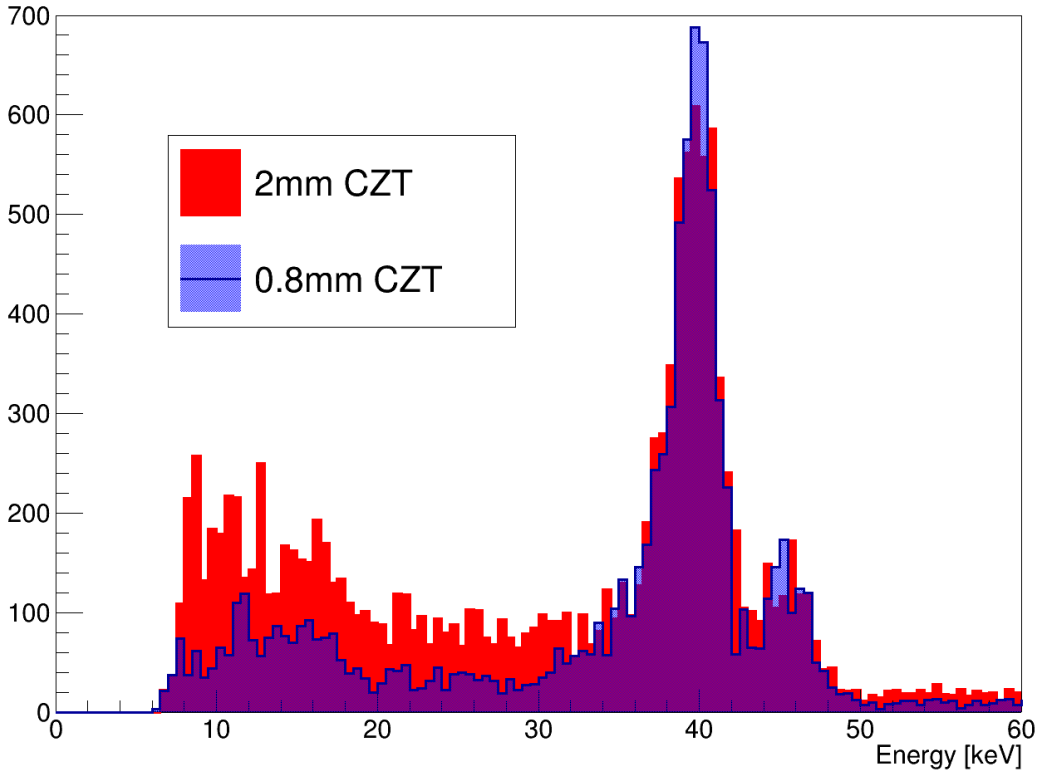

Fig. 6.2: An example Eu152 spectra in one pixel of a 2 mm CZT and a 0.8 mm CZT. The 0.8 mm tends have a slightly higher energy resolution, and a smaller low-energy tail near the energy threshold.

background rate will be 69 % of that seen by the thicker detectors, resulting in an overall higher signal-to-noise ratio. And example of a 2 mm versus 0.8 mm spectrum is shown in Figure 6.2, showing the smaller low-energy tail in the 0.8 mm CZTs.

Background will be further reduced by improved shielding, currently being designed and fabricated by the team at KTH in Stockholm. This will include quicker electronics and lower energy threshold. The shield anticoincidence window will be reduced from 6 µs to 2 µs. The shield flag, anticoincidence flag, and event flag from X-Calibur are shown in Figure 6.3. For XL-Calibur, the start of the anticoincidence window will be delayed after the shield flag to reduce the dead time. This will reduce the background by a factor of ∼2.

To illustrate the capabilities of XL-Calibur, we can compare it to previous polarimetric measurements. As mentioned earlier in this thesis, OSO-8 measured the polarization fraction of the Crab nebula at 2.6 keV to be (19.2 ± 1.0) %, with a polarization angle of $(156.0 \pm 1.4)°$

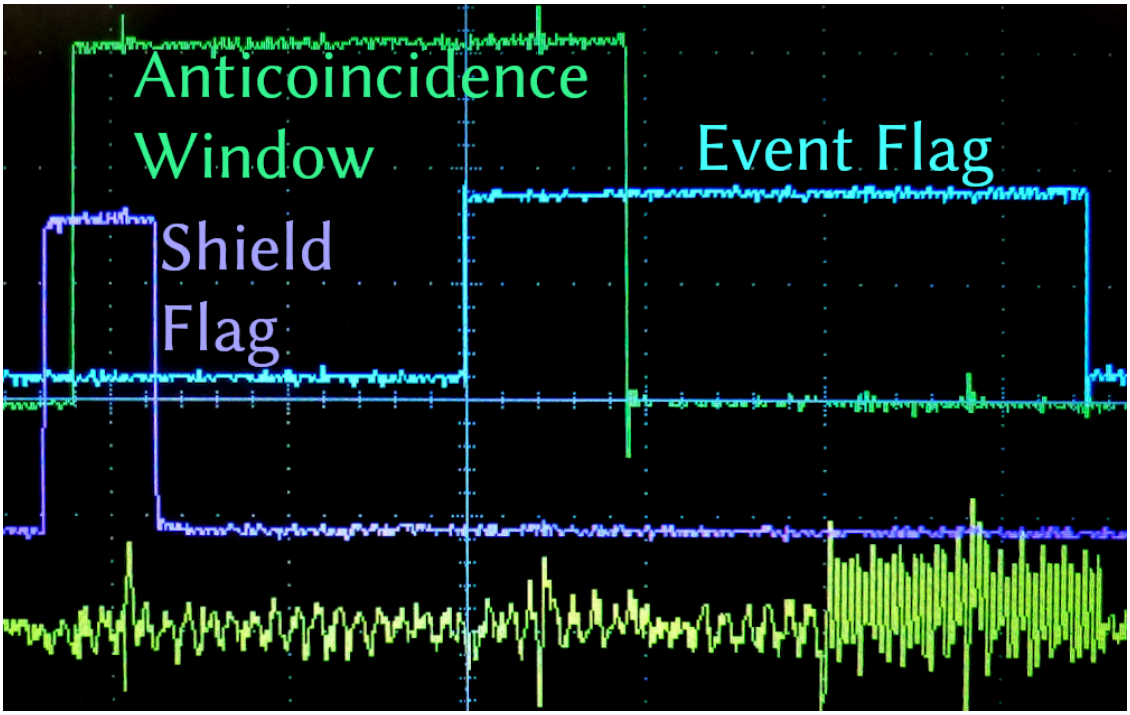

Fig. 6.3: The shield, anticoincidence, and event flags in the X-Calibur electronics. When an event flag overlaps with the anticoincidence flag, the event is discarded. By delaying the start of the anticoincidence flag from the shield flag, the dead time will be reduced.

[159]. This resulted from 71.2 h pointing on the source and 71.3 h off. More recently, the PoGO+ observation of the Crab nebula from its July 2016 balloon flight took almost two days of data, 25.56 h on and 21.94 h off. For its entire energy range, about 18-160 keV, PoGO+ measured a polarization fraction of $(20.9 \pm 5.0)\,\%$ and angle of $(131.3 \pm 6.8)°$ [27]. When resolving the data into pulse phase and removing the peak, leaving the emission dominated by just the nebula, Chauvin et al. found a polarization fraction of $17.4^{+8.6}_{-9.3}\%$ and angle of $(137 \pm 15)°$. To compare XL-Calibur to these previous measurements, in Figure 6.4 I show a simulated 48 h observation, divided equally between on and off target. This is a reasonable assumption for observation length given that XL-Calibur's maiden flight will follow roughly the same path as the 2016 PoGO+ flight. This shows that over the energy range 20-60 keV XL-Calibur will be able to resolve the polarization in 10 keV bins with an MDP of $<10\,\%$.

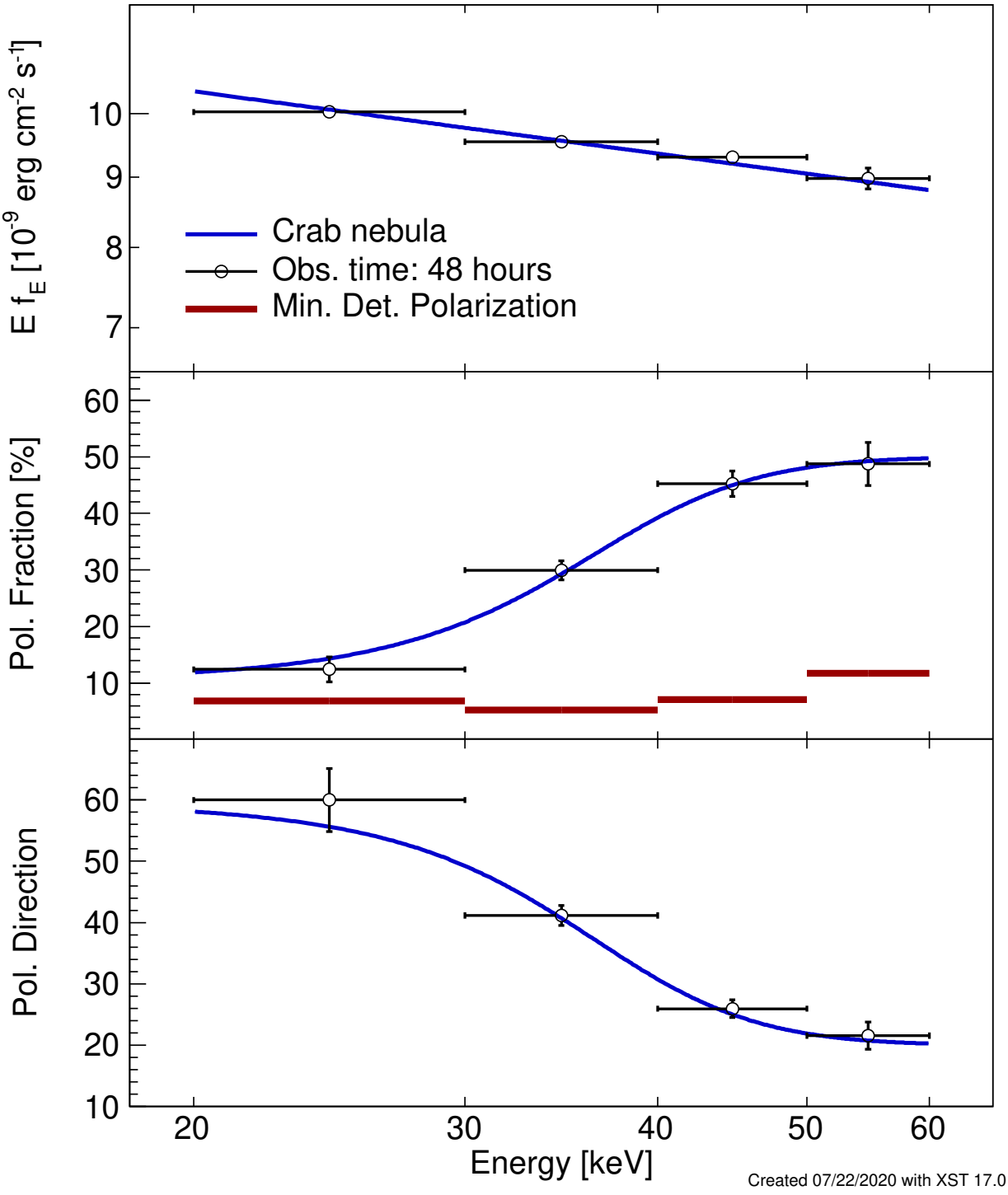

Fig. 6.4: Simulated XL-Calibur observation for 48 hours of observation.

6.1.2 The Imagining X-ray Polarization Explorer

2021 will see the launch of a satellite polarimeter, the Imaging X-ray Polarimetry Explorer (IXPE) [161]. IXPE contains three coaligned telescopes, each consisting of a mirror focusing X-rays onto a gas pixel detector (GPD). The GPD is of a gas cell in which X-rays produce photoelectrons, emitted preferentially to the X-ray's polarization. The electron ionizes the gas, and the path of this ionization track is read out by a gas electron multiplier. The initial direction of the electron gives information about the X-ray polarization, and its location of emission gives imaging [37]. The photoelectron changes direction as it ionizes the gas and slows down, so key to measuring the polarization is correctly interpreting the shape of track to find the emission point of the electron and its initial direction.

As IXPE operates on the photoelectric effect, its observational energy range is limited to where this is the dominant interaction, about 2 to 8 keV. In this range, it will be able to map the magnetic fields of supernova remnants, AGN jets, and pulsar wind nebulae from the polarization of the synchrotron X-ray emission from these sources.

6.1.3 Others

IXPE will hopefully be just the first satellite X-ray polarimeter of a new era: PolSTAR, eXTP, COSI, and XPP are several other missions that may fly in the future. PolSTAR (Polarimetric Spectroscopic Telescope Array) is a satellite version of X-Calibur, combining the polarimetric capabilities of X-Calibur with the optical bench of NuSTAR [92]. eXTP (enhanced X-ray Timing and Polarization mission) consists of a large area detector, and spectroscopic array, and a polarimetric array based on the design of IXPE; it is scheduled to be launched by the Chinese Academy of Sciences by 2025 [165].

Compton Spectrometer and Imager (COSI)

COSI is a balloon-borne gamma-ray instrument with a 0.2-5 MeV bandpass [32] that was recently selected to move forward with a satellite mission [148]. COSI consists of layers of

germanium strips alternating direction in each layer, cryogenically cooled below 80 K. One of the main goals of COSI is to map the positron annihilation line at 511 keV in the center of the galaxy, but it will also detect gamma-rays from gamma-ray bursts (GRBs), black holes, and neutron stars. Due to the inherent polarimetry-sensitive nature of Compton scattering, COSI will be able to detect the polarization of signals as low as 15 mCrab. Previous measurements have indicated that GRBs may be highly polarized [34, 63], so constraining the polarization of these is one of the main goals of COSI. Within its initial two year mission lifetime, the COSI satellite is likely to see about 40 GRBs, translating into an MDP of about 50 %.

X-ray Polarization Probe (XPP)

XPP is a design concept for a second generation X-ray polarization observatory [77]. It has a large bandpass of 0.2-60 keV, achieved by combining several focal plane instruments sensitive in different energy ranges. XPP would have three Wolter I mirrors, two of which illuminate identical large bandpass modules and a third illuminating an IXPE-like gas pixel detector which offers imaging in a small bandpass. The large bandass module consist of three instruments: a Low, Medium, and High Energy Polarimeter (LEP, MEP, and HEP). The LEP (0.2-2 keV) is a diffraction grating taking advantage of the polarization dependence of Bragg diffraction and is transparent above 2 keV [102, 103]. X-rays which are transmitted through the LEP are incidence on the MEP (2-10 keV), which like IXPE reads out the inital direction of photoelectrons to measure polarization. In this case, it is based on the design of PRAXyS [69], which utilized a Time Projection Chamber (TPC) [15] to read out the electron tracks. There will be a window at the back of the MEP which allows X-rays >10 keV to exit into the HEP, which is based on the X-Calibur and PolSTAR designs [92]. The HEP will differ from X-Calibur in that the monolithic beryllium scattering element will be replaced by a composite of beryllium, lithium hydride, and scintillator to optimize the Compton scattering cross section across the entire 10-60 keV range.

6.2 Advancements in Simulation

6.2.1 Combining Ray-Tracing and GRMHD

One of the major drawbacks of ray-tracing codes such as the one described in Chapter 2 is that they rely on idealized models. They make simplifying assumptions about the disk structure and time evolution of the system, and thus are of limited use when it comes to timing predictions and simulations. To improve on this, we can use GRMHD simulation results to inform our ray-tracing. This can allow us to feed realistic disk structures into our ray-tracing code and evolve it with time, which would be difficult to do while simultaneously tracking radiation through the environment. This project is currently underway, led by Andrew West at Washington University in St. Louis and Matthew Liska at Harvard. We hope to be able to confirm the link between warped disk precession and QPOs [73, 75].

6.2.2 Polarization in Magnetic Fields

The magnetic field around compact objects can strongly impact the polarization. Faraday rotation is an important effect in photons travelling through the plasma in black hole coronae and disks, and around highly magnetized neutron stars (called magnetars), the prediction of QED vacuum birefringence becomes significant.

Faraday Rotation

In the plasma of coronae and disks around black holes, the magnetic fields cause the plane of polarization of photons to rotate. Davis et al. [38] use the following equation for a photon traveling the distance of the Thompson optical depth τ_T:

$$\chi_F = \frac{3\lambda^2 \tau_T}{16\pi^2 e} \overrightarrow{\mathbf{B}} \cdot \hat{\mathbf{k}}, \tag{6.1}$$

where e is electron charge, $\overrightarrow{\mathbf{B}}$ is the magnetic field, $\hat{\mathbf{k}}$ is the photon wave vector, and λ is the photon wavelength. Due to the wavelength dependence, this effect will be weak for X-rays unless the magentic field is quite strong, on the order of 10^5-10^6 G. The net effect of Faraday rotation will be to depolarize the emission, as the polarization angle of photons from similar locations will be rotated away from each other by slight path differences. When considering paths through the accretion disk atmosphere, this effect will be small since the disk is geometrically thin; it will be less so for the lamppost corona, which relies on its size to capture and Comptonize photons. Stronger still will be the effect of Faraday rotation for extended corona models [11], where photons spend more time in the corona.

QED Birefringence

One of the early predictions of quantum electrodynamics is that the magnetized vacuum is birefringent [140]. This requires enormous magnetic fields for the effect to be significant, and so it has yet to be observed in a laboratory. In magnetars, however, where the magnetic field can reach $\sim 10^{15}$ G, this effect may become observable. Around black holes, Caiazzo and Heyl [21] show that this can depolarize the X-rays, especially around black holes with higher angular momenta where it is more likely that photons will orbit around the black hole several times, thus spending more time in the magnetic field, before reaching the observer. Around neutron stars, however, QED birefringence can instead increase the polarization. Heyl and Caiazzo [68] demonstrate that around magnetars, the polarization angle of the source follows the direction of the magnetic field far from the star, which can lead to polarization fractions of nearly 100 %. They predict that this is the case around the source 4U 0142+61, and identify it as an ideal target of observation for IXPE.

6.3 Summary

In this thesis, I have presented the results from my work studying X-rays from warped black hole accretion disks, as well as my contributions to observational X-ray polarimetry through my work on X-Calibur.

In Chapter 2, I summarized the methods and abilities of the ray-tracing code used by our group [91]. I improved the computational ability of this code by implementing the embedded Cash-Karp method with adaptive step size. Additionally, in this chapter I described the warped accretion disk model which I added to the code.

I used this warped disk model in Chapter 3 to simulate the polarization signature from such disks. In this chapter, adapted from Abarr and Krawczynski [3], I found that polarization angle can be a diagnostic of disk warping in the case of systems which have previous measures of orientation (from jet inclination or binary orbit, for example), while the energy spectrum and polarization fraction may be difficult to use to measure disk warping. Using this code, I simulated IXPE observations of two possible sources: Cygnus X-1 and GRO J1655-40, both candidates for containing misaligned disks. I found that these sources likely have low polarization fractions, requiring long observation lengths.

Chapter 4 contains my results from simulating the reflection spectrum from warped disks using XILLVER, originally presented in Abarr and Krawczynski [2]. I show that the consideration of photons which scatter multiple times is more important for warped disks, especially when the warp radius is small or the warp degree is large. To determine the effect that disk warping has on the measured properties of black hole systems, specifically inclination and spin, I fit my simulated spectra with the `relxill_lp` model in XSPEC, and find that these parameters can be measured with greater accuracy by using a two part `relxill_lp` model, one for each segment of the disk. In particular, this will become more important as more advanced missions such as XRISM [164] and Athena [115] are launched in the coming years.

I discuss my contributions to X-Calibur, the balloon-borne hard X-ray polarimeter, in Chapter 5. In particular, I worked on the alignment system: I temperature tested the mirror to

help determine the operating temperature during flight and designed a portable system to verify the alignment of the mirror after installation on the truss. I took part in the 2018-2019 long duration balloon campaign in McMurdo, Antarctica, and helped in the analysis of the resulting data that led to the first polarimetric constraint of the accreting pulsar GX 301-2. Finally, in Chapter 6 I have discussed several future endeavors. I discussed the future of X-ray polarimetry, including my contributions to the upcoming mission XL-Calibur, and presented details of the upcoming satellite IXPE. I ended by presenting several projects which are in the works that improve the usefulness and accuracy of ray-tracing simulations, including the addition of the effects of a strong magnetic field as well as implementing a disk structure informed by GRMHD results.

References

[1] Q. Abarr et al. "Observations of a GX 301-2 Apastron Flare with the X-Calibur Hard X-Ray Polarimeter Supported by NICER, the Swift XRT and BAT, and Fermi GBM." In: ApJ 891.1, 70 (Mar. 2020), p. 70. DOI: 10.3847/1538-4357/ab672c. arXiv: 2001.03581 [astro-ph.HE].

[2] Quincy Abarr and Henric Krawczynski. *The Iron Line Profile from Warped Black Hole Accretion Disks*. 2020. arXiv: 2008.03829 [astro-ph.HE].

[3] Quincy Abarr and Henric Krawczynski. "The Polarization of X-Rays from Warped Black Hole Accretion Disks." In: ApJ 889.2, 111 (Feb. 2020), p. 111. DOI: 10.3847/1538-4357/ab5fdf. arXiv: 1912.00243 [astro-ph.HE].

[4] *About RXTE - PCA*. Dec. 6, 2011. URL: https://heasarc.gsfc.nasa.gov/docs/xte/learning_center/pca.html.

[5] Eric Agol and Julian H. Krolik. "Magnetic Stress at the Marginally Stable Orbit: Altered Disk Structure, Radiation, and Black Hole Spin Evolution." In: ApJ 528.1 (Jan. 2000), pp. 161–170. DOI: 10.1086/308177. arXiv: astro-ph/9908049 [astro-ph].

[6] K. A. Arnaud. "XSPEC: The First Ten Years." In: *Astronomical Data Analysis Software and Systems V*. Ed. by George H. Jacoby and Jeannette Barnes. Vol. 101. Astronomical Society of the Pacific Conference Series. Jan. 1996, p. 17.

[7] Hisamitsu Awaki et al. "Hard x-ray telescopes to be onboard ASTRO-H." In: Appl. Opt. 53.32 (Nov. 2014), p. 7664. DOI: 10.1364/AO.53.007664.

[8] James M. Bardeen and Jacobus A. Petterson. "The Lense-Thirring Effect and Accretion Disks around Kerr Black Holes." In: ApJ 195 (Jan. 1975), p. L65. DOI: 10.1086/181711.

[9] James M. Bardeen, William H. Press, and Saul A. Teukolsky. "Rotating Black Holes: Locally Nonrotating Frames, Energy Extraction, and Scalar Synchrotron Radiation." In: ApJ 178 (Dec. 1972), pp. 347–370. DOI: 10.1086/151796.

[10] Peter A. Becker and Michael T. Wolff. "Thermal and Bulk Comptonization in Accretion-powered X-Ray Pulsars." In: ApJ 654.1 (Jan. 2007), pp. 435–457. DOI: 10.1086/509108. arXiv: astro-ph/0609035 [astro-ph].

[11] Banafsheh Beheshtipour, Henric Krawczynski, and Julien Malzac. "The X-Ray Polarization of the Accretion Disk Coronae of Active Galactic Nuclei." In: ApJ 850.1, 14 (Nov. 2017), p. 14. DOI: 10.3847/1538-4357/aa906a. arXiv: 1710.00247 [astro-ph.HE].

[12] M. Beilicke et al. "Design and Performance of the X-ray Polarimeter X-Calibur." In: *Journal of Astronomical Instrumentation* 3.2, 1440008 (Dec. 2014), p. 1440008. DOI: 10.1142/S225117171440008X. arXiv: 1412.6457 [astro-ph.IM].

[13] Ronaldo Bellazzini. *X-ray Polarimetry : A New Window in Astrophysics.* Cambridge Contemporary Astrophysics. Cambridge University Press, 2010. ISBN: 9780521191845. URL: http://libproxy.wustl.edu/login?url=http://search.ebscohost.com/login.aspx?direct=true&db=e000xna&AN=320444&site=ehost-live&scope=site.

[14] Lars Bildsten et al. "Observations of Accreting Pulsars." In: ApJS 113.2 (Dec. 1997), pp. 367–408. DOI: 10.1086/313060. arXiv: astro-ph/9707125 [astro-ph].

[15] J. K. Black et al. "X-ray polarimetry with a micropattern TPC." In: *Nuclear Instruments and Methods in Physics Research A* 581.3 (Nov. 2007), pp. 755–760. DOI: 10.1016/j.nima.2007.08.144.

[16] Omer Blaes. "General Overview of Black Hole Accretion Theory." In: Space Sci. Rev. 183.1-4 (Sept. 2014), pp. 21–41. DOI: 10.1007/s11214-013-9985-6. arXiv: 1304.4879 [astro-ph.HE].

[17] C. T. Bolton. "Identification of Cygnus X-1 with HDE 226868." In: Nature 235.5336 (Feb. 1972), pp. 271–273. DOI: 10.1038/235271b0.

[18] Niel Brandt and Philipp Podsiadlowski. "The effects of high-velocity supernova kicks on the orbital properties and sky distributions of neutron-star binaries." In: MNRAS 274.2 (May 1995), pp. 461–484. DOI: 10.1093/mnras/274.2.461.

[19] Laura W. Brenneman and Christopher S. Reynolds. "Constraining Black Hole Spin via X-Ray Spectroscopy." In: ApJ 652.2 (Dec. 2006), pp. 1028–1043. DOI: 10.1086/508146. arXiv: astro-ph/0608502 [astro-ph].

[20] I. Caballero and J. Wilms. "X-ray pulsars: a review." In: Mem. Soc. Astron. Italiana 83 (Jan. 2012), p. 230. arXiv: 1206.3124 [astro-ph.HE].

[21] Ilaria Caiazzo and Jeremy Heyl. "Vacuum birefringence and the x-ray polarization from black-hole accretion disks." In: Phys. Rev. D 97.8, 083001 (Apr. 2018), p. 083001. DOI: 10.1103/PhysRevD.97.083001. arXiv: 1803.03798 [astro-ph.HE].

[22] B. Carter. "Axisymmetric Black Hole Has Only Two Degrees of Freedom." In: Phys. Rev. Lett. 26.6 (Feb. 1971), pp. 331–333. DOI: 10.1103/PhysRevLett.26.331.

[23] Jeff R Cash and Alan H Karp. "A variable order Runge-Kutta method for initial value problems with rapidly varying right-hand sides." In: *ACM Transactions on Mathematical Software (TOMS)* 16.3 (1990), pp. 201–222.

[24] Subrahmanyan Chandrasekhar. *Radiative transfer*. 1960.

[25] M. Chauvin et al. "Polarimetry in the Hard X-Ray Domain with INTEGRAL SPI." In: ApJ 769.2, 137 (June 2013), p. 137. DOI: 10.1088/0004-637X/769/2/137. arXiv: 1305.0802 [astro-ph.IM].

[26] M. Chauvin et al. "Calibration and performance studies of the balloon-borne hard X-ray polarimeter PoGO+." In: *Nuclear Instruments and Methods in Physics Research A* 859 (July 2017), pp. 125–133. DOI: 10.1016/j.nima.2017.03.027. arXiv: 1703.07627 [astro-ph.IM].

[27] M. Chauvin et al. "Shedding new light on the Crab with polarized X-rays." In: *Scientific Reports* 7, 7816 (Aug. 2017), p. 7816. DOI: 10.1038/s41598-017-07390-7. arXiv: 1706.09203 [astro-ph.HE].

[28] M. Chauvin et al. "Accretion geometry of the black-hole binary Cygnus X-1 from X-ray polarimetry." In: *Nature Astronomy* 2 (June 2018), pp. 652–655. DOI: 10.1038/s41550-018-0489-x. arXiv: 1812.09907 [astro-ph.HE].

[29] M. Chauvin et al. "The PoGO+ view on Crab off-pulse hard X-ray polarization." In: MNRAS 477.1 (June 2018), pp. L45–L49. DOI: 10.1093/mnrasl/sly027. arXiv: 1802.07775 [astro-ph.HE].

[30] Maxime Chauvin et al. "PoGO+ polarimetric constraint on the synchrotron jet emission of Cygnus X-1." In: MNRAS 483.1 (Feb. 2019), pp. L138–L143. DOI: 10.1093/mnrasl/sly233. arXiv: 1812.03244 [astro-ph.HE].

[31] Yifan Cheng et al. "X-ray spectropolarimetric signature of a warped disk around a stellar-mass black hole." In: *Classical and Quantum Gravity* 33.12, 125015 (June 2016), p. 125015. DOI: 10.1088/0264-9381/33/12/125015. arXiv: 1505.01562 [gr-qc].

[32] J. -L. Chiu et al. "The upcoming balloon campaign of the Compton Spectrometer and Imager (COSI)." In: *Nuclear Instruments and Methods in Physics Research A* 784 (June 2015), pp. 359–363. DOI: 10.1016/j.nima.2014.11.099.

[33] Daniel Clery. "Update: Telescope designed to study mysterious dark energy keeps Russia's space science hopes alive." In: *Science* (July 15, 2019). DOI: 10.1126/science.aay3154. URL: https://www.sciencemag.org/news/2019/07/update-

telescope-designed-study-mysterious-dark-energy-keeps-russia-s-space-science.

[34] Wayne Coburn and Steven E. Boggs. "Polarization of the prompt γ-ray emission from the γ-ray burst of 6 December 2002." In: Nature 423.6938 (May 2003), pp. 415–417. DOI: 10.1038/nature01612. arXiv: astro-ph/0305377 [astro-ph].

[35] Riley M. T. Connors et al. "Conflicting Disk Inclination Estimates for the Black Hole X-Ray Binary XTE J1550-564." In: ApJ 882.2, 179 (Sept. 2019), p. 179. DOI: 10.3847/1538-4357/ab35df.

[36] Riley M. T. Connors et al. "Evidence for Returning Disk Radiation in the Black Hole X-Ray Binary XTE J1550-564." In: ApJ 892.1, 47 (Mar. 2020), p. 47. DOI: 10.3847/1538-4357/ab7afc. arXiv: 2002.11873 [astro-ph.HE].

[37] Enrico Costa et al. "An efficient photoelectric X-ray polarimeter for the study of black holes and neutron stars." In: Nature 411.6838 (June 2001), pp. 662–665. arXiv: astro-ph/0107486 [astro-ph].

[38] Shane W. Davis et al. "The Effects of Magnetic Fields and Inhomogeneities on Accretion Disk Spectra and Polarization." In: ApJ 703.1 (Sept. 2009), pp. 569–584. DOI: 10.1088/0004-637X/703/1/569. arXiv: 0908.0505 [astro-ph.HE].

[39] A. J. Dean et al. "Polarized Gamma-Ray Emission from the Crab." In: *Science* 321.5893 (Aug. 2008), p. 1183. DOI: 10.1126/science.1149056.

[40] Jason Dexter and Eric Agol. "A FAST NEW PUBLIC CODE FOR COMPUTING PHOTON ORBITS IN A KERR SPACETIME." In: *The Astrophysical Journal* 696.2 (Apr. 2009), pp. 1616–1629. DOI: 10.1088/0004-637x/696/2/1616. URL: https://doi.org/10.1088%2F0004-637x%2F696%2F2%2F1616.

[41] J.R. Dormand and P.J. Prince. "A family of embedded Runge-Kutta formulae." In: *Journal of Computational and Applied Mathematics* 6.1 (1980), pp. 19–26. ISSN: 0377-

0427. DOI: https://doi.org/10.1016/0771-050X(80)90013-3. URL: http://www.sciencedirect.com/science/article/pii/0771050X80900133.

[42] V. Doroshenko et al. "Is there a highly magnetized neutron star in GX 301-2?" In: A&A 515, A10 (June 2010), A10. DOI: 10.1051/0004-6361/200912951. arXiv: 0907.3844 [astro-ph.HE].

[43] M. Dovciak, V. Karas, and G. Matt. "Polarization signatures of strong gravity in active galactic nuclei accretion discs." In: MNRAS 355.3 (Dec. 2004), pp. 1005–1009. DOI: 10.1111/j.1365-2966.2004.08396.x. arXiv: astro-ph/0409356 [astro-ph].

[44] A. Einstein. "Die Grundlage der allgemeinen Relativitätstheorie." In: *Annalen der Physik* 354.7 (Jan. 1916), pp. 769–822. DOI: 10.1002/andp.19163540702.

[45] I. El Mellah et al. "Formation of wind-captured disks in supergiant X-ray binaries. Consequences for Vela X-1 and Cygnus X-1." In: A&A 622, A189 (Feb. 2019), A189. DOI: 10.1051/0004-6361/201834498. arXiv: 1810.12933 [astro-ph.HE].

[46] A. C. Fabian et al. "On the determination of the spin and disc truncation of accreting black holes using X-ray reflection." In: MNRAS 439.3 (Apr. 2014), pp. 2307–2313. DOI: 10.1093/mnras/stu045. arXiv: 1401.1615 [astro-ph.HE].

[47] M. Falanga et al. "Ephemeris, orbital decay, and masses of ten eclipsing high-mass X-ray binaries." In: A&A 577, A130 (May 2015), A130. DOI: 10.1051/0004-6361/201425191. arXiv: 1502.07126 [astro-ph.HE].

[48] E. Fehlberg. *Low-order Classical Runge-Kutta Formulas with Stepsize Control and Their Application to Some Heat Transfer Problems*. NASA technical report. National Aeronautics and Space Administration, 1969. URL: https://books.google.com/books?id=IMaJw5g4hGkC.

[49] W. Forman et al. "The fourth Uhuru catalog of X-ray sources." In: ApJS 38 (Dec. 1978), pp. 357–412. DOI: 10.1086/190561.

[50] M. Forot et al. "Polarization of the Crab Pulsar and Nebula as Observed by the INTEGRAL/IBIS Telescope." In: ApJ 688.1 (Nov. 2008), p. L29. DOI: 10.1086/593974. arXiv: 0809.1292 [astro-ph].

[51] P. Chris Fragile and Peter Anninos. "Hydrodynamic Simulations of Tilted Thick-Disk Accretion onto a Kerr Black Hole." In: ApJ 623.1 (Apr. 2005), pp. 347–361. DOI: 10.1086/428433. arXiv: astro-ph/0403356 [astro-ph].

[52] P. Chris Fragile, Warner A. Miller, and Eric Vandernoot. "Iron-Line Emission as a Probe of Bardeen-Petterson Accretion Disks." In: ApJ 635.1 (Dec. 2005), pp. 157–166. DOI: 10.1086/491616. arXiv: astro-ph/0507309 [astro-ph].

[53] P. Chris Fragile et al. "Global General Relativistic Magnetohydrodynamic Simulation of a Tilted Black Hole Accretion Disk." In: ApJ 668.1 (Oct. 2007), pp. 417–429. DOI: 10.1086/521092. arXiv: 0706.4303 [astro-ph].

[54] F. Fürst et al. "Multiple cyclotron line-forming regions in GX 301-2." In: A&A 620, A153 (Dec. 2018), A153. DOI: 10.1051/0004-6361/201732132. arXiv: 1809.05691 [astro-ph.HE].

[55] J. García et al. "X-Ray Reflected Spectra from Accretion Disk Models. III. A Complete Grid of Ionized Reflection Calculations." In: ApJ 768.2, 146 (May 2013), p. 146. DOI: 10.1088/0004-637X/768/2/146. arXiv: 1303.2112 [astro-ph.HE].

[56] J. García et al. "Improved Reflection Models of Black Hole Accretion Disks: Treating the Angular Distribution of X-Rays." In: ApJ 782.2, 76 (Feb. 2014), p. 76. DOI: 10.1088/0004-637X/782/2/76. arXiv: 1312.3231 [astro-ph.HE].

[57] Jessica A. Gaskin et al. "Lynx X-Ray Observatory: an overview." In: *Journal of Astronomical Telescopes, Instruments, and Systems* 5, 021001 (Apr. 2019), p. 021001. DOI: 10.1117/1.JATIS.5.2.021001.

[58] N. Gehrels et al. "The Swift Gamma-Ray Burst Mission." In: ApJ 611.2 (Aug. 2004), pp. 1005–1020. DOI: 10.1086/422091. arXiv: astro-ph/0405233 [astro-ph].

[59] Keith C. Gendreau, Zaven Arzoumanian, and Takashi Okajima. "The Neutron star Interior Composition ExploreR (NICER): an Explorer mission of opportunity for soft x-ray timing spectroscopy." In: Proc. SPIE. Vol. 8443. Society of Photo-Optical Instrumentation Engineers (SPIE) Conference Series. Sept. 2012, p. 844313. DOI: 10.1117/12.926396.

[60] I. M. George and A. C. Fabian. "X-ray reflection from cold matter in Active Galactic Nuclei and X-ray binaries." In: MNRAS 249 (Mar. 1991), p. 352. DOI: 10.1093/mnras/249.2.352.

[61] Riccardo Giacconi. "Nobel Lecture: The dawn of x-ray astronomy." In: *Reviews of Modern Physics* 75.3 (2003), p. 995.

[62] A. Giménez-García et al. "Measuring the stellar wind parameters in IGR J17544-2619 and Vela X-1 constrains the accretion physics in supergiant fast X-ray transient and classical supergiant X-ray binaries." In: A&A 591, A26 (June 2016), A26. DOI: 10.1051/0004-6361/201527551. arXiv: 1603.00925 [astro-ph.HE].

[63] Diego Götz et al. "Variable Polarization Measured in the Prompt Emission of GRB 041219A Using IBIS on Board INTEGRAL." In: ApJ 695.2 (Apr. 2009), pp. L208–L212. DOI: 10.1088/0004-637X/695/2/L208. arXiv: 0903.1712 [astro-ph.HE].

[64] Jenny Greene, Charles D. Bailyn, and Jerome A. Orosz. "Optical and Infrared Photometry of the Microquasar GRO J1655-40 in Quiescence." In: ApJ 554.2 (June 2001), pp. 1290–1297. DOI: 10.1086/321411. arXiv: astro-ph/0101337 [astro-ph].

[65] Francesco Haardt and Laura Maraschi. "X-Ray Spectra from Two-Phase Accretion Disks." In: ApJ 413 (Aug. 1993), p. 507. DOI: 10.1086/173020.

[66] Fiona A. Harrison et al. "The Nuclear Spectroscopic Telescope Array (NuSTAR) High-energy X-Ray Mission." In: ApJ 770.2, 103 (June 2013), p. 103. DOI: 10.1088/0004-637X/770/2/103. arXiv: 1301.7307 [astro-ph.IM].

[67] John F. Hawley and Julian H. Krolik. "Magnetically Driven Jets in the Kerr Metric." In: ApJ 641.1 (Apr. 2006), pp. 103–116. DOI: 10.1086/500385. arXiv: astro-ph/0512227 [astro-ph].

[68] Jeremy Heyl and Ilaria Caiazzo. "Strongly Magnetized Sources: QED and X-ray Polarization." In: *Galaxies* 6.3 (July 2018), p. 76. DOI: 10.3390/galaxies6030076. arXiv: 1802.00358 [astro-ph.HE].

[69] J. E. Hill et al. "The x-ray polarimeter instrument on board the Polarimeter for Relativistic Astrophysical X-ray Sources (PRAXyS) mission." In: Proc. SPIE. Vol. 9905. Society of Photo-Optical Instrumentation Engineers (SPIE) Conference Series. July 2016, 99051B. DOI: 10.1117/12.2233322.

[70] R. M. Hjellming and M. P. Rupen. "Episodic ejection of relativistic jets by the X-ray transient GRO J1655 - 40." In: Nature 375.6531 (June 1995), pp. 464–468. DOI: 10.1038/375464a0.

[71] Janie K. Hoormann, Banafsheh Beheshtipour, and Henric Krawczynski. "Testing general relativity's no-hair theorem with x-ray observations of black holes." In: Phys. Rev. D 93.4, 044020 (Feb. 2016), p. 044020. DOI: 10.1103/PhysRevD.93.044020. arXiv: 1601.02055 [astro-ph.HE].

[72] J. H. Hough. "Polarimetry Techniques at Optical and Infrared Wavelengths." In: *Astronomical Polarimetry: Current Status and Future Directions*. Ed. by A. Adamson et al. Vol. 343. Astronomical Society of the Pacific Conference Series. Dec. 2005, p. 3.

[73] Adam Ingram and Chris Done. "The effect of frame dragging on the iron Kα line in X-ray binaries." In: MNRAS 427.2 (Dec. 2012), pp. 934–947. DOI: 10.1111/j.1365-2966.2012.21907.x. arXiv: 1208.0728 [astro-ph.HE].

[74] Adam Ingram et al. "Polarization Modulation from Lense-Thirring Precession in X-Ray Binaries." In: ApJ 807.1, 53 (July 2015), p. 53. DOI: 10.1088/0004-637X/807/1/53. arXiv: 1505.00015 [astro-ph.HE].

[75] Adam Ingram et al. "Tomographic reflection modelling of quasi-periodic oscillations in the black hole binary H 1743-322." In: MNRAS 464.3 (Jan. 2017), pp. 2979–2991. DOI: 10.1093/mnras/stw2581. arXiv: 1610.00948 [astro-ph.HE].

[76] Keith Jahoda et al. "In-orbit performance and calibration of the Rossi X-ray Timing Explorer (RXTE) Proportional Counter Array (PCA)." In: Proc. SPIE. Ed. by Oswald H. Siegmund and Mark A. Gummin. Vol. 2808. Society of Photo-Optical Instrumentation Engineers (SPIE) Conference Series. Oct. 1996, pp. 59–70. DOI: 10.1117/12.256034.

[77] Keith Jahoda et al. "The X-ray Polarization Probe mission concept." In: BAAS. Vol. 51. Sept. 2019, p. 181.

[78] F. Jansen et al. "XMM-Newton observatory. I. The spacecraft and operations." In: A&A 365 (Jan. 2001), pp. L1–L6. DOI: 10.1051/0004-6361:20000036.

[79] E. Jourdain and J. -P. Roques. "2003-2018 Monitoring of the Crab Nebula Polarization in Hard X-Rays with INTEGRAL SPI." In: ApJ 882.2, 129 (Sept. 2019), p. 129. DOI: 10.3847/1538-4357/ab3422. arXiv: 1907.09341 [astro-ph.HE].

[80] Philip E. Kaaret et al. "Status of the stellar x-ray polarimeter for the Spectrum-X-Gamma mission." In: Proc. SPIE. Ed. by Silvano Fineschi. Vol. 2010. Society of Photo-Optical Instrumentation Engineers (SPIE) Conference Series. 1994, pp. 22–27. DOI: 10.1117/12.168582.

[81] L. Kaper, A. van der Meer, and F. Najarro. "VLT/UVES spectroscopy of Wray 977, the hypergiant companion to the X-ray pulsar <ASTROBJ>GX301-2</ASTROBJ>." In: A&A 457.2 (Oct. 2006), pp. 595–610. DOI: 10.1051/0004-6361:20065393. arXiv: astro-ph/0607613 [astro-ph].

[82] E. Kara et al. "The corona contracts in a black-hole transient." In: Nature 565.7738 (Jan. 2019), pp. 198–201. DOI: 10.1038/s41586-018-0803-x. arXiv: 1901.03877 [astro-ph.HE].

[83] Roy P. Kerr. "Gravitational Field of a Spinning Mass as an Example of Algebraically Special Metrics." In: Phys. Rev. Lett. 11.5 (Sept. 1963), pp. 237–238. DOI: 10.1103/PhysRevLett.11.237.

[84] A. R. King et al. "Aligning spinning black holes and accretion discs." In: MNRAS 363.1 (Oct. 2005), pp. 49–56. DOI: 10.1111/j.1365-2966.2005.09378.x. arXiv: astro-ph/0507098 [astro-ph].

[85] Andrew King and Chris Nixon. "Misaligned Accretion and Jet Production." In: ApJ 857.1, L7 (Apr. 2018), p. L7. DOI: 10.3847/2041-8213/aab8f9. arXiv: 1803.08927 [astro-ph.HE].

[86] Fabian Kislat et al. "Optimization of the design of X-Calibur for a long-duration balloon flight and results from a one-day test flight." In: *Journal of Astronomical Telescopes, Instruments, and Systems* 4, 011004 (Jan. 2018), p. 011004. DOI: 10.1117/1.JATIS.4.1.011004.

[87] O. Klein and T. Nishina. "Über die Streuung von Strahlung durch freie Elektronen nach der neuen relativistischen Quantendynamik von Dirac." In: *Zeitschrift fur Physik* 52.11-12 (Nov. 1929), pp. 853–868. DOI: 10.1007/BF01366453.

[88] Danny T. Koh et al. "Rapid Spin-Up Episodes in the Wind-fed Accreting Pulsar GX 301-2." In: ApJ 479.2 (Apr. 1997), pp. 933–947. DOI: 10.1086/303929.

[89] H. Krawczynski, G. Chartas, and F. Kislat. "The Effect of Microlensing on the Observed X-Ray Energy Spectra of Gravitationally Lensed Quasars." In: ApJ 870.2, 125 (Jan. 2019), p. 125. DOI: 10.3847/1538-4357/aaf39c. arXiv: 1809.01057 [astro-ph.HE].

[90] H. Krawczynski et al. "Scientific prospects for hard X-ray polarimetry." In: *Astroparticle Physics* 34.7 (Feb. 2011), pp. 550–567. DOI: 10.1016/j.astropartphys.2010.12.001. arXiv: 1012.0321 [astro-ph.HE].

[91] Henric Krawczynski. "Tests of General Relativity in the Strong-gravity Regime Based on X-Ray Spectropolarimetric Observations of Black Holes in X-Ray Binaries." In: ApJ 754.2, 133 (Aug. 2012), p. 133. DOI: 10.1088/0004-637X/754/2/133. arXiv: 1205.7063 [gr-qc].

[92] Henric S. Krawczynski et al. "X-ray polarimetry with the Polarization Spectroscopic Telescope Array (PolSTAR)." In: *Astroparticle Physics* 75 (Feb. 2016), pp. 8–28. DOI: 10.1016/j.astropartphys.2015.10.009. arXiv: 1510.08358 [astro-ph.IM].

[93] S. Kumar and J. E. Pringle. "Twisted accretion discs - The Bardeen-Petterson effect." In: MNRAS 213 (Mar. 1985), pp. 435–442. DOI: 10.1093/mnras/213.3.435.

[94] Josef Lense and Hans Thirring. "Über den Einfluß der Eigenrotation der Zentralkörper auf die Bewegung der Planeten und Monde nach der Einsteinschen Gravitationstheorie." In: *Physikalische Zeitschrift* 19 (Jan. 1918), p. 156.

[95] M. Liska et al. "Bardeen-Petterson alignment, jets, and magnetic truncation in GRMHD simulations of tilted thin accretion discs." In: MNRAS 487.1 (July 2019), pp. 550–561. DOI: 10.1093/mnras/stz834. arXiv: 1810.00883 [astro-ph.HE].

[96] Matthew Liska et al. "H-AMR: A New GPU-accelerated GRMHD Code for Exascale Computing With 3D Adaptive Mesh Refinement and Local Adaptive Time-stepping." In: *arXiv e-prints*, arXiv:1912.10192 (Dec. 2019), arXiv:1912.10192. arXiv: 1912.10192 [astro-ph.HE].

[97] M. L. Lister et al. "4C +12.50: A Superluminal Precessing Jet in the Recent Merger System IRAS 13451+1232." In: ApJ 584.1 (Feb. 2003), pp. 135–146. DOI: 10.1086/345666. arXiv: astro-ph/0210372 [astro-ph].

[98] G. Lodato and J. E. Pringle. "The evolution of misaligned accretion discs and spinning black holes." In: MNRAS 368.3 (May 2006), pp. 1196–1208. DOI: 10.1111/j.1365-2966.2006.10194.x. arXiv: astro-ph/0602306 [astro-ph].

[99] Giuseppe Lodato and Daniel J. Price. "On the diffusive propagation of warps in thin accretion discs." In: MNRAS 405.2 (June 2010), pp. 1212–1226. DOI: 10.1111/j.1365-2966.2010.16526.x. arXiv: 1002.2973 [astro-ph.HE].

[100] Giuseppe Lodato and J. E. Pringle. "Warp diffusion in accretion discs: a numerical investigation." In: MNRAS 381.3 (Nov. 2007), pp. 1287–1300. DOI: 10.1111/j.1365-2966.2007.12332.x. arXiv: 0708.1124 [astro-ph].

[101] S. H. Lubow, G. I. Ogilvie, and J. E. Pringle. "The evolution of a warped disc around a Kerr black hole." In: MNRAS 337.2 (Dec. 2002), pp. 706–712. DOI: 10.1046/j.1365-8711.2002.05949.x. arXiv: astro-ph/0208206 [astro-ph].

[102] Herman L. Marshall et al. "The rocket experiment demonstration of a soft x-ray polarimeter (REDSoX Polarimeter)." In: Proc. SPIE. Vol. 10397. Society of Photo-Optical Instrumentation Engineers (SPIE) Conference Series. Aug. 2017, 103970K. DOI: 10.1117/12.2274107.

[103] Herman L. Marshall et al. "Design of a broadband soft x-ray polarimeter." In: *Journal of Astronomical Telescopes, Instruments, and Systems* 4, 011005 (Jan. 2018), p. 011005. DOI: 10.1117/1.JATIS.4.1.011005.

[104] Andrea Martocchia and Giorgio Matt. "Iron Kalpha line intensity from accretion discs around rotating black holes." In: MNRAS 282.4 (Oct. 1996), pp. L53–L57. DOI: 10.1093/mnras/282.4.L53.

[105] Hironori Matsumoto et al. "Inorbit performance of the Hard X-ray Telescope (HXT) on board the Hitomi (ASTRO-H) satellite." In: *Journal of Astronomical Telescopes, Instruments, and Systems* 4, 011212 (Jan. 2018), p. 011212. DOI: 10.1117/1.JATIS.4.1.011212. arXiv: 1803.00242 [astro-ph.IM].

[106] G. Matt, G. C. Perola, and L. Piro. "The iron line and high energy bump as X-ray signatures of cold matter in Seyfert 1 galaxies." In: A&A 247 (July 1991), p. 25.

[107] Jeffrey E. McClintock, Ramesh Narayan, and James F. Steiner. "Black Hole Spin via Continuum Fitting and the Role of Spin in Powering Transient Jets." In: Space Sci. Rev. 183.1-4 (Sept. 2014), pp. 295–322. DOI: 10.1007/s11214-013-0003-9. arXiv: 1303.1583 [astro-ph.HE].

[108] Jeffrey E. McClintock et al. "Measuring the spins of accreting black holes." In: *Classical and Quantum Gravity* 28.11, 114009 (June 2011), p. 114009. DOI: 10.1088/0264-9381/28/11/114009. arXiv: 1101.0811 [astro-ph.HE].

[109] Jonathan C. McKinney, Alexander Tchekhovskoy, and Roger D. Bland ford. "Alignment of Magnetized Accretion Disks and Relativistic Jets with Spinning Black Holes." In: *Science* 339.6115 (Jan. 2013), p. 49. DOI: 10.1126/science.1230811. arXiv: 1211.3651 [astro-ph.CO].

[110] P. Meszaros and W. Nagel. "X-ray pulsar models. II. Comptonized spectra and pulse shapes." In: ApJ 299 (Dec. 1985), pp. 138–153. DOI: 10.1086/163687.

[111] P. Meszaros et al. "Astrophysical Implications and Observational Prospects of X-Ray Polarimetry." In: ApJ 324 (Jan. 1988), p. 1056. DOI: 10.1086/165962.

[112] J. J. Monaghan. "Smoothed particle hydrodynamics." In: ARA&A 30 (Jan. 1992), pp. 543–574. DOI: 10.1146/annurev.aa.30.090192.002551.

[113] Fabio Muleri et al. "Performance of the Gas Pixel Detector: an x-ray imaging polarimeter for upcoming missions of astrophysics." In: Proc. SPIE. Vol. 9905. Society of Photo-Optical Instrumentation Engineers (SPIE) Conference Series. July 2016, 99054G. DOI: 10.1117/12.2233206.

[114] Armin Nabizadeh et al. "NuSTAR observations of wind-fed X-ray pulsar GX 301-2 during unusual spin-up event." In: A&A 629, A101 (Sept. 2019), A101. DOI: 10.1051/0004-6361/201936045. arXiv: 1907.12923 [astro-ph.HE].

[115] Kirpal Nandra et al. "The Hot and Energetic Universe: A White Paper presenting the science theme motivating the Athena+ mission." In: *arXiv e-prints*, arXiv:1306.2307 (June 2013), arXiv:1306.2307. arXiv: 1306.2307 [astro-ph.HE].

[116] Richard P. Nelson and John C. B. Papaloizou. "Hydrodynamic simulations of propagating WARPS and bending waves in accretion discs." In: MNRAS 309.4 (Nov. 1999), pp. 929–940. DOI: 10.1046/j.1365-8711.1999.02894.x. arXiv: astro-ph/9907076 [astro-ph].

[117] Richard P. Nelson and John C. B. Papaloizou. "Hydrodynamic simulations of the Bardeen-Petterson effect." In: MNRAS 315.3 (July 2000), pp. 570–586. DOI: 10.1046/j.1365-8711.2000.03478.x. arXiv: astro-ph/0001439 [astro-ph].

[118] Chris Nixon and Greg Salvesen. "A physical model for state transitions in black hole X-ray binaries." In: MNRAS 437.4 (Feb. 2014), pp. 3994–3999. DOI: 10.1093/mnras/stt2215. arXiv: 1311.2930 [astro-ph.HE].

[119] Chris Nixon et al. "Tearing up the Disk: How Black Holes Accrete." In: ApJ 757.2, L24 (Oct. 2012), p. L24. DOI: 10.1088/2041-8205/757/2/L24. arXiv: 1209.1393 [astro-ph.HE].

[120] Christopher J. Nixon and Andrew R. King. "Broken discs: warp propagation in accretion discs." In: MNRAS 421.2 (Apr. 2012), pp. 1201–1208. DOI: 10.1111/j.1365-2966.2011.20377.x. arXiv: 1201.1297 [astro-ph.HE].

[121] Scott C. Noble, Julian H. Krolik, and John F. Hawley. "Dependence of Inner Accretion Disk Stress on Parameters: The Schwarzschild Case." In: ApJ 711.2 (Mar. 2010), pp. 959–973. DOI: 10.1088/0004-637X/711/2/959. arXiv: 1001.4809 [astro-ph.HE].

[122] I. D. Novikov and K. S. Thorne. "Astrophysics of black holes." In: *Black Holes (Les Astres Occlus)*. Jan. 1973, pp. 343–450.

[123] Michael A. Nowak et al. "Suzaku Observations of 4U 1957+11: Potentially the Most Rapidly Spinning Black Hole in (the Halo of) the Galaxy." In: ApJ 744.2, 107 (Jan. 2012), p. 107. DOI: 10.1088/0004-637X/744/2/107. arXiv: 1109.6008 [astro-ph.HE].

[124] NSSTC Web Page. 2020. URL: https://gammaray.nsstc.nasa.gov/gbm/science/pulsars.html (visited on 05/20/2020).

[125] G. I. Ogilvie. "The non-linear fluid dynamics of a warped accretion disc." In: MNRAS 304.3 (Apr. 1999), pp. 557–578. DOI: 10.1046/j.1365-8711.1999.02340.x. arXiv: astro-ph/9812073 [astro-ph].

[126] G. I. Ogilvie. "An alpha theory of time-dependent warped accretion discs." In: MNRAS 317.3 (Sept. 2000), pp. 607–622. DOI: 10.1046/j.1365-8711.2000.03654.x. arXiv: astro-ph/0005278 [astro-ph].

[127] Takashi Okajima et al. "Characterization of the supermirror hard-x-ray telescope for the InFOCμS balloon experiment." In: Appl. Opt. 41.25 (Sept. 2002), pp. 5417–5426. DOI: 10.1364/AO.41.005417.

[128] Jerome A. Orosz et al. "An Improved Dynamical Model for the Microquasar XTE J1550-564." In: ApJ 730.2, 75 (Apr. 2011), p. 75. DOI: 10.1088/0004-637X/730/2/75. arXiv: 1101.2499 [astro-ph.SR].

[129] Jerome A. Orosz et al. "The Mass of the Black Hole in Cygnus X-1." In: ApJ 742.2, 84 (Dec. 2011), p. 84. DOI: 10.1088/0004-637X/742/2/84. arXiv: 1106.3689 [astro-ph.HE].

[130] Don N. Page and Kip S. Thorne. "Disk-Accretion onto a Black Hole. Time-Averaged Structure of Accretion Disk." In: ApJ 191 (July 1974), pp. 499–506. DOI: 10.1086/152990.

[131] J. C. B. Papaloizou and J. E. Pringle. "The time-dependence of non-planar accretion discs." In: MNRAS 202 (Mar. 1983), pp. 1181–1194. DOI: 10.1093/mnras/202.4.1181.

[132] William H. Press et al. *Numerical recipes in C++ : the art of scientific computing*. 2002.

[133] J. E. Pringle. "A simple approach to the evolution of twisted accretion discs." In: MNRAS 258.4 (Oct. 1992), pp. 811–818. DOI: 10.1093/mnras/258.4.811.

[134] H. Quaintrell et al. "The mass of the neutron star in Vela X-1 and tidally induced non-radial oscillations in GP Vel." In: A&A 401 (Apr. 2003), pp. 313–323. DOI: 10.1051/0004-6361:20030120. arXiv: astro-ph/0301243 [astro-ph].

[135] Ronald A. Remillard and Jeffrey E. McClintock. "X-Ray Properties of Black-Hole Binaries." In: ARA&A 44.1 (Sept. 2006), pp. 49–92. DOI: 10.1146/annurev.astro.44.051905.092532. arXiv: astro-ph/0606352 [astro-ph].

[136] Christopher S. Reynolds and Michael A. Nowak. "Fluorescent iron lines as a probe of astrophysical black hole systems." In: Phys. Rep. 377.6 (Apr. 2003), pp. 389–466. DOI: 10.1016/S0370-1573(02)00584-7. arXiv: astro-ph/0212065 [astro-ph].

[137] P. A. G. Scheuer and R. Feiler. "The realignment of a black hole misaligned with its accretion disc." In: MNRAS 282 (Sept. 1996), p. 291. DOI: 10.1093/mnras/282.1.291.

[138] Jeremy D. Schnittman and Julian H. Krolik. "X-ray Polarization from Accreting Black Holes: The Thermal State." In: ApJ 701.2 (Aug. 2009), pp. 1175–1187. DOI: 10.1088/0004-637X/701/2/1175. arXiv: 0902.3982 [astro-ph.HE].

[139] K. Schwarzschild. "On the gravitational field of a mass point according to Einstein's theory." In: *arXiv e-prints*, physics/9905030 (May 1999), physics/9905030. arXiv: physics/9905030 [physics.hist-ph].

[140] Julian Schwinger. "On Gauge Invariance and Vacuum Polarization." In: *Physical Review* 82.5 (June 1951), pp. 664–679. DOI: 10.1103/PhysRev.82.664.

[141] N. I. Shakura. "The long-period X-ray pulsar 3U 0900-40 as a neutron star with an abnormally strong magnetic field." In: *Soviet Astronomy Letters* 1 (Dec. 1975), pp. 223–225.

[142] N. I. Shakura and R. A. Sunyaev. "Reprint of 1973A&A....24..337S. Black holes in binary systems. Observational appearance." In: A&A 500 (June 1973), pp. 33–51.

[143] Aneta Siemiginowska, Randall K. Smith, and Keith A. Arnaud. *Handbook of X-ray Astronomy.* Cambridge Observing Handbooks for Research Astronomers. Cambridge University Press, 2011. ISBN: 9780521883733.

[144] Kareem A. Sorathia, Julian H. Krolik, and John F. Hawley. "Magnetohydrodynamic Simulation of a Disk Subjected to Lense-Thirring Precession." In: ApJ 777.1, 21 (Nov. 2013), p. 21. DOI: 10.1088/0004-637X/777/1/21. arXiv: 1309.0290 [astro-ph.HE].

[145] David Stuchlik. "The NASA Wallops Arc-Second Pointer (WASP) System for Precision Pointing of Scientific Balloon Instruments and Telescopes." In: June 2017. DOI: 10.2514/6.2017-3609.

[146] David W. Stuchlik. "The Wallops Arc Second Pointer - A Balloon Borne Fine Pointing System." In: *AIAA Balloon Systems Conference*. DOI: 10.2514/6.2015-3039. eprint: https://arc.aiaa.org/doi/pdf/10.2514/6.2015-3039. URL: https://arc.aiaa.org/doi/abs/10.2514/6.2015-3039.

[147] Slawomir Suchy et al. "Broadband Spectroscopy Using Two Suzaku Observations of the HMXB GX 301-2." In: ApJ 745.2, 124 (Feb. 2012), p. 124. DOI: 10.1088/0004-637X/745/2/124. arXiv: 1111.2088 [astro-ph.HE].

[148] John Tomsick et al. "The Compton Spectrometer and Imager." In: BAAS. Vol. 51. Sept. 2019, p. 98. arXiv: 1908.04334 [astro-ph.IM].

[149] John A. Tomsick et al. "The Reflection Component from Cygnus X-1 in the Soft State Measured by NuSTAR and Suzaku." In: ApJ 780.1, 78 (Jan. 2014), p. 78. DOI: 10.1088/0004-637X/780/1/78. arXiv: 1310.3830 [astro-ph.HE].

[150] John A. Tomsick et al. "Alternative Explanations for Extreme Supersolar Iron Abundances Inferred from the Energy Spectrum of Cygnus X-1." In: ApJ 855.1, 3 (Mar. 2018), p. 3. DOI: 10.3847/1538-4357/aaaab1. arXiv: 1801.07267 [astro-ph.HE].

[151] Hiroshi Tsunemi et al. "Formation Flight Astronomical Survey Telescope (FFAST) mission in hard x-ray." In: Proc. SPIE. Vol. 9144. Society of Photo-Optical Instrumentation Engineers (SPIE) Conference Series. July 2014, 91442R. DOI: 10.1117/12.2054733.

[152] S. S. Tsygankov, A. A. Lutovinov, and A. V. Serber. "Completing the puzzle of the 2004-2005 outburst in V0332+53: the brightening phase included." In: MNRAS 401.3 (Jan. 2010), pp. 1628–1635. DOI: 10.1111/j.1365-2966.2009.15791.x. arXiv: 0909.5379 [astro-ph.HE].

[153] P. Uttley et al. "X-ray reverberation around accreting black holes." In: A&A Rev. 22, 72 (Aug. 2014), p. 72. DOI: 10.1007/s00159-014-0072-0. arXiv: 1405.6575 [astro-ph.HE].

[154] G. Vedrenne et al. "SPI: The spectrometer aboard INTEGRAL." In: A&A 411 (Nov. 2003), pp. L63–L70. DOI: 10.1051/0004-6361:20031482.

[155] D. J. Walton et al. "The Soft State of Cygnus X-1 Observed with NuSTAR: A Variable Corona and a Stable Inner Disk." In: ApJ 826.1, 87 (July 2016), p. 87. DOI: 10.3847/0004-637X/826/1/87. arXiv: 1605.03966 [astro-ph.HE].

[156] Yan Wang and Xiang-Dong Li. "Strong Field Effects on Emission Line Profiles: Kerr Black Holes and Warped Accretion Disks." In: ApJ 744.2, 186 (Jan. 2012), p. 186. DOI: 10.1088/0004-637X/744/2/186. arXiv: 1110.4997 [astro-ph.HE].

[157] B. Louise Webster and Paul Murdin. "Cygnus X-1-a Spectroscopic Binary with a Heavy Companion ?" In: Nature 235.5332 (Jan. 1972), pp. 37–38. DOI: 10.1038/235037a0.

[158] M. C. Weisskopf et al. "Measurement of the X-ray polarization of the Crab nebula." In: ApJ 208 (Sept. 1976), pp. L125–L128. DOI: 10.1086/182247.

[159] M. C. Weisskopf et al. "A precision measurement of the X-ray polarization of the Crab Nebula without pulsar contamination." In: ApJ 220 (Mar. 1978), pp. L117–L121. DOI: 10.1086/182648.

[160] M. C. Weisskopf et al. "An Overview of the Performance and Scientific Results from the Chandra X-Ray Observatory." In: PASP 114.791 (Jan. 2002), pp. 1–24. DOI: 10.1086/338108. arXiv: astro-ph/0110308 [astro-ph].

[161] Martin C. Weisskopf et al. "The Imaging X-ray Polarimetry Explorer (IXPE)." In: Proc. SPIE. Vol. 9905. Society of Photo-Optical Instrumentation Engineers (SPIE) Conference Series. 2016, p. 990517. DOI: 10.1117/12.2235240.

[162] D. R. Wilkins et al. "Returning radiation in strong gravity around black holes: Reverberation from the accretion disc." In: *arXiv e-prints*, arXiv:2008.08083 (Aug. 2020), arXiv:2008.08083. arXiv: 2008.08083 [astro-ph.HE].

[163] Daniel C. Wilkins. "Bound Geodesics in the Kerr Metric." In: Phys. Rev. D 5.4 (Feb. 1972), pp. 814–822. DOI: 10.1103/PhysRevD.5.814.

[164] XRISM Science Team. "Science with the X-ray Imaging and Spectroscopy Mission (XRISM)." In: *arXiv e-prints*, arXiv:2003.04962 (Mar. 2020), arXiv:2003.04962. arXiv: 2003.04962 [astro-ph.HE].

[165] ShuangNan Zhang et al. "The enhanced X-ray Timing and Polarimetry mission—eXTP." In: *Science China Physics, Mechanics, and Astronomy* 62.2, 29502 (Feb. 2019), p. 29502. DOI: 10.1007/s11433-018-9309-2. arXiv: 1812.04020 [astro-ph.IM].